PIV Investigation of Turbulent Flow around Partially Submerged Circular Cylinders with and without Simulated Upstream Ice Blocks

by

Mark Kofi Israel

A Thesis submitted to the Faculty of Graduate Studies of the University of Manitoba in partial fulfilment of the requirements of the degree of

MASTER OF SCIENCE

Department of Mechanical Engineering

University of Manitoba

Winnipeg

ABSTRACT

Two sets of particle image velocimetry (PIV) experiments were conducted around stationary, partially submerged horizontal circular cylinders. The first set investigated the effects of blockage ratio (BR), submergence level, and a simulated upstream ice cover on the spatiotemporal dynamics of the wake flow at a Reynolds number of 10 000. The results were compared to a reference case of a cylinder fully immersed in the uniform flow. Due to the absence of an upper shear layer, the recirculation lengths of the submerged cylinder are longer, but the turbulence levels are lower compared to the uniform case. Increasing BR has no significant effect on the recirculation length but increases turbulence levels. Conversely, a decrease in submergence level shortens the recirculation length but has negligible impact on turbulence levels. An upstream ice cover further reduces the recirculation length and decreases the turbulence levels around the cylinder due to the boundary layer beneath the ice cover. The sources of turbulence production were investigated, and the unsteady dynamics were examined using frequency spectra of fluctuating velocities, proper orthogonal decomposition, and the reverse flow area.

The second set of experiments examined the effects of different lengths, thicknesses, and undersurfaces of simulated upstream ice blocks on the mean flow and turbulence transport phenomena around a submerged cylinder. The cylinder was submerged 50% below the free surface, and the Reynolds number was 25 500. The cylinder encounters an approach flow with lower momentum but higher turbulence intensity when placed behind a longer ice block, and undersurface roughness reduces the momentum but enhances the turbulence intensity of the approach flow. The recirculation length, mean velocities, and turbulence levels around the cylinder reduce with increasing ice block length and subsequent roughening of its undersurface.

ACKNOWLEDGEMENTS

I want to thank the Almighty God for His help and protection. My sincere gratitude also goes to my advisors, Dr. Mark Tachie and Dr. Karen Dow, for providing me the opportunity to pursue this master's degree program and for the confidence they showed in me which has helped me through this journey. I am very grateful for the opportunity they granted me to attend and present my research at a conference in Italy. I am grateful to Dr. Shawn Clark for his immense contributions to my research. Dr. Xingjun Fang, Mr. Brendan Pachal and Mr. Dave Tataryn all provided invaluable support during my experiments, and I say thank you to them.

My gratitude also goes to Dr. Godwin Tay through whom I was able to connect with Dr. Mark Tachie and be offered this opportunity to pursue my master's in Canada. A big thank you to Rev. Emmanuel Samba for his encouragement and the kindness he showed me by paying for my flight ticket and visa fees to travel to pursue this program. I also want to thank my parents, Mr. Martin Israel and Mrs. Evelyn Lartey, and my siblings, Alison Israel and Edwin Israel, for their love, support and sacrifices. My sincerest gratitude to my friend and brother, Sedem Kumahor, for his encouragement, support and guidance. To Kwasi Agyei-Agyemang, Fati Abdul-Salam and my other colleagues in the research group, thank you for every help. I would also like to thank my friend Naana Nyamekye for her prayers. Finally, thank you to Dr. Shawn Clark and Dr. Ebenezer Essel for accepting to be part of my examining committee.

TABLE OF CONTENTS

LIST OF FIGURES

LIST OF TABLES

NOMENCLATURE

Abbreviations

BR	Blockage ratio
FOV	Field of view
KH	Kelvin-Helmholtz
PDF	Probability density function
PIV	Particle image velocimetry
POD	Proper orthogonal decomposition
SV	Secondary vortex
TKE	Turbulence kinetic energy
VK	von Kármán

Symbols

A	Reverse flow area
d	Cylinder diameter
f	Vortex shedding frequency
Fr_d	Froude number based on freestream velocity and cylinder diameter
Fr_h	Froude number based on freestream velocity and upstream water level
Fr_S	Froude number based on freestream velocity and submergence level
g	Acceleration due to gravity
h	Upstream water level
H	Boundary layer shape factor
l	Length of ice block
L_r	Mean recirculation length

P_k	Turbulence production
Re	Reynolds number based on freestream velocity and cylinder diameter
R_{ij}	Correlation coefficient
S	Submergence level
S_k	Stokes number
$S_{A'}$	Skewness factor of fluctuating reverse flow area
St	Strouhal number
t_s	Submerged thickness of ice block
T_{int}	Integral time scale
T_r	Mean thickness of recirculation bubble
Tu	Turbulence intensity
$\overline{u'u'}$, $\overline{v'v'}$	Reynolds normal stresses
$\overline{u'v'}$	Reynolds shear stress
$\overline{u'u'u'}$, $\overline{v'v'v'}$	Third order moments of velocity fluctuations
u	Streamwise instantaneous velocity
U	Streamwise mean velocity
U_c	Convective velocity
U_e	Freestream velocity
U_{max}	Maximum streamwise mean velocity
U_b	Maximum backflow velocity
U_s	Slip velocity of seeding particles
V	Vertical mean velocity
x	Streamwise direction

y	Vertical direction
δ	Boundary layer thickness
δ^*	Boundary layer displacement thickness
δ_ω	Vorticity thickness
θ	Boundary layer momentum thickness
λ	Wavelength
Λ	Swirling strength
$\Lambda_{ci,z}$	Signed swirling strength
ν	Kinematic viscosity of working fluid
ρ_f	Density of working fluid
ρ_p	Density of seeding particles
τ_f	Viscous timescale
τ_p	Relaxation time of seeding particles
τ_o	Largest characteristic timescale
ξ_u	Uncertainty in streamwise mean velocity
$\xi_{\overline{u'u'},\overline{v'v'}}$	Uncertainty in Reynolds normal stresses
$\xi_{\overline{u'v'}}$	Uncertainty in Reynolds shear stress

Subscripts and Superscripts

$(.)'$	Fluctuating component
$\overline{(.)}$	Time-averaged component
$(.)_{rms}$	Root-mean-square value

1 INTRODUCTION

This chapter presents the motivation and background of this present study, as well as the outline of the other sections of this thesis.

1.1 Background and Motivation

A partially submerged horizontal circular cylinder interacting with a crossflow has a wide range of geophysical and engineering applications. A typical example is the flow around booms (see Figure 1.1), which consist of partially submerged horizontal cylindrical pontoons chained together, spanning the entire width of a river channel upstream or downstream of hydraulic structures. These booms are often used for containing floating debris (debris booms), preventing oil spills from spreading (oil containment booms), providing safer waterways (safety booms), and retaining upstream ice (ice booms). The ice boom is the main motivation for this present study.

As ambient temperature decreases during winter in cold-climate countries like Canada, rivers cool below the freezing point, and turbulent water forms small, needle- or disc-shaped ice crystals called frazil ice when it reaches a supercooled state (Hicks 2009; Senarathbandara et al. 2023). The presence of ice in rivers poses unique challenges to both natural processes and hydraulic infrastructure. For instance, frazil ice on intakes of hydroelectric power stations reduces the discharge and operational efficiency of hydroelectric power systems at a time that often coincides with the peak annual energy demand, resulting in loss of power generation revenue (Abdelnour et al. 1998; Gebre et al. 2013). Ice jams, which can also form when river ice accumulates at narrow channel constrictions, obstruct the passage of water, leading to a rise in the upstream water level and potential flooding (Boucher 2014; Fang et al. 2023). To mitigate these adverse effects of river

(a)

(b)

Figure 1.1. Pictures of (a) floating pontoons of booms in open water (Source: ODINBoom®) and (b) ice booms with upstream ice cover (Source: Ontario Power Generation).

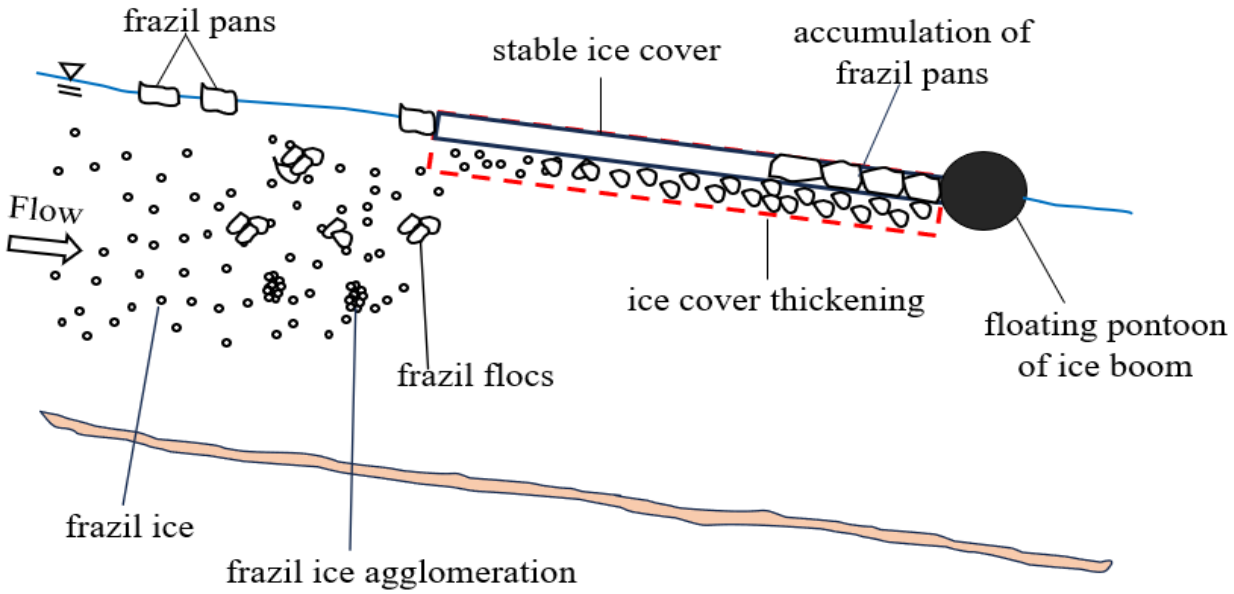

Figure 1.2. Schematic of the formation process of a stable ice cover initiated by a floating ice boom pontoon (adapted from Gebre et al. 2013; Senarathbandara et al. 2023).

ice on hydraulic structures and ensure public safety, ice booms are used to retain ice and initiate formation of a stable ice cover which insulates the water and reduces subsequent frazil ice production throughout the winter (see Figure 1.1(b)).

Figure 1.2 illustrates a typical formation process of a stable ice cover by an ice boom deployed in a cold-region river. Frazil ice produced in the fast flowing, open water sections agglomerate together to form buoyant ice flocs which subsequently form larger structures known as ice pans at the open water surface (Beltaos 1983; Poole 1994; Hicks 2009; Boucher 2014). These floating ice pans collect against the ice boom pontoons before freezing in-situ to form a stable ice cover (Pariset and Hauser 1961; Foltyn and Tuthill 1996; Abdelnour et al. 1998). As more ice is transported downstream, the ice cover created by the boom lengthens in the upstream direction, and the deposition of frazil materials beneath the ice cover contributes to its thickening (Beltaos 1983; Boucher 2014; Senarathbandara et al. 2023). This process of elongation repeats until the ice cover

is stable. Meanwhile, the undersurface of an ice cover, which is usually smooth may become rough over time with the accumulation of debris underneath it (Edie 2022; Fang et al. 2023).

Unfortunately, several ice boom failures have been reported over the past decades which resulted in catastrophic impacts on the hydraulic structures they were designed to protect and increased public safety risks at these structures (Poole 1994; Abdelnour et al. 1998). These failures, which are partly attributed to the turbulent flow induced by the floating pontoons (Poole 1994), persist to date because the flow dynamics around ice booms are still not well understood due to the safety and logistical challenges associated with conducting field studies (Nyantekyi-Kwakye et al. 2019). Another factor contributing to the limited understanding of the turbulent flow dynamics around ice booms with upstream ice is that the few experimental and numerical studies conducted were restricted to the impact forces of ice on boom structures (Løset and Timco 1993; Timco and Cornett 1996; Hopkins and Tuthill 2002; Morse et al. 2006) with no assessment of the turbulent flow dynamics around floating pontoons. Like ice booms, booms in open water conditions, such as oil containment booms, are prone to structural vibration and acoustic noise due to the variety of unsteady flow phenomena around them. However, there is limited understanding of the unsteady flow dynamics around these booms because the few studies conducted on the turbulent flow around floating pontoons (modelled as partially submerged circular cylinders) in open water, did not examine the spatiotemporal characteristics (Triantafyllou and Dimas 1989; Ozdil and Akilli 2015; Bouscasse et al. 2017; Edie et al. 2021; Edie 2022; Addai et al. 2024). Understanding the spatiotemporal dynamics of the wake flow around partially submerged circular cylinders with and without upstream ice would enable engineers to develop effective flow control strategies to prevent the failure of booms. To this end, two sets of experiments were performed to understand the dynamics of the separated flow induced by a single partially submerged circular cylinder with and

without upstream ice. The first set of experiments investigated the effects of blockage ratio, submergence level and a simulated upstream ice cover on the spatiotemporal characteristics of the wake flow, while the second set of experiments focused on the effects of different conditions of simulated upstream ice blocks on the mean and turbulent transport phenomena around the cylinder. In most practical applications, boom pontoons are usually flexible and free to oscillate at the surface of the water; however, this study focuses on the fundamental case of the cylinder held stationary at fixed submergence levels.

1.2 Thesis Outline

The rest of this thesis is organized as follows: a review of the relevant literature is presented in Chapter 2, the experimental setup and measurement procedure are described in Chapter 3, and the results are discussed in Chapter 4. A summary of the key findings as well as recommendations for future research work are then presented in Chapter 5.

2 LITERATURE REVIEW

This chapter presents a review of the pertinent literature on the separated flow dynamics around stationary horizontal circular cylinders that are fully immersed in uniform flow, mounted on or partially buried in a wall, and partially submerged with and without simulated upstream ice blocks.

2.1 Circular Cylinders in Uniform Flow

Extensive experimental and numerical studies have been conducted on canonical circular cylinders fully immersed in uniform crossflow (Gerrard 1967; Arie et al. 1981; Cantwell and Coles 1983; Norberg and Sunden 1987; Rajagopalan and Antonia 2005; Dong et al. 2006; Perret 2009; Khabbouchi et al. 2014; Yagmur et al. 2015; Capone et al. 2016; Nguyen and Lei 2022). These studies show that when a circular cylinder is fully immersed in uniform flow, the boundary layer on the cylinder separates to form a shear layer on either side of the cylinder. These separated shear layers subsequently roll up to form small-scale vortices due to the Kelvin-Helmholtz (KH) instability (Gerrard 1967; Rajagopalan and Antonia 2005; Dong et al. 2006; Perret 2009; Khabbouchi et al. 2014; Capone et al. 2016). The separated shear layers entrain ambient fluid and form large-scale von Kármán (VK) vortices, which are shed alternately from either side of the cylinder into the wake (Dong et al. 2006; Khabbouchi et al. 2014; Capone et al. 2016). The quasi-periodic shedding of these large-scale VK vortices is responsible for the unsteady loads experienced by the cylinder and can modify momentum and turbulence transport around the cylinder. The vortex shedding frequency is often expressed in dimensionless form as the Strouhal number ($St = fd/U_e$, where f, d and U_e are the vortex shedding frequency, cylinder diameter and freestream velocity, respectively). A schematic of a circular cylinder in uniform flow, along with the generic features of the mean flow, is presented in Figure 2.1 with the upstream water level

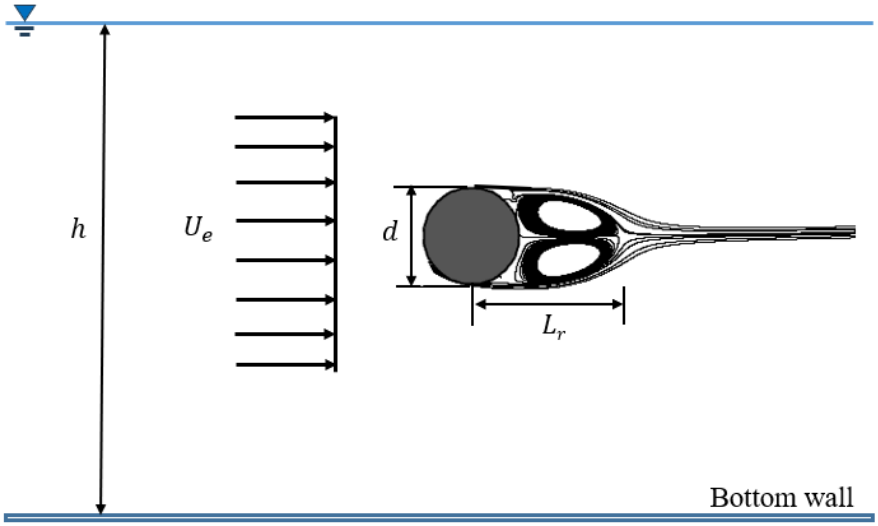

Figure 2.1. Schematic of a circular cylinder fully immersed in uniform flow.

denoted by h. As demonstrated by the mean streamlines, a recirculation bubble characterized by a pair of counter-rotating mean recirculation regions symmetric about the wake centerline forms in the wake of the cylinder. The streamwise extent of the recirculation bubble is linked to the drag forces imposed on the cylinder (Yagmur et al. 2015), and is quantified using the mean recirculation length (L_r), defined as the streamwise distance measured from the center of the cylinder to the stagnation point on the wake centerline (Dong et al. 2006; Perret 2009; Capone et al. 2016).

Past studies have investigated the effects of Reynolds number ($Re = U_e d/\nu$, where ν is the kinematic viscosity of the working fluid), freestream turbulence intensity ($Tu = u'_{rms}/U_e$, where u'_{rms} is the root-mean-square value of the streamwise velocity fluctuations), and blockage ratio (BR = d/h) on the vortex shedding frequency, drag characteristics, and turbulent transport phenomena around circular cylinders in uniform flows (Gerrard 1967; Cantwell and Coles 1983; Dong et al. 2006; Khabbouchi et al. 2014; Capone et al. 2016, Nguyen and Lei 2022). Based on Reynolds number, the flow around the cylinder is classified into the following three fundamental flow regimes: the subcritical ($400 < Re < 250\,000$), the critical ($Re \approx 250\,000$), and the supercritical

($Re > 250\,000$) regimes (Nishino 2007). Previous research has demonstrated that in the subcritical flow regime, the separation point on the cylinder surface gradually shifts backwards, and the mean recirculation length reduces with increasing Reynolds number. However, in this flow regime, the vortex shedding phenomenon around the cylinder exhibits a well-defined periodicity with a dominant peak at $St \approx 0.21$, regardless of Reynolds number (Dong et al. 2006; Khabbouchi et al. 2014; Capone et al. 2016). Khabbouchi et al. (2014) used hot-wire anemometry to examine the effects of freestream turbulence intensity ranging from 0.25% to 6.20% on the dynamics of the separated shear layers over a Reynolds number range of 4500 to 45 000. It was observed that increasing freestream turbulence intensity amplifies the unsteadiness in the separated shear layers and enhances the breakdown of the vortices in the shear layers. It was also reported that increasing freestream turbulence intensity increases the growth rates of the separated shear layers and shortens the wake formation length, defined as the streamwise distance from the mean flow separation points to the location of maximum streamwise Reynolds normal stress. Their results are in good agreement with those of Norberg and Sunden (1987) but at variance with the findings of Arie et al. (1981), who reported an elongation of the wake formation length with increasing freestream turbulence intensity. Recently, Nguyen and Lei (2022) used particle image velocimetry (PIV) to investigate the effects of blockage ratios ranging from 17% to 60%, on the separated flow dynamics around fully immersed circular cylinders at low Reynolds numbers ($Re \leq 1300$). It was observed that increasing the blockage ratio enhances the turbulence levels of the separated shear layers, and this was attributed to the interaction of wall boundary layers with the separated shear layers at higher blockage ratios.

2.2 Wall-Mounted and Partially Buried Circular Cylinders

There have been investigations on horizontal circular cylinders mounted on or partially buried in a wall (Buresti and Lanciotti 1979; Angrilli et al. 1982; Doligalski et al. 1994; Price et al. 2002; Wang and Tan 2008; Nishino and Roberts 2008; Akoz 2012; He et al. 2017). Figure 2.2 shows a schematic of the mean flow around a wall-mounted circular cylinder. In this figure and hereafter, the upstream wall boundary layer thickness is denoted by δ. The presence of the wall subjects the cylinder to wall turbulence and mean shear due to the wall boundary layer which forms upstream of the cylinder. Due to the absence of flow over the bottom side of the cylinder, a single separated shear layer forms from the top side of the cylinder. This shear layer travels over a relatively longer distance before attaching to the downstream wall, resulting in a larger recirculation bubble compared to that of a cylinder fully immersed in uniform flow. For wall-mounted circular cylinders, the recirculation length is defined as the streamwise distance measured from the center of the cylinder to the attachment point of the shear layer on the wall (Wang and Tan 2008). The absence of the lower shear layer inhibits the formation and alternate shedding of the large-scale VK vortices around wall-mounted and partially buried cylinders. Additionally, the no-slip and kinematic boundary conditions at the wall attenuate the velocity fluctuations (Price et al. 2002; Akoz 2012; He et al. 2017).

Price et al. (2002) studied the separated flow dynamics around a wall-mounted circular cylinder using flow visualization, PIV, and hot-wire anemometry over a Reynolds number range of 1200 to 5000. It was reported that although there is no regular VK vortex shedding around the wall-mounted cylinder, distinct vortex shedding motions with some degree of periodicity occur within the single shear layer. He et al. (2017) investigated the turbulent flow dynamics around a wall-mounted circular cylinder at Re = 1000 using a PIV technique and observed a similar shedding of

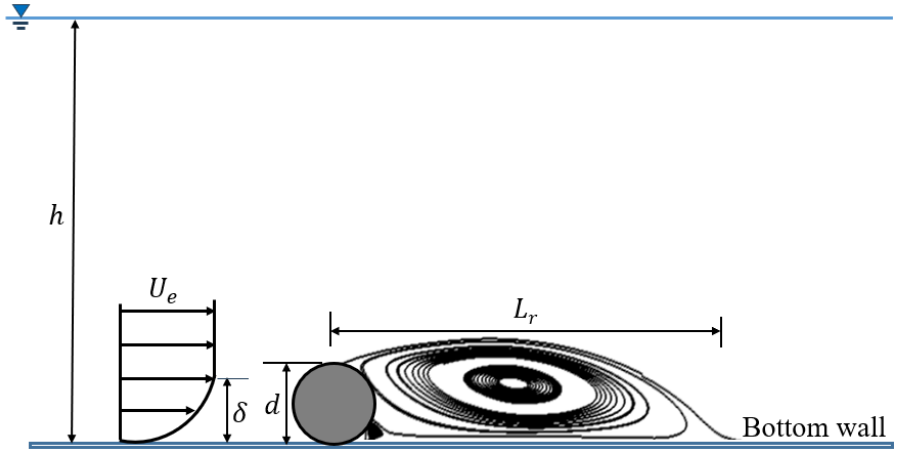

Figure 2.2. Schematic of flow around a wall-mounted circular cylinder.

these distinct vortices along the shear layer. However, the shear layer showed no distinct periodicity, and the spectra of velocity fluctuations revealed multiple frequency peaks with no discernible dominant frequency. Nishino and Roberts (2008) demonstrated using linear stability analysis that a convective-type instability, where local disturbances are swept downstream of the cylinder, dominates the wake flow of these cylinders when the VK vortex shedding phenomenon is inhibited. This is at variance with the absolute instability which prevails in the flow around cylinders in uniform flow and allows local disturbances to propagate upstream and downstream of the cylinder. Akoz (2012) studied the turbulent flow characteristics around a circular cylinder with 25% and 50% of its surface buried below a false bed over a Reynolds number range of 1000 to 7000 using PIV. It was observed that the size of the mean recirculation region decreases with exposure level of the cylinder (i.e., when the ratio of the cylinder surface exposed to the approach flow decreases). However, the levels of Reynolds stresses in the wake increase with increasing exposure level due to enhanced transport of high-momentum fluid from the ambient flow into the wake region.

2.3 Partially Submerged Circular Cylinders without Upstream Ice Blocks

The flow around stationary horizontal, partially submerged circular cylinders in open water (i.e., without upstream ice blocks) has also received some research attention (Triantafyllou and Dimas 1989; Ozdil and Akilli 2015; Bouscasse et al. 2017; Edie et al. 2021; Edie 2022; Addai et al. 2024). Figure 2.3 presents a schematic of the mean flow features around a partially submerged circular cylinder in open water, where *S* represents the submergence level of the cylinder. As observed in Figure 2.3, the flow dynamics around partially submerged circular cylinders differ considerably from those of circular cylinders in uniform flow. The absence of flow over the top of the partially submerged cylinder results in only one separated shear layer from the bottom side of the cylinder, and alternate VK vortex shedding does not occur (Triantafyllou and Dimas 1989; Ozdil and Akilli 2015; Bouscasse et al. 2017). The mean recirculation length in this case is defined as the streamwise distance measured from the center of the cylinder to the impingement point of the shear layer on the free surface. Despite some topological similarities between the flows around wall-mounted or partially buried cylinders and partially submerged cylinders, such as the formation of a relatively large mean recirculation bubble in the wake, the absence of an approach wall boundary layer in the latter implies that the separated shear layer develops differently. The free-slip and kinematic boundary conditions imposed by the free surface attenuate vertical velocity fluctuations around partially submerged cylinders. Additionally, depending on the global Froude number ($Fr_h = U_e/\sqrt{gh}$, where g is the acceleration due to gravity), the free surface may exhibit distortions, increasing the complexity of the flow around partially submerged circular cylinders.

Triantafyllou and Dimas (1989) investigated the flow dynamics around a half-submerged circular cylinder using linear stability analysis with Fr_h ranging from 0.0 to 2.5 at a Reynolds number of

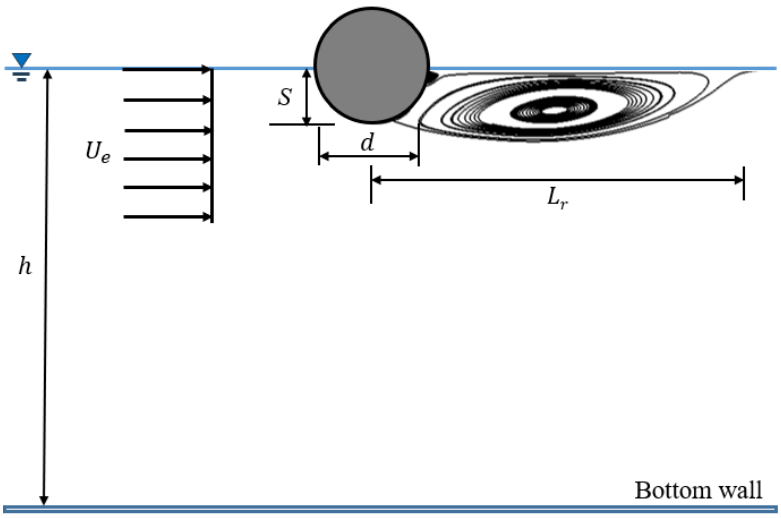

Figure 2.3. Schematic of flow around a partially submerged circular cylinder in open water.

50 000. It was observed that the free surface remains steady when $Fr_h \leq 0.5$, but large amplitude waves are formed on the free surface at higher Fr_h. It was also revealed that a convective-type instability dominates the wake flow of partially submerged circular cylinders. Other studies (Ozdil and Akilli 2015; Edie et al. 2021; Edie 2022; Addai et al. 2024) have elucidated the effects of submergence level, local Froude number, Reynolds number, and blockage ratio on the salient flow characteristics. Ozdil and Akilli (2015) and Edie et al. (2021) studied the flow dynamics around a partially submerged circular cylinder at different submergence levels ($0.25 \leq S/d \leq 0.75$) over a Reynolds number range of 5000 to 11 000 using PIV. These studies reported that the mean recirculation length, Reynolds stresses, and turbulence transport around the cylinder increase with increasing submergence level. Edie (2022) investigated the effects of local Froude numbers ($Fr_d = U_e/\sqrt{gd}$) ranging from 0.13 to 0.65 and Reynolds numbers (2900 to 26 000) on the turbulent characteristics of the flow around a half-submerged circular cylinder using PIV. It was reported that the mean recirculation length increases with both Fr_d and Re, but the Reynolds stresses are more strongly influenced by Re compared to Fr_d. More recently, Addai et al. (2024) conducted a

PIV study on the effects of blockage ratios (3.3% to 9.7%) and Reynolds numbers (2900 to 26 000) on the turbulent wake dynamics of half-submerged circular cylinders. The results were discussed in terms of the mean flow, Reynolds stresses, energy budget of turbulence kinetic energy, and the dynamics of coherent vortical structures in the wake flow. It was found that increasing Reynolds number and blockage ratio enhances the turbulence levels and the budget terms of turbulence kinetic energy but decreases the spatial coherence of vortical structures in the wake flow. The energy budget analysis also revealed that, regardless of Reynolds number and blockage ratio, the production term in the transport equation of turbulence kinetic energy acts as an energy source, while the convection term behaves as an energy sink. Consequently, the balance of the energy budget of turbulence kinetic energy is primarily determined by the diffusion term.

2.4 Partially Submerged Circular Cylinders with Upstream Ice Blocks

Previous experimental and numerical studies conducted on partially submerged circular cylinders with simulated upstream ice focused on the loads applied directly on the cylinders by moving ice blocks with no assessment of the turbulent flow dynamics (Løset and Timco 1993; Løset 1994b; Timco and Cornett 1996; Liddiard et al. 2002; Hopkins and Tuthill 2002; Morse et al. 2006). Løset and Timco (1993) experimentally investigated the effects of different ice concentrations on the loading of partially submerged circular cylinders using dynamometers. It was observed that increasing ice concentration resulted in higher loading on the cylinders. Løset (1994b) investigated the effects of ice velocities and concentrations using numerical simulations and reported that the loading on the cylinder increases linearly with increasing ice velocity and exponentially with increasing ice concentration. Timco and Cornett (1996) also examined the effects of varying thickness of upstream ice blocks on the loading of partially submerged circular cylinders. It was

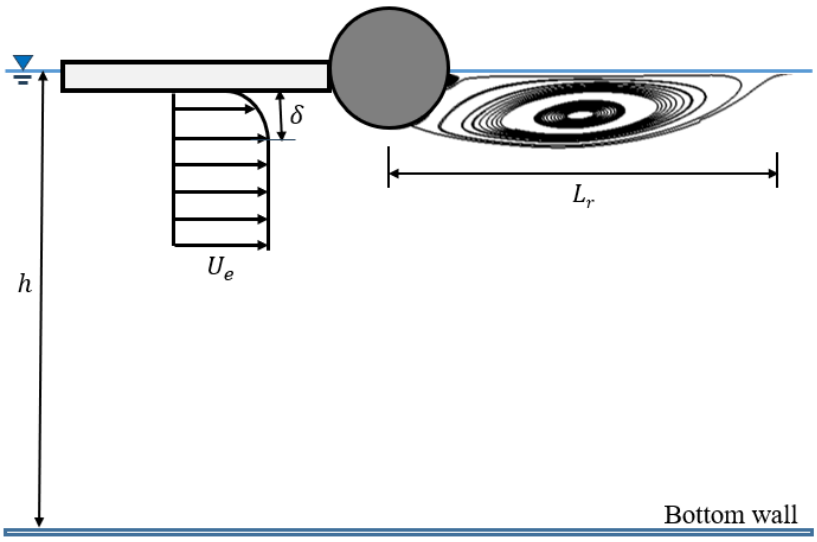

Figure 2.4. Schematic of flow around a partially submerged circular cylinder with an upstream ice block.

demonstrated that the loads imposed on cylinders increase with increasing thickness of the upstream ice blocks. As the moving ice blocks collect against the partially submerged cylinders, they juxtapose or consolidate to form a stationary ice cover which continues to elongate upstream as more ice is retained. While these studies have improved our understanding of how upstream moving ice blocks affect the loading on partially submerged circular cylinders, the influence of stationary ice blocks on the mean and turbulent flow characteristics around the cylinders is not yet understood. When a partially submerged circular cylinder is placed behind a stationary upstream ice block, it experiences wall turbulence and mean shear due to the boundary layer that forms under the ice block, as depicted in Figure 2.4. Thus, the turbulent flow dynamics around partially submerged cylinders with stationary upstream ice blocks will likely differ from those of partially submerged cylinders in open water.

2.5 Objectives

Previous research has provided valuable insights into the separated flow characteristics around partially submerged circular cylinders without upstream ice blocks, but the spatiotemporal dynamics have not yet been examined. Additionally, the effects of upstream ice blocks on the separated flow dynamics around such cylinders is not understood. Understanding the spatiotemporal dynamics of the wake flow around partially submerged circular cylinders with and without upstream ice blocks, and the effects of different conditions of upstream ice blocks on the wake dynamics would enable engineers to develop effective flow control strategies to prevent the failure of offshore structures such as ice and safety booms. Thus, the objectives of the present study are to:

1. Evaluate the effects of blockage ratio, submergence level, and a simulated upstream ice cover on the spatiotemporal dynamics of the wake flow around stationary, horizontal partially submerged circular cylinders.

2. Investigate the effects of different conditions of simulated upstream ice blocks on the mean flow and turbulence transport phenomena around stationary, horizontal partially submerged circular cylinders.

To achieve these objectives, two sets of PIV experiments were conducted around stationary, partially submerged horizontal circular cylinders with and without upstream ice blocks. In the first set of experiments, a time-resolved PIV technique was employed and the effects of blockage ratio (BR = 5% and 9%), submergence level (S/d = 0.50 and 0.75), and a simulated upstream ice cover on the spatiotemporal dynamics of the wake flow around the cylinder were examined. The results from these experiments were compared to a reference case of the cylinder fully immersed in

uniform flow. The dynamics of the wake flow are examined in terms of the instantaneous and mean flow, shear layer growth, Reynolds stresses, turbulence kinetic energy (TKE), energy budget, and transport of TKE. The unsteady characteristics are assessed using frequency spectra and temporal autocorrelation coefficients of the fluctuating velocities, proper orthogonal decomposition, and reverse flow area. The second set of experiments were performed using double-frame PIV. For these experiments, the submergence level of the cylinder was maintained at $S/d = 0.50$, and the effects of four different conditions of simulated upstream ice block: (1) an ice pan with smooth undersurface modelled using a relatively short ice block, (2) a long ice cover with smooth undersurface, (3) a long ice cover with rough undersurface, and (4) a long, thickened ice cover with rough undersurface, were examined. The results from these experiments are discussed in terms of the mean velocity and recirculation length, Reynolds stresses, energy budget of turbulence kinetic energy, turbulence transport, and two-point spatial autocorrelation coefficient of velocity fluctuations.

3 EXPERIMENTAL SETUP AND MEASUREMENT PROCEDURE

This chapter provides a description of the test facility, experimental setup and measurement procedure used for the experiments. The test cases and components of the PIV system as well as measurement uncertainties are also presented.

3.1 Test Facility

The experiments were conducted in the open recirculating water channel located in the Turbulence and Hydraulic Engineering Laboratory (THEL) at the University of Manitoba. Figure 3.1 shows a picture of the recirculating water channel which consists of a settling chamber, variable frequency drive assembly, test section, plenum, and return pipe. The side and bottom walls of the rectangular test section, which is 6000 mm long, 450 mm high and 600 mm wide, were made from smooth 31.8 mm thick Super Abrasion Resistant® transparent acrylic plates to allow optical access to the flow. An impeller pump regulated by a 30-kW variable frequency motor drives the recirculating water through the settling chamber and test section. The variable frequency drive assembly allows the velocity of the water to be varied between 0.03 m/s and 2.00 m/s. The settling chamber, installed upstream of the test section, houses the flow conditioning unit which consists of a perforated steel plate, a hexagonal honeycomb, mesh screens of different sizes, and a 4.88:1 converging section. The flow conditioning unit is employed to breakdown large-scale turbulence motions to provide uniform flow in the test section. The water exiting the test section enters a plenum containing turning vanes to divide and divert the flow into the return pipe.

3.2 PIV System

The velocity measurements were performed using a PIV system comprising a high-speed dual-

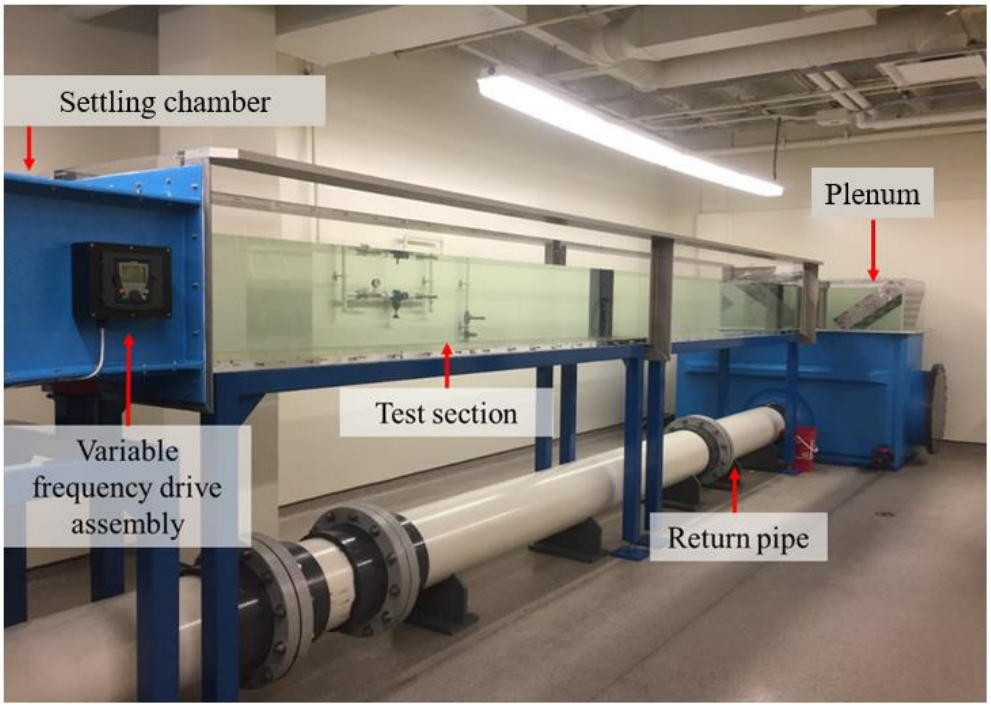

Figure 3.1. A picture of the open, recirculating water channel at the Turbulence and Hydraulic Engineering Laboratory.

cavity dual-head neodymium-doped yttrium lithium fluoride (Nd:YLF) laser, three high speed 12-bit complementary metal oxide semiconductor (CMOS) cameras, and a computer. Figure 3.2 shows a picture of the PIV system with the cameras mounted on a transverse system and the laser placed beneath the test section. The Nd:YLF laser, supplied by Photonics Industries International Inc. (Ronkonkoma, New York, USA), is used to illuminate the flow field by emitting green light of wavelength 527 nm. The energy rating of the laser is 30 mJ/pulse for each cavity. The illuminated flow field is captured using the CMOS cameras which are mounted on a transverse system to facilitate accurate positioning. The CMOS cameras can achieve image acquisition rates up to 807 Hz at a full resolution of 2560 pixel × 1600 pixel. Higher image acquisition rates up to10 kHz can be achieved but at a reduced camera resolution. The cameras are synchronized with the

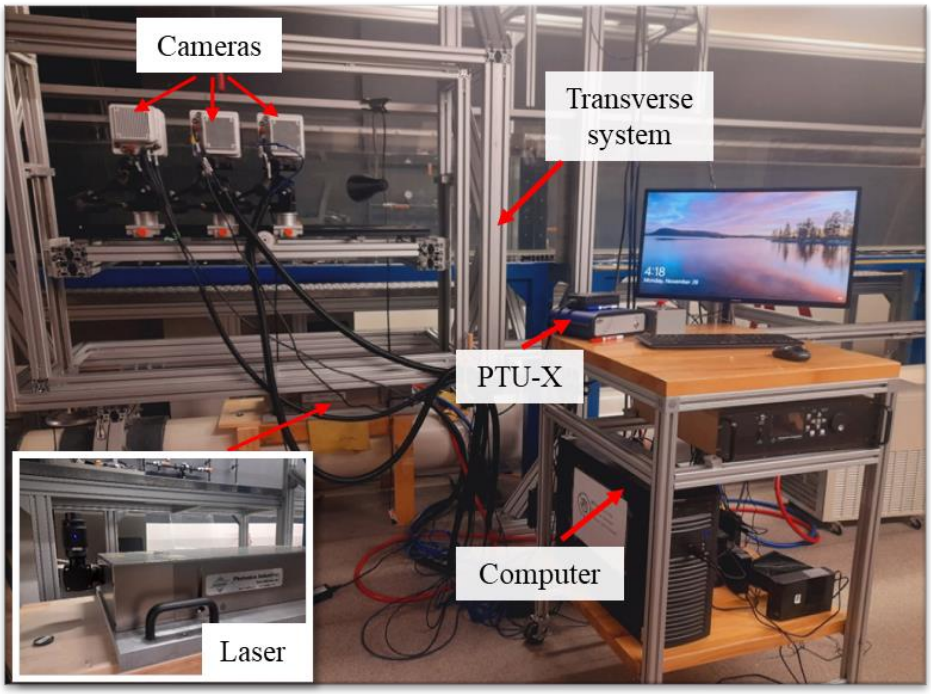

Figure 3.2. A picture showing the components of the PIV system in the Turbulence and Hydraulic Engineering Laboratory.

laser by means of a programmable timing unit (PTU–X). A commercial software (DaVis version 10.0.5) supplied by LaVision, Inc. (Göttingen, Germany) is installed on the computer and used for data acquisition, processing, and calculation of instantaneous velocity vectors.

3.3 Test Cases and Measurement Procedure

The experimental setup, test cases, measurement procedure, vector processing algorithms and uncertainty quantification used for the two sets of experiments are described in the following sub-sections.

A schematic of the side view of the experimental setup along with a simulated ice block, partially submerged circular cylinder and the fields of view (FOV) of the cameras used to image the flow field is shown in Figure 3.3. The cylinder was positioned 4000 mm away from the inlet of the test

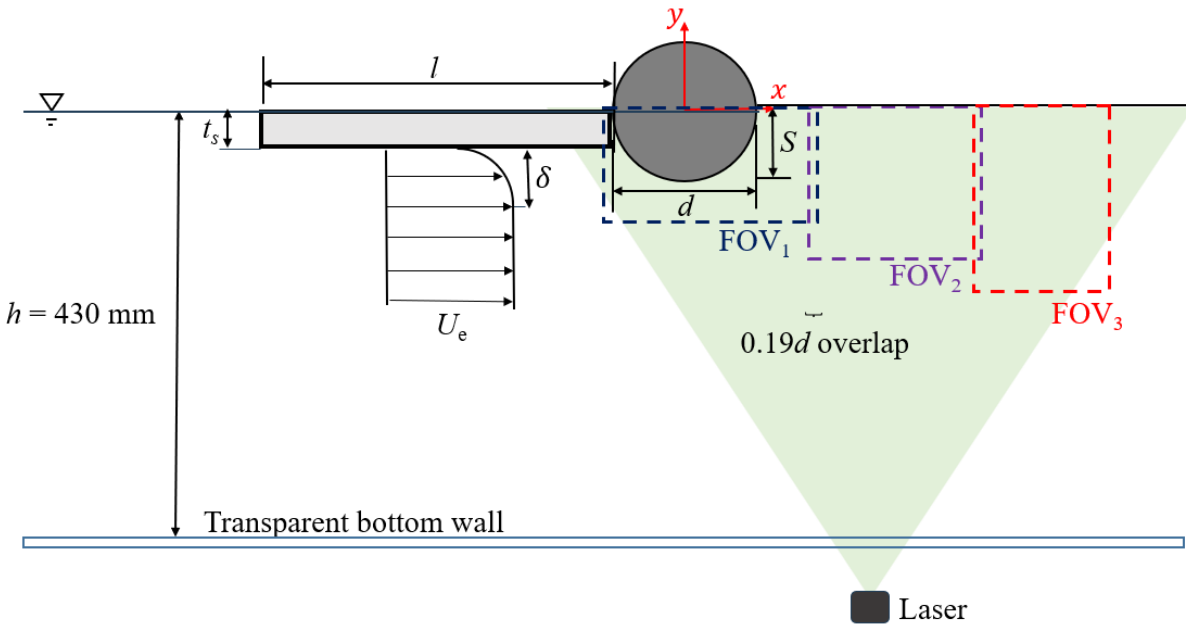

Figure 3.3. Schematic of the experimental setup (not to scale) with the fields of view (FOV) of the three cameras, nomenclature and adopted coordinate system.

section and was held rigidly in a horizontal position at the appropriate submergence level. The depth of water, measured 3500 mm away from the inlet of the test section, was kept constant at 430 mm for all test cases. The x and y coordinates are aligned with the streamwise and vertical directions, respectively, and the origin of the coordinate axes was set at the center of the cylinder. Each cylinder used in the experiments had a spanwise length (w) of 588 mm and was painted with non-reflective black paint to mitigate surface glare from laser illumination. In the experiments involving ice blocks, the simulated ice block with length l and submerged thickness t_s was mounted upstream in direct contact with the cylinder.

3.3.1 Test cases for the effects of blockage ratio, submergence level and upstream ice cover

Two circular cylinders with diameters of 26.2 mm and 51.5 mm held at different submergence levels were used in these experiments. One submergence level ($S = 0.75d$) with the smaller cylinder

Table 3.1. Summary of test cases and relevant parameters for the first set of experiments.

Test case	d (mm)	U_e (m/s)	S/d	BR	Re	Fr_S	Fr_h
UC	27.5	0.37	-	0.06	10 200	-	0.18
SC_{75}	26.2	0.39	0.75	0.05	10 200	0.89	0.20
LC_{75}	51.5	0.20	0.75	0.09	10 300	0.33	0.10
LC_{50}	51.5	0.20	0.50	0.06	10 300	0.40	0.10
$ICLC_{50}$	51.5	0.20	0.50	0.06	10 300	0.40	0.10

(hereafter denoted by SC_{75}) and two submergence levels ($S = 0.75d$ and $0.50d$) with the larger cylinder (denoted by LC_{75} and LC_{50}, respectively), without the simulated ice block, were examined. Another experiment was performed with the larger cylinder at a submergence level of $S/d = 0.5$ with the simulated upstream ice block (modelled using a smooth acrylic box) installed. The simulated ice block had a length of 2500 mm and a submerged thickness of 12 mm to mimic an ice cover. For brevity, the test case of the larger cylinder with the simulated ice cover is denoted by $ICLC_{50}$. A reference experiment was then performed with a 27.5 mm-diameter circular cylinder that was fully immersed in the uniform flow and held securely at the mid-span of the test section using a spring-wedge arrangement which was fitted to it. The test case of the circular cylinder fully immersed in the uniform flow is hereafter referred to as UC for brevity. The effective spanwise aspect ratios $w/S = 15 – 30$ for the partially submerged cylinders and $w/d = 21$ for the uniform case are larger than the value of 10 required to establish a two-dimensional mean flow at the channel mid-span (Largeau and Moriniere 2006).

The room temperature was 20°C and the kinematic viscosity of water was 1×10^{-6} m^2/s. Table 3.1 presents a summary of the different test cases and some relevant parameters including Froude numbers ($Fr_S = U_e/\sqrt{gS}$ and Fr_h), and blockage ratios calculated as S/h and d/h for the partially

submerged test cases and the fully immersed test case, respectively. The freestream velocity was varied between 0.20 m/s and 0.39 m/s, depending on the cylinder diameter, to achieve a constant Re of about 10 000. The Froude number Fr_h was less than 0.2.

3.3.2 Test cases for the effects of different upstream ice block conditions

A circular cylinder with a diameter of 77.3 mm was used for these experiments. The submergence level of the cylinder was kept constant at $S = 0.50d$, and the effective spanwise aspect ratio (w/S) was 15. Four test cases with simulated upstream ice blocks of different lengths, submerged thicknesses and undersurface conditions were considered. Table 3.2 summarizes the relevant parameters of the ice blocks and the notations assigned to each test case. The test cases of the short and long ice blocks with smooth undersurface are denoted by SIP (smooth ice pan) and SIC (smooth ice cover), respectively, whiles the long, rough undersurface ice block case is represented by RIC (rough ice cover), and the thick, long, rough undersurface ice block case by TRIC (thick, rough ice cover). The smooth undersurface cases (SIP and SIC) were modelled using smooth acrylic boxes. For the rough undersurface cases (RIC and TRIC), 16-grit sandpaper, which was also used by Nematollahi and Tachie (2018) and Fang et al. (2023), was attached to the bottom of the acrylic box to simulate the roughness. The average roughness height of the sandpaper, measured using a SMZ800N optical stereo microscope (Microscope Central, Pennsylvania, USA), is 1.54 mm (Nematollahi and Tachie 2018). The room temperature was kept at 20°C and the kinematic viscosity of water was 1×10^{-6} m^2/s. The freestream velocity was maintained at 0.33 m/s which corresponds to $Re = 25\ 500$. The Froude number Fr_h was 0.16.

Table 3.2. Summary of test cases and notations for the second set of experiments.

Notation	Ice block undersurface condition	l (mm)	t_s (mm)
SIP	Smooth	750	12
SIC		2500	12
RIC	Rough	2500	12
TRIC		2500	51

3.3.3 Measurement procedure

The water was seeded with silver-coated hollow glass spheres with average diameter (d_p) of 10 μm and density (ρ_p) of 1400 kg/m^3, supplied by Dantec Dynamics (Skovlunde, Denmark). The slip velocity (U_s) of the seeding particles was calculated using the following expression:

$$U_s = \frac{{d_p}^2(\rho_p - \rho_f)g}{18\rho_f \nu} \tag{3.1}$$

where ρ_f represents the density of the working fluid. The slip velocity of the seeding particles was calculated to be 2.18×10^{-5} m/s. The relaxation time of the seeding particles ($\tau_p = U_s/g$) and the viscous time scale ($\tau_f = \nu/U_\tau^2$, where U_τ is the friction velocity) were used to evaluate the Stokes number ($S_k = \tau_p/\tau_f$), which is useful for assessing the ability of the particles to faithfully follow the flow. The Stokes numbers ranged from 8.50×10^{-6} to 4.31×10^{-4}, which are lower than the threshold value of 0.05 (Samimy and Lele 1991), and it is concluded that the motions of the particles are true representations of the flow motions. The seeded flow was illuminated from below the test section using the Nd:YLF laser. The laser sheet was approximately 1.5 mm thick to reduce the effects of out-of-plane particle motion. The velocity measurements were performed in the x-y plane using the three CMOS cameras. They were positioned side-by-side on the traverse system

to simultaneously measure the velocity field in the symmetry plane of the cylinder. The first camera was fitted with Sigma 105 mm lens to provide higher spatial resolution to adequately resolve the dynamics of the thin shear layer around the cylinder while the second and third cameras were fitted with Nikon 60 mm lens. The dimensions ($x \times y$) of the fields of view of the first (FOV_1), second (FOV_2) and third (FOV_3) cameras were 118 mm × 74 mm, 291 mm × 137 mm, and 137 mm × 291 mm, respectively. Adjacent fields of view overlapped by 10 mm with each other in the streamwise direction and the cameras were operated at a full resolution of 2560 pixel × 1600 pixel. Initial velocity measurements were performed upstream of the position of the cylinder, without the cylinder installed, to characterize the approach flow to which the cylinder is exposed in each case.

DaVis version 10.0.5 software was used for the acquisition of particle images, and to calculate the instantaneous velocity vectors. For the first set of experiments, a total of 60 000 instantaneous images per field of view were collected at a sampling rate of 600 Hz for each test case and for the approach flow measurements using time-resolved PIV. Preliminary tests showed that this sample size was sufficient to ensure convergence of the mean velocities and higher-order turbulence statistics as well as reverse flow area. The second set of experiments as well as the approach flow measurements in these test cases were conducted using double-frame PIV. For these measurements, a total of 12 000 instantaneous images per field of view were collected at a sampling rate of 3 Hz for each test case. During data acquisition, it was ensured that the particle image diameters were within 2 to 4 pixels to minimize peak locking and ensure valid detection of correlation peak. The instantaneous velocity vectors were calculated using a graphical processing unit (GPU)-accelerated multi-pass cross-correlation algorithm in the DaVis version 10.0.5 software. The vector calculation procedure included an initial pass (with a grid size of 128 pixel × 128 pixel and 50% overlap) and four final passes (each having a grid size of 24 pixel × 24 pixel

and 75% overlap). The vector spacings were 0.31 mm, 0.52 mm, and 0.52 mm for FOV_1, FOV_2, and FOV_3, respectively. Analyses of the animations of the raw PIV images showed that the oscillations of the downstream free surface were negligible (less than 0.5 mm). Thus, it is concluded that the free surface is steady, and the effects of free surface waves on the flow characteristics are negligible. In-house MATLAB scripts were used to post-process the instantaneous velocity vectors. The instantaneous velocities in the x and y directions are represented by u and v, respectively. An overbar $\overline{(\cdot)}$ denotes time averaging and an upper case represents mean velocity. The instantaneous velocities are decomposed into mean and fluctuating components using Reynolds decomposition as: $u' = u - U$, where u' is the fluctuating component.

3.4 Measurement Uncertainty

Measurement uncertainties in the mean velocities and Reynolds stresses are quantified using the method outlined by Sciacchitano and Wieneke (2016) and Essel et al. (2021) as follows:

$$\xi_U = \frac{Z_c}{\sqrt{N}} \frac{u_{rms}}{U} \tag{3.2}$$

$$\xi_{\overline{u'u'},\overline{v'v'}} = Z_c \sqrt{\frac{2}{N}} \tag{3.3}$$

$$\xi_{\overline{u'v'}} = Z_c \sqrt{\frac{1+\rho_{uv}{}^2}{N-1}} \tag{3.4}$$

where N, Z_c and ρ_{uv} represent the number of uncorrelated samples, the 95% confidence coefficient (Z_c = 1.96), and the correlation coefficient, respectively. For the DF-PIV measurements, the measurement uncertainties for the mean velocity, Reynolds normal stresses, and Reynolds shear stresses were calculated to be less than 2%, 6% and 4% of their peak values, respectively. Since the TR-PIV samples are not statistically independent, it was necessary to determine the effective

number of samples (N_{eff}) over the sampling time T that contribute to statistical convergence using the expression:

$$N_{eff} = \frac{T}{2T_{int}} \tag{3.5}$$

where T_{int} is the integral time scale evaluated from the temporal autocorrelations of the streamwise velocity fluctuations. Using this method, the TR-PIV measurement uncertainties for the mean velocity, Reynolds normal stresses, and Reynolds shear stresses were calculated to be less than 5%, 9% and 7% of their peak values, respectively.

4 RESULTS AND DICUSSION

The results from the first and second sets of experiments in this present study are, respectively, presented and discussed in Section 4.1 and Section 4.2 of this chapter. These main sections are organized into subsections. For Section 4.1, the approach flow and boundary layer are analyzed in the first subsection whiles the instantaneous and mean flow characteristics are examined in the second subsection. The third subsection discusses the Reynolds stresses and turbulence kinetic energy (TKE). The budget terms of TKE and TKE transport are analyzed in the fourth subsection. The remaining subsections investigate the unsteady wake characteristics using frequency spectra and temporal autocorrelation coefficients of the fluctuating velocities, proper orthogonal decomposition, and reverse flow area. For Section 4.2, the approach boundary layers are characterized in the first subsection, and the characteristics of the mean flow are examined in the second subsection. The Reynolds stresses and TKE are discussed in the third subsection, and the budget terms of TKE as well as the transport of TKE are analyzed in the fourth subsection. The last subsection examines the evolution of coherent vortical structures in the wake flow using two-point spatial autocorrelation coefficients.

In the following analyses, spurious data above the cylinder in the uniform flow, caused by the shadow cast due to illuminating the flow from below the test section, and at the air-water interface in the partially submerged cases due to the distortion of the laser sheet, are masked out.

4.1 Effects of Blockage Ratio, Submergence Level and Upstream Ice Cover

The effects of blockage ratio, submergence level and a simulated upstream ice cover on the spatiotemporal dynamics of the wake flow around partially submerged circular cylinders are discussed in this section. The results are compared to the case of the cylinder fully immersed in

uniform flow. The test cases from the first set of experiments (UC, SC_{75}, LC_{75}, LC_{50} and $ICLC_{50}$) are used. The discussions presented here are from the following papers: Israel, M. K., Dow, K., Clark, S. P., and Tachie, M. F. (2024), "Experimental investigation of the turbulent wake of partially submerged horizontal circular cylinders," International Journal of Heat and Fluid Flow, **109**, 109509. DOI: 10.1016, and Israel, M. K., Dow, K., Clark, S. P., and Tachie, M. F. (2024), "Spatiotemporal characteristics of turbulent flows around partially submerged circular cylinders," submitted to Flow, Turbulence and Combustion on 7th June 2024.

4.1.1 Approach flow and boundary layer

The approach flow and boundary layer are assessed using the velocity measurements performed in the absence of the cylinders because the nature of the approach flow and boundary layer plays an important role in the flow structure around the cylinders. For the uniform flow case (UC) and the cases of the partially submerged cylinders without upstream ice cover (SC_{75}, LC_{75}, and LC_{50}), the mean velocity of the approach flow was measured to be uniform to 0.2%, and the turbulence intensity was 0.75%. The boundary layer beneath the simulated ice cover in $ICLC_{50}$ is examined using the vertical profiles of dimensionless streamwise mean velocity and Reynolds stresses ($\overline{u'u'}$, $\overline{v'v'}$, and $\overline{u'v'}$) shown in Figure 4.1.1. These profiles were extracted at a streamwise location $0.2d$ upstream of the trailing edge of the simulated ice cover. The boundary layer thickness, defined as the vertical distance from the ice block undersurface to the location where $U = 0.99U_e$, is $\delta = 0.52d$. At the elevation corresponding to the submergence level ($y = 0.5d$), the streamwise mean velocity is $0.96U_e$, and the turbulence intensity (Tu) decreased from its near-wall peak to 2.90%. Thus, for $ICLC_{50}$, the submerged cylinder is fully immersed in the boundary layer beneath the ice cover since $\delta > S$, and it is exposed to a turbulence level of 2.90% or higher.

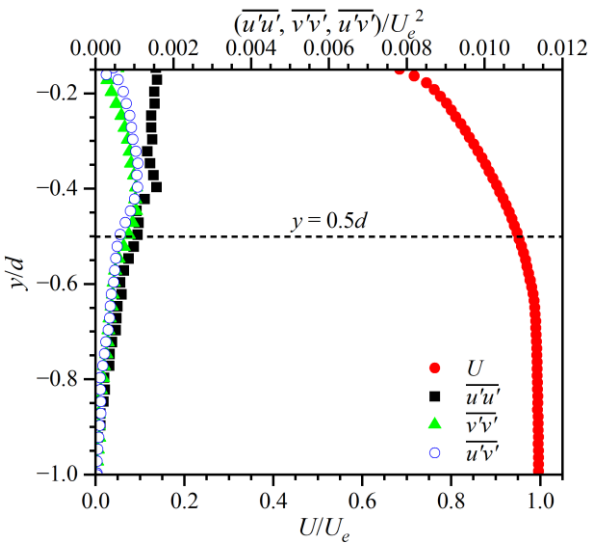

Figure 4.1.1. Vertical profiles of dimensionless streamwise mean velocity and Reynolds stresses of the approach boundary layer in $ICLC_{50}$.

4.1.2 Instantaneous and mean flow

4.1.2.1 Instantaneous flow field

The swirling strength method proposed by Zhou et al. (1999) is used to visualize the instantaneous vortical structures. The swirling strength is defined as the imaginary part of the complex eigenvalue of the local velocity gradient tensor and is an effective vortex indicator as it reveals swirling motions (vortices) produced from pure fluid rotation while ignoring regions of intense shear. Since a planar PIV technique was used in the present study, the complete velocity gradient is not available. Therefore, following the approach used by Chen et al. (2014), a two-dimensional swirling strength, defined based on the in-plane (x-y) velocity gradients as:

$$\Lambda = \frac{1}{2}\left(\frac{\partial u}{\partial x} + \frac{\partial v}{\partial y}\right) \pm \frac{1}{2}\sqrt{\underbrace{\left(\frac{\partial u}{\partial x} + \frac{\partial v}{\partial y}\right)^2}_{b^2} - \underbrace{4\left(\frac{\partial u}{\partial x}\frac{\partial v}{\partial y} - \frac{\partial v}{\partial x}\frac{\partial u}{\partial y}\right)}_{4ac}} \tag{4.1}$$

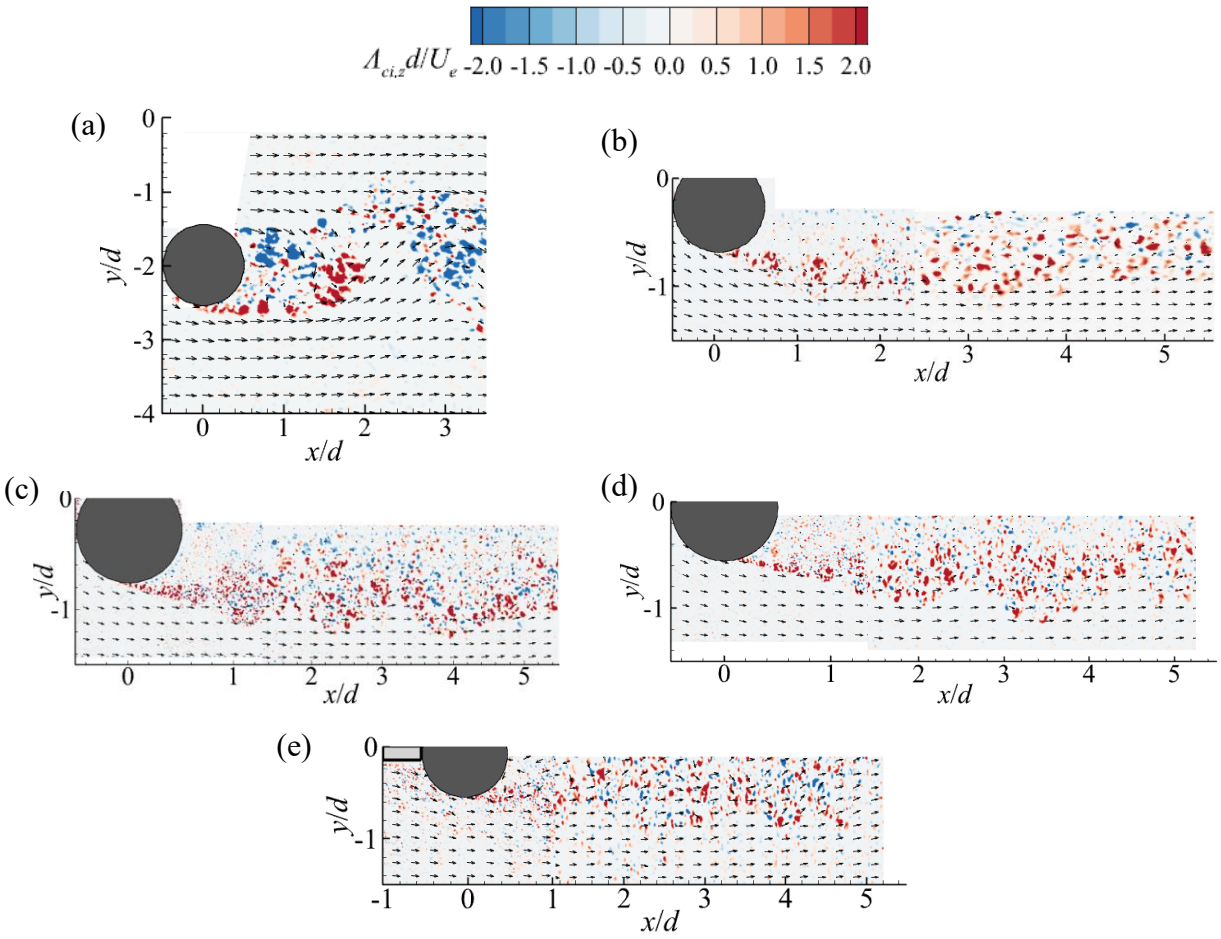

Figure 4.1.2. Instantaneous snapshots of signed swirling strengths ($\Lambda_{ci,z}$) superimposed with velocity vectors for (a) UC, (b) SC_{75}, (c) LC_{75}, (d) LC_{50}, and (e) $ICLC_{50}$. The spurious data in the region above the cylinder for UC and at the air-water interface for the partially submerged test cases are masked out.

is employed. Here, the magnitude of the local swirling motion is quantified by $\Lambda_{ci} = \sqrt{|b^2 - 4ac|}$, where $4ac > b^2$, and is evaluated at locations where the solution to Λ is complex and zero elsewhere. However, because $\Lambda_{ci} \geq 0$, it does not provide the directions of rotations. To recover the signs of the swirling motions, the magnitudes of the swirling strength are multiplied by the signs of the in-plane instantaneous fluctuating vorticities $\left(\omega_z = \frac{\partial v}{\partial x} - \frac{\partial u}{\partial y}\right)$, such that $\Lambda_{ci,z} = \Lambda_{ci} \times (\omega_z/|\omega_z|)$, as demonstrated by Wu and Christensen (2006).

Figure 4.1.2 presents typical snapshots of the signed swirling strengths for the different test cases. The topologies reveal prograde (blue patches) and retrograde (red patches) vortices, representing clockwise and counterclockwise swirling motions, respectively. In all cases, the approach flow separates at the cylinder surface and forms separated shear layers. These shear layers break down and roll up into small-scale vortices due to the KH instability. In the UC case, the lower shear layer crosses the wake centerline and entrains ambient fluid from the upper wake to form a VK vortex. Further downstream of the cylinder, a VK vortex from the upper side of the cylinder entrains ambient fluid from the lower wake.

The snapshots for the partially submerged cases are qualitatively similar to each other. In these cases, the separated shear layer rolls up into small-scale retrograde structures which are shed into the wake. While this occurs, prograde structures are produced at the free surface and drawn into the wake. The prograde and retrograde structures collide erratically and pair up to form clusters of relatively larger vortices which subsequently break down into smaller vortices as they convect downstream into the wake. Rajagopalan and Antonia (2005) suggested that concurrent pairing up and breaking down of small-scale vortices along separated shear layers is due to a convective instability. Triantafyllou and Dimas (1989) demonstrated that a convective-type instability, where local disturbances are swept downstream of the cylinder, dominates the wake flow of partially submerged circular cylinders. Thus, the prevalent pairing up and breaking down of small-scale vortices in the wake of the partially submerged test cases is attributed to the dominance of convective instability.

4.1.2.2 Mean flow

Figure 4.1.3 presents contours of dimensionless streamwise (U/U_e) and vertical (V/U_e) mean velocities overlaid with mean streamlines to examine the mean flow features around the cylinders. In this and subsequent figures, only the lower half of the wake of UC is shown for conciseness since the wake is symmetric about its centerline. Regardless of submergence level and upstream flow condition, the mean flow deflects downwards as it approaches the cylinder and accelerates around the cylinder due to the reduced section imposed by the cylinder resulting in a region of elevated U/U_e beneath the cylinder. The mean flow subsequently recovers upwards towards the wake centerline (UC) and free surface (partially submerged cases) downstream of the cylinder. The magnitudes of the local maxima of the mean velocities are indicated on the plots and their locations are marked using green "+" symbol. The mean streamlines in UC show formation of a mean recirculation bubble, entrapped by the wake centerline and the lower separated shear layer. For the partially submerged cases, on the other hand, the separated shear layer and the free surface encompass a mean recirculation bubble characterized by a large primary vortex and a small secondary vortex (SV) which formed at the intersection of the cylinder and the free surface. The mean streamline, traced from the mean flow separation point on the cylinder to the point on the wake centerline (UC) or free surface (partially submerged cases) where the streamwise mean velocity is zero, is identified as the mean separating streamline. The isopleth of $U = 0$ (red dashed line), which extends from the mean flow separation point, is used to demarcate the mean reverse flow area of the recirculation bubble. The mean recirculation length is defined as the streamwise distance measured from the center of the cylinder to the point where the $U = 0$ isopleth intercepts with the wake centerline and free surface for UC and partially submerged cases, respectively.

Table 4.1.1 presents a summary of the local maximum streamwise mean velocity (U_{max}/U_e) and

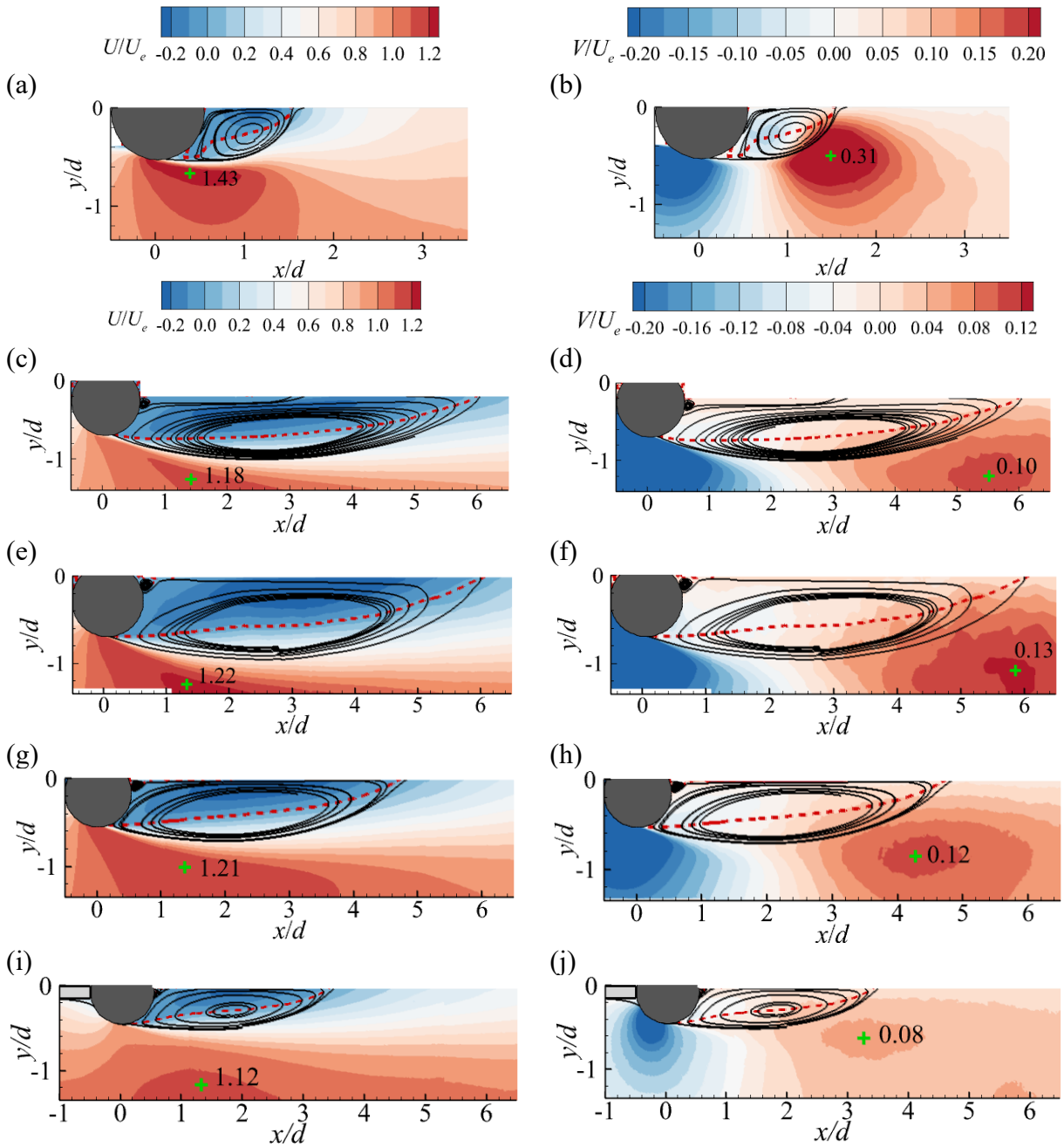

Figure 4.1.3. Contours of dimensionless streamwise (left) and vertical (right) mean velocities for UC (a, b), SC_{75} (c, d), LC_{75} (e, f), LC_{50} (g, h), and $ICLC_{50}$ (i, j). The isopleths of $U = 0$ (red dashed line) and mean streamlines are superimposed on the contour plots. The locations (green '+' symbol) and magnitudes of peak values are also indicated. The spurious data at the air-water interface for the partially submerged test cases is masked out.

its location (x_u/d, y_u/d), maximum backflow velocity (U_b/U_e), and mean recirculation length (L_r/d). For the partially submerged cases, the mean recirculation length was estimated by

Table 4.1.1. Summary of critical values from the mean flow topology.

Test case	U_{max}/U_e	$x_u/d,\ y_u/d$	U_b/U_e	L_r/d
UC	1.43	0.35, -0.72	-0.22	1.38
SC_{75}	1.18	1.40, -1.25	-0.30	6.24
LC_{75}	1.22	1.38, -1.23	-0.32	6.23
LC_{50}	1.21	1.36, -1.00	-0.34	4.80
$ICLC_{50}$	1.12	1.30, -1.20	-0.28	3.70

extrapolating the isopleth of $U = 0$ to the free surface. The metrics presented in Table 4.1.1 are often used to characterize the mean flow around bluff bodies (Dong et al. 2006; Akoz 2012; Essel et al. 2015; Capone et al. 2016; Addai et al. 2024). For the uniform flow case, $U_{max}/U_e = 1.43$ which is larger than $U_{max}/U_e = 1.18 \pm 0.06$ observed for the partially submerged cases. Also, U_{max} occurs closer to the cylinder in uniform flow compared to those partially submerged beneath the free surface. These results indicate that the acceleration of the mean flow around cylinders in uniform flow is more intense compared to those around partially submerged cylinders. In contrast, the maximum backflow velocities for the partially submerged cases are 27% to 55% larger, and the mean recirculation lengths are 168% to 352% longer compared to the uniform case. The comparatively shorter recirculation length and lower backflow velocity for the uniform case is due to the interaction between the two oppositely signed separated shear layers, which are absent in the partially submerged cases. These results are in qualitative agreement with the previous investigation by Agyei-Agyemang et al. (2023) on square cylinders, which reported that when placed adjacent to a free surface, the recirculation length is 713% longer than that of a square cylinder in uniform flow. It is worth noting that the values of U_b/U_e and L_r/d for UC are in good agreement with $U_b/U_e = -0.23$ and $L_r/d = 1.36$ reported by Dong et al. (2006) for a circular cylinder

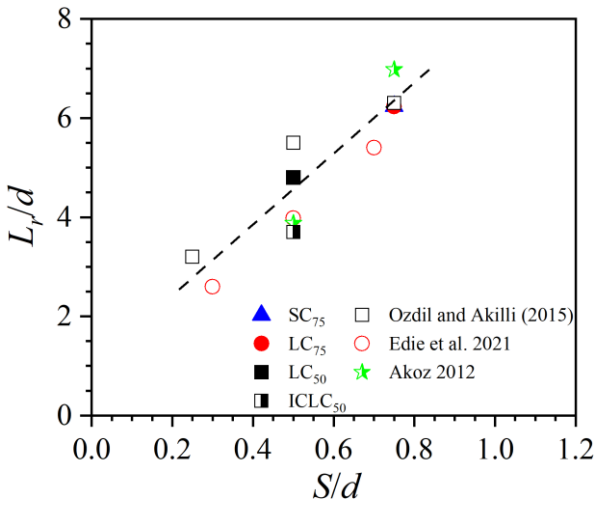

Figure 4.1.4. Comparison of the mean recirculation lengths of the partially submerged cases in this present study with previous investigations on partially submerged and partially buried circular cylinders.

in uniform flow at $Re = 10\,000$. For the cases of the partially submerged cylinders without upstream ice cover, the magnitudes of U_b/U_e are within 0.32 ± 0.02. However, the mean recirculation length reduced from $L_r/d \approx 6.2$ (SC_{75} and LC_{75}) to 4.8 (LC_{50}) which may be due to the closer proximity of the separated shear layer to the free surface at the smaller submergence level. It is also observed that an upstream ice cover reduces the maximum backflow velocity and mean recirculation length compared to the case of a partially submerged cylinder without an upstream ice cover as evidenced by the smaller magnitudes of U_b/U_e and L_r/d for $ICLC_{50}$ compared to those of LC_{50}. This observation is attributed to the higher turbulence intensity of the approach boundary layer underneath the ice cover in $ICLC_{50}$, which promotes entrainment of high momentum fluid from the ambient flow into the wake of the cylinder and shortens the recirculation length (Khabbouchi et al. 2014; Essel et al. 2015, Fang and Tachie 2020; Chalmers et al. 2023).

The mean recirculation lengths for the partially submerged cases in this present study are compared to previous results for partially submerged (Ozdil and Akilli 2015; Edie et al. 2021) and partially

buried (Akoz 2012) circular cylinders in Figure 4.1.4. Good agreement is observed between the present and previous studies. The plot indicates that the mean recirculation length tends to increase linearly with increasing exposure level (i.e., when the ratio of the cylinder surface exposed to the approach flow increases). The correlation between recirculation length and exposure level determined using the least squares method, is $L_r/d = 7.25S/d + 0.85$ with an R-squared value of 0.85.

4.1.2.3 Shear layer

Given the similarity in the initial downstream development between plane mixing layers and separated shear layers, it is customary to use the vorticity thickness proposed by Brown and Roshko (1974) for plane mixing layers to characterize the growth rate of separated shear layers (Akon and Kopp 2018; Fang and Tachie 2019a; Essel et al. 2021). The vorticity thickness is defined as:

$$\delta_\omega = (U_{max} - U_{min})/(\partial U/\partial y)_{max} \tag{4.2}$$

where U_{max} and U_{min} are the local maximum and minimum of streamwise mean velocity, respectively, along the separated shear layer.

Figure 4.1.5(a) shows the streamwise variation of the vorticity thickness along the separated shear layer. Two linear regions with different growth rates are observed in the profiles. Specifically, the region of the separated shear layer that encompasses the first half of the mean recirculation region (Region 1) has a lower growth rate compared to the region that bounds the second half (Region 2). Khabbouchi et al. (2014) also identified these two regions for a circular cylinder in a uniform flow and suggested that Region 1 is associated with the development of instabilities while Region 2

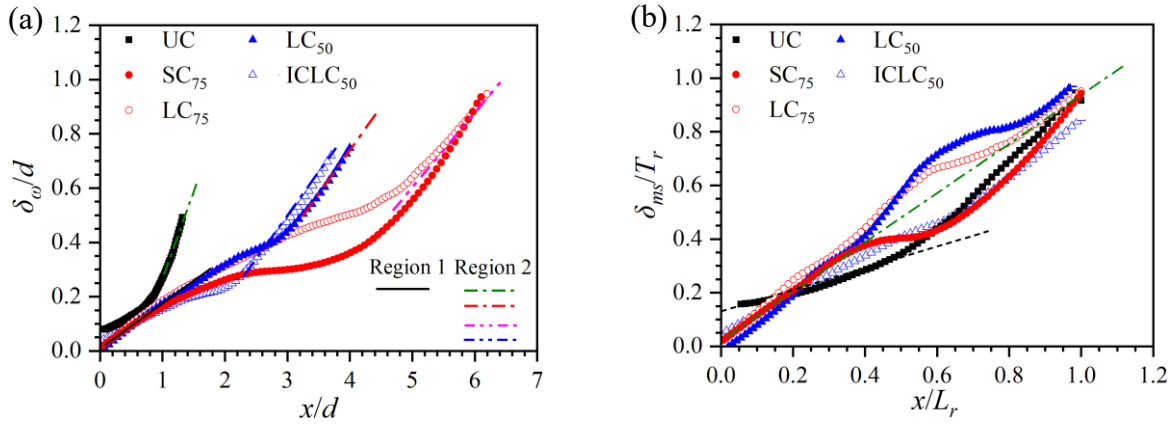

Figure 4.1.5. Streamwise variation of the (a) vorticity thickness δ_ω/d and (b) maximum slope thickness δ_{ms}/T_r.

defines the fully turbulent region of the separated shear layer. The profiles for the partially submerged cases reveal a near-flattening of vorticity thickness between Region 1 and Region 2. Castro and Haque (1987) and Lyn and Rodi (1994), who studied separated shear layers bounding mean recirculation regions over sharp-edged bluff bodies, also reported profiles similar to those observed here for the partially submerged test cases. Lyn and Rodi (1994) explained that the near flattening of vorticity thickness in the mid-region of separated shear layers is due to a "funnelling" effect caused by the opposing actions of the mean recirculation region and the freestream flow, which maintain velocity gradients across the separated shear layer.

A summary of the growth rates ($\mathrm{d}\delta_\omega/\mathrm{d}x$) of the two linear regions in each test case is presented in Table 4.1.2. For Region 1, the growth rate for the uniform case is 0.13 which is comparable to 0.17 for the partially submerged cases. However, for Region 2, the growth rate for the uniform case is 43% to 63% higher than the values for the submerged cases. The values of $\mathrm{d}\delta_\omega/\mathrm{d}x$ for Region 1 for all cases and for Region 2 of SC_{75} and LC_{75}, are in good agreement with 0.14–0.22 reported for plane mixing layers (Brown and Roshko 1974), 0.15 for square prisms in uniform flow (Lander et al. 2016) and 0.11–0.18 for free surface-attaching jets (Rahman and Tachie 2019).

Table 4.1.2. Summary of shear layer growth rates.

Test case	$\mathrm{d}\delta_\omega/\mathrm{d}x$	
	Region 1	Region 2
UC	0.13	0.67
SC_{75}	0.17	0.25
LC_{75}	0.17	0.25
LC_{50}	0.17	0.35
$ICLC_{50}$	0.17	0.38

The maximum slope thickness, defined as:

$$\delta_{ms} = (U_{max})/(\partial U/\partial y)_{max} \tag{4.3}$$

is an alternative approach to quantify the growth of a separated shear layer (Kiya et al. 1982; Cherry et al. 1984; Akon and Kopp 2018). As shown in equations (4.2) and (4.3), the difference between the vorticity thickness and maximum slope thickness is how U_{min} is treated. In the latter, U_{min} = 0. Figure 4.1.5(b) illustrates the streamwise development of maximum slope thickness along the separated shear layer. Following Akon and Kopp (2018), the streamwise and vertical coordinates are scaled by the mean recirculation length (L_r) and maximum thickness (T_r) of the recirculation bubble, respectively. Figure 4.1.5(b) shows that, within the first half of the recirculation region, the profiles of the partially submerged cases collapse to a linear distribution with a slope of 0.95 which is higher than 0.48 for the initial stage of the uniform flow case. Nonetheless, the slope of the linear distribution for the partially submerged cases is comparable to 1.14 reported by Akon and Kopp (2018) for separated and reattached flows over two- and three-dimensional wall-mounted bluff bodies.

4.1.3 Reynolds stresses and turbulence kinetic energy

The Reynolds stresses and turbulence kinetic energy are used to examine the characteristics of the fluctuating velocity field. Figure 4.1.6 shows contours of the streamwise ($\overline{u'u'}$) and vertical ($\overline{v'v'}$) Reynolds normal stresses. The mean separating streamlines (the solid black lines) are superimposed, and the magnitudes of local peaks are indicated on the plots with their locations marked using green "+" symbol. For the uniform flow case, the streamwise Reynolds normal stress concentrates along the mean separating streamline, while the vertical component is concentrated along the wake centerline with a peak magnitude that is 48% higher compared to the streamwise component. The dominance of vertical fluctuating velocities (v') is a direct consequence of the formation of VK vortices in the wake of the cylinder fully immersed in the uniform flow (Cantwell and Coles 1983; Dong et al. 2006; Perret 2009).

Due to the lack of alternate vortex shedding in the partially submerged cases, both the streamwise and vertical Reynolds normal stresses are concentrated along the shear layer but in these cases, the streamwise component is comparatively larger than the vertical component. This observation is in qualitative agreement with previous studies on partially submerged cylinders (Ozdil and Akilli 2015; Edie et al. 2021; Addai et al. 2024) as well as partially buried and wall-mounted cylinders (Wang and Tan 2008; Akoz 2012; He et al. 2017). The unequal magnitudes of the Reynolds stresses also highlight the anisotropic nature of the wake flow around the cylinders. For LC_{75} and LC_{50}, $\overline{u'u'}_{max}$ and $\overline{v'v'}_{max}$ are nearly the same but comparatively higher than SC_{75}. This suggests that an increase in blockage ratio enhances the turbulence levels in the wake of partially submerged circular cylinders, in agreement with the findings of Addai et al. (2024). The presence of an ice cover upstream of the partially submerged cylinder ($ICLC_{50}$) reduces the magnitudes of $\overline{u'u'}_{max}$ and $\overline{v'v'}_{max}$ by 40% and 25%, respectively, compared to the case without an ice cover (LC_{50}).

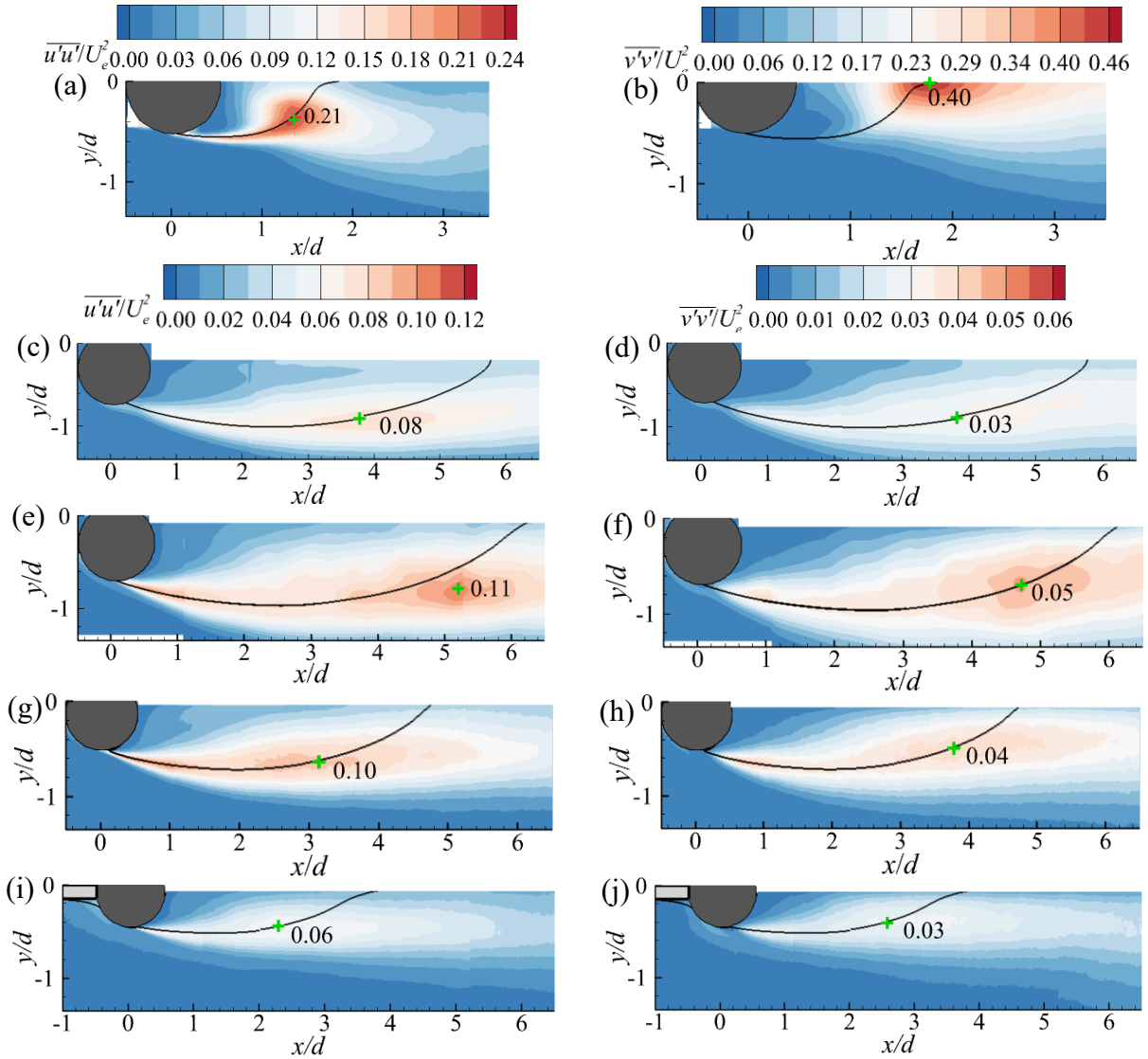

Figure 4.1.6. Contours of dimensionless streamwise (left) and vertical (right) Reynolds normal stresses for UC (a, b), SC_{75} (c, d), LC_{75} (e, f), LC_{50} (g, h), and $ICLC_{50}$ (i, j). The solid black line is the mean separating streamline. The locations (green '+' symbol) and magnitudes of peak values are also indicated. A white rectangle is used to mask spurious data at the air-water interface. Different contour levels are used for UC while the same contour levels are used in the partially submerged cases.

Meanwhile, the wake formation length, defined as the streamwise distance from the center of the cylinder to the location of $\overline{u'u'}_{max}$ (Griffin 1995; Bai and Alam 2018), is significantly shorter for UC compared to the submerged cases. For the partially submerged cylinders, the wake formation length increases with increasing blockage ratio and decreases with decreasing submergence level

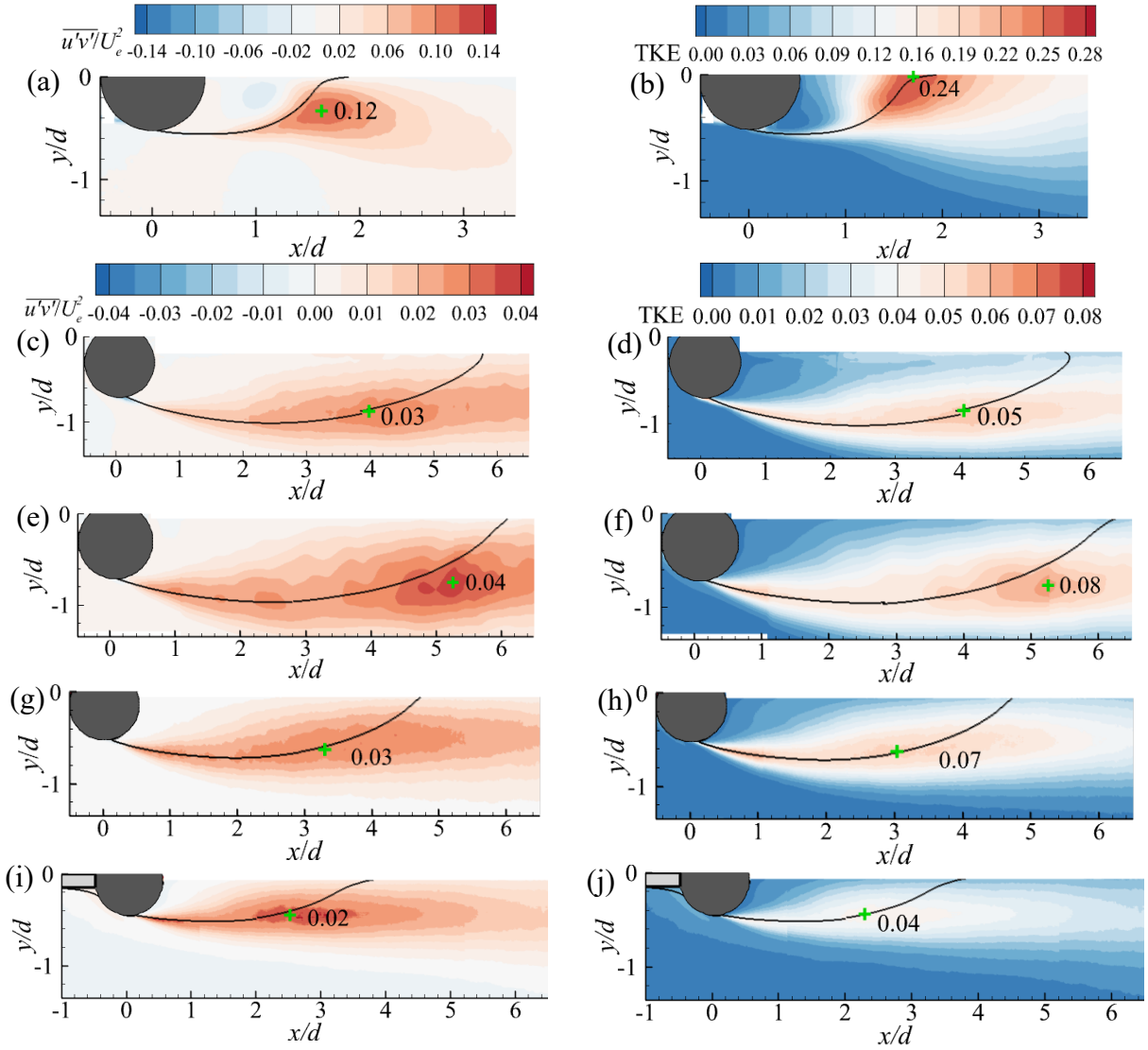

Figure 4.1.7. Contours of dimensionless Reynolds shear stress (left) and turbulence kinetic energy (right) for UC (a, b), SC_{75} (c, d), LC_{75} (e, f), LC_{50} (g, h), and $ICLC_{50}$ (i, j). The solid black line is the mean separating streamline. The locations (green '+' symbol) and magnitudes of peak values are also indicated. A white rectangle is used to mask spurious data at the air-water interface. Different contour levels are used for UC while the same contour levels are used in the partially submerged cases.

as evidenced by the further upstream location of $\overline{u'u'}_{max}$ in SC_{75} and LC_{50} compared to that of LC_{75}. The wake formation length of $ICLC_{50}$ is also shorter than that of LC_{50}.

The contours of dimensionless Reynolds shear stress ($\overline{u'v'}$) and turbulence kinetic energy are shown in Figure 4.1.7. Since the spanwise velocity fluctuations were not measured, the turbulence

kinetic energy was estimated as TKE = $0.5(\overline{u'u'} + \overline{v'v'})$. For the cylinder in uniform flow, the maximum Reynolds shear stress occurs along the mean separating streamline, but the maximum turbulence kinetic energy occurs along the wake centerline due to the dominance of $\overline{v'v'}$. In contrast, for the partially submerged cylinders, the maximum Reynolds shear stress and turbulence kinetic energy occur at similar locations along the mean separating streamline, regardless of submergence level and upstream flow condition. The maximum values of $\overline{u'v'}$ and TKE for the partially submerged test cases are 66% to 83% and 67% to 84%, respectively, lower compared to that of UC.

4.1.4 Budget of turbulence kinetic energy and turbulence transport

The budget terms of TKE are examined to provide insights into the sources of turbulence production, as turbulence production correlates with the levels of Reynolds stresses and TKE. The transport equation of TKE for a statistically steady flow is given by:

$$0 = P_k + C_k + D_k + \varepsilon_k \tag{4.4}$$

where P_k, C_k, D_k and ε_k represent the production, convection by the mean flow, diffusion, and dissipation of TKE, respectively.

Here, the flow statistics are homogeneous in the spanwise direction and the spanwise mean velocity is zero. Also, since the fluctuating pressure was not measured, its contribution to the diffusion term is not included in the following analysis. Even though the contribution from viscous diffusion was included, it is orders of magnitude lower compared to that from turbulence diffusion. Additionally, the dissipation term is omitted from these analyses because the spatial resolution used in the present measurements was not sufficient to resolve the Kolmogorov scales at which

turbulence dissipation occurs. With these assumptions and simplifications, the individual budget terms in equation (4.4) can be expressed as follows:

$$P_k = -\overline{u'u'}\frac{\partial U}{\partial x} - \overline{v'v'}\frac{\partial V}{\partial y} - \overline{u'v'}\frac{\partial U}{\partial y} - \overline{u'v'}\frac{\partial V}{\partial x} \tag{4.5}$$

$$C_k = -U\frac{\partial k}{\partial x} - V\frac{\partial k}{\partial y} \tag{4.6}$$

$$D_k = \frac{\partial}{\partial x}\left(\nu\frac{\partial k}{\partial x} - \overline{u'u'u'} - \overline{u'v'v'}\right) + \frac{\partial}{\partial y}\left(\nu\frac{\partial k}{\partial y} - \overline{u'u'v'} - \overline{v'v'v'}\right) \tag{4.7}$$

The contour plots of dimensionless production (P_k) term are shown in Figure 4.1.8. The magnitudes of P_k at the location of maximum production and the location of maximum TKE (from Figure 4.1.7(b, d, f, h, j)) are indicated on the plots, with their locations respectively marked using green "+" and black "x" symbols. Similar to the turbulence kinetic energy, the production term is concentrated along the mean separating streamlines. The positive values of P_k along the separated shear layers show that the production term is a primary source of the turbulence kinetic energy (Cimarelli et al. 2019; Addai et al. 2024; Lui et al. 2024). The location of maximum production coincides with the location of maximum TKE on the wake centerline in the uniform flow case, but for the partially submerged cylinders, the maximum production occurs upstream of the location of maximum TKE. It is also evident that the levels of P_k are significantly lower for the partially submerged cases (in conformity with the lower levels of Reynolds stresses and TKE) than the uniform flow case. For the partially submerged cylinders, the magnitude of maximum P_k increased by 19% from SC_{75} to LC_{75} when blockage ratio was increased, but the maximum P_k values are similar for LC_{75} and LC_{50} which is consistent with the similar levels of Reynolds stresses and TKE observed between these test cases. Furthermore, the presence of an upstream ice cover ($ICLC_{50}$) reduced the maximum production by15% compared to the case of the cylinder without upstream ice cover (LC_{50}).

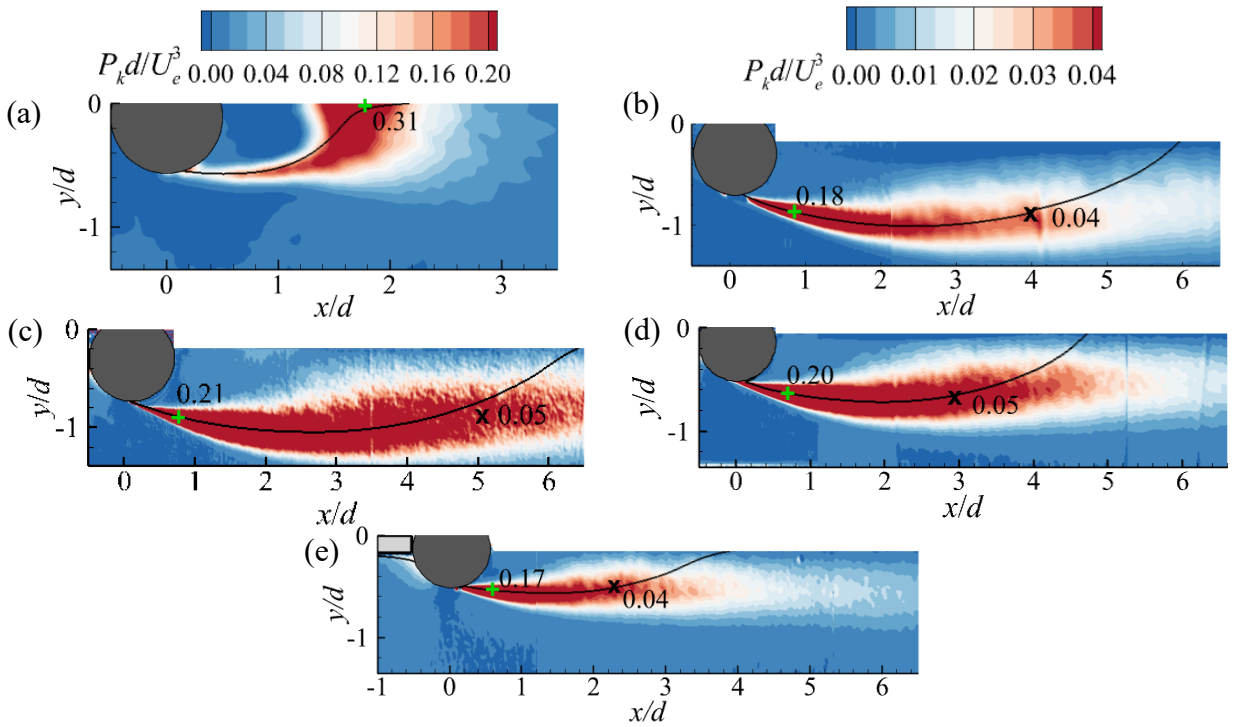

Figure 4.1.8. Contours of dimensionless P_k in the transport equation of TKE for UC (a), SC_{75} (b), LC_{75} (c), LC_{50} (d), and $ICLC_{50}$ (e). The magnitudes of the maximum P_k and its location (green "+" symbol) as well as the magnitude of P_k at location of maximum TKE (black "x" symbol) are indicated. The left contour legend to is used for UC whiles the right contour legend is used for the partially submerged caes.

To further investigate the mechanisms of turbulence production around the cylinders, vertical profiles of dimensionless P_k and the individual terms of equation (4.5) at the locations of maximum TKE are shown in Figure 4.1.9(a, c, e, g, i). In all cases, the contribution from streamwise fluctuating velocities, $-\overline{u'u'}\frac{\partial U}{\partial x}$, is negative (i.e., energy sink) in the region adjacent to the wake centerline (UC) or free surface (partially submerged cases) but acts as an energy source as the freestream is approached. By virtue of spanwise homogeneity and mass conservation, $\frac{\partial V}{\partial y} = -\frac{\partial U}{\partial x}$; thus, the sign and contribution from the vertical fluctuating velocities ($-\overline{v'v'}\frac{\partial V}{\partial y}$) are opposite to$-\overline{u'u'}\frac{\partial U}{\partial x}$. Regarding the contribution from the Reynolds shear stress, $-\overline{u'v'}\frac{\partial U}{\partial y}$ acts as an energy

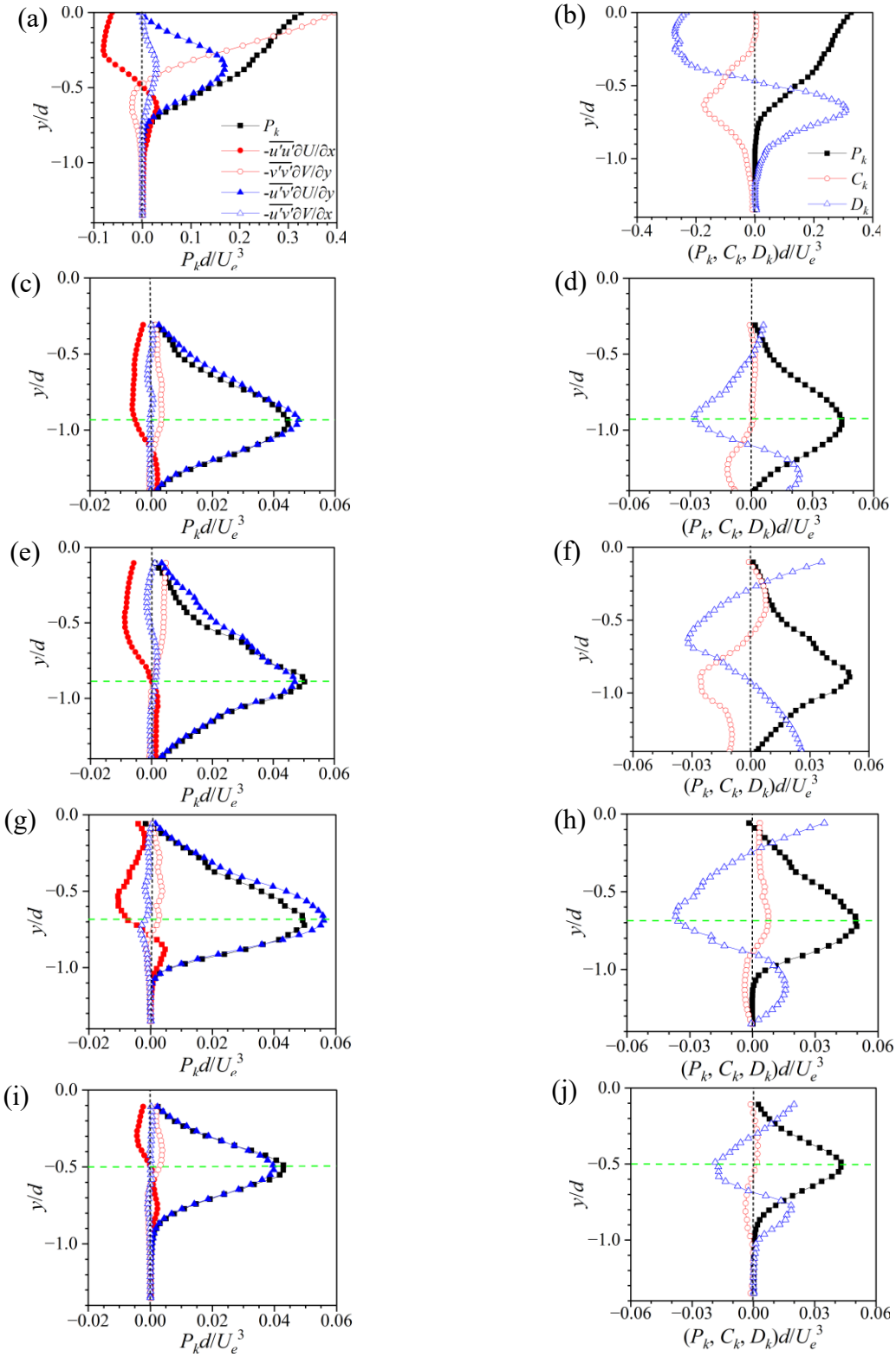

Figure 4.1.9. Vertical profiles of the individual production terms (left), and the energy budget terms of TKE at the location of the maximum TKE for UC (a, b), SC_{75} (c, d), LC_{75} (e, f), LC_{50} (g, h), and $ICLC_{50}$ (i, j). The green dashed horizontal line marks the vertical location of the separating streamline.

source while $-\overline{u'v'}\frac{\partial V}{\partial x}$ is either positive (UC), negative (LC_{50}), or shows a sign change (SC_{75}, LC_{75}, and $ICLC_{50}$). Nonetheless, the contribution from $-\overline{u'v'}\frac{\partial U}{\partial y}$ always outweighs that of $-\overline{u'v'}\frac{\partial V}{\partial x}$ because of the stronger $\frac{\partial U}{\partial y}$ compared to $\frac{\partial V}{\partial x}$.

The distributions of $-\overline{u'u'}\frac{\partial U}{\partial x}$ and $-\overline{u'v'}\frac{\partial U}{\partial y}$ are qualitatively similar among the different cases, and since $-\overline{u'v'}\frac{\partial V}{\partial x}$ is comparatively small, the net production is strongly dependent on $-\overline{v'v'}\frac{\partial V}{\partial y}$. Close to the wake centerline of the uniform flow case, for instance, $-\overline{u'v'}\frac{\partial U}{\partial y}$ is comparatively small and since $-\overline{u'u'}\frac{\partial U}{\partial x}$ is negative, $-\overline{v'v'}\frac{\partial V}{\partial y}$ is the primary energy source. The results also demonstrate that the net production of $\overline{v'v'}$ ($-\overline{v'v'}\frac{\partial V}{\partial y}-\overline{u'v'}\frac{\partial V}{\partial x}$) and $\overline{u'u'}$ ($-\overline{u'u'}\frac{\partial U}{\partial x}-\overline{u'v'}\frac{\partial U}{\partial y}$) are positive and negative, respectively, close to the wake centerline with the likelihood of inter-component energy transfer from $\overline{v'v'}$ to $\overline{u'u'}$ through the pressure-strain term. For the partially submerged cases, $-\overline{u'v'}\frac{\partial U}{\partial y}$ and the total production are nearly the same because the magnitudes of $-\overline{u'u'}\frac{\partial U}{\partial x}$ and $-\overline{v'v'}\frac{\partial V}{\partial y}$ are comparable. Close to the free surface of the partially submerged cases, it is $\overline{u'u'}$ that would transfer energy to $\overline{v'v'}$ since the net production is positive and negative in the former and latter, respectively.

Figure 4.1.9(b, d, f, h, j) show one-dimensional profiles of the production, convection and diffusion terms expressed in equations (4.5) to (4.7) at the locations of maximum TKE. The convection and diffusion terms are of the same sign (negative) close to the wake centerline and (positive) free surface. Otherwise, they are of opposite signs and counterbalance each other, regardless of submergence and upstream flow condition. However, the diffusion term is of higher magnitude which underscores the enhanced turbulent fluxes across the shear layer, and either reinforces

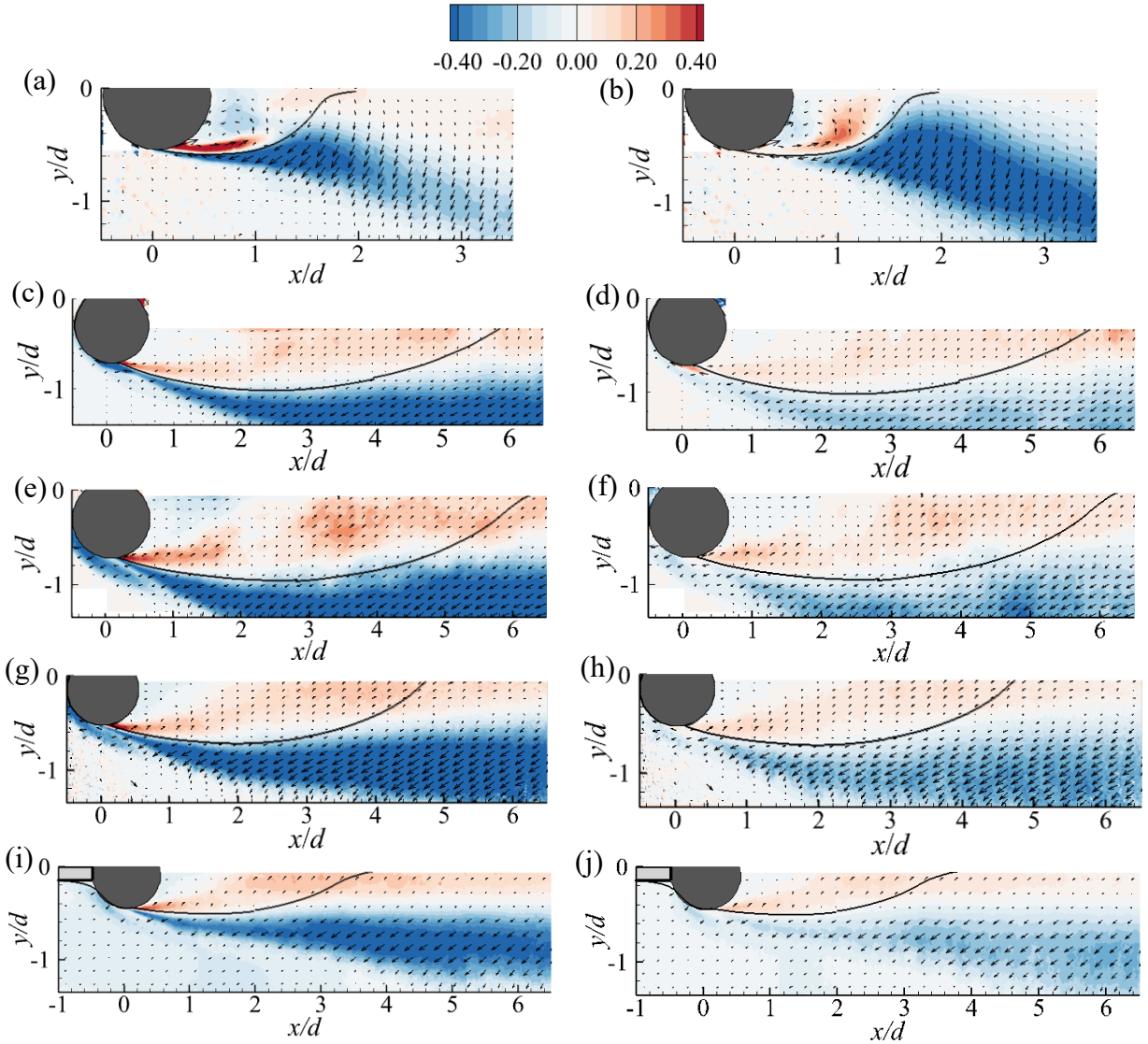

Figure 4.1.10. Contours of streamwise (u_k) and vertical (v_k) TKE transport velocities for UC (a, b), SC_{75} (c, d), LC_{75} (e, f), LC_{50} (g, h), and $ICLC_{50}$ (i, j). The black solid line is the mean separating streamline and the vectors of the TKE transport velocities are superimposed. The same levels are used for both u_k and v_k to facilitate comparisons. A white rectangle is used to mask spurious data at the air-water interface.

production as a source term (close to the free surface) or as an energy sink (close to the wake centerline or separating streamline). These results for the present partially submerged cases are in qualitative agreement with those of Addai et al. (2024) for partially submerged circular cylinders without upstream ice. Additionally, it is observed that turbulence convection by the mean flow and diffusion are an order of magnitude lower in the partially submerged cases compared to the uniform

flow case. For the partially submerged cylinders, the magnitudes of the budget terms are comparatively lower for SC_{75} than those of LC_{75} and LC_{50}, and the magnitude of the budget terms decrease further when the partially submerged cylinder is placed behind an ice cover.

Following Shabaka et al. (1985) and Hancock and Bradshaw (1987), the transport of TKE is examined using the streamwise (u_k) and vertical (v_k) transport velocities, which are defined as $u_k = (\overline{u'u'u'} + \overline{u'v'v'})/\text{TKE}$ and $v_k = (\overline{v'u'u'} + \overline{v'v'v'})/\text{TKE}$. Figure 4.1.10(a, c, e, g, i) and Figure 4.1.10(b, d, f, h, j), respectively, show contours of u_k and v_k superimposed with vectors of u_k and v_k. The distributions reveal turbulence diffusion from the shear layer towards the wake centerline (UC) and free surface (partially submerged cases) through fast entrainment ($+u_k$, $+v_k$), and into the freestream through slow ejection ($-u_k$, $-v_k$) events. Despite the qualitative similarities between turbulence diffusion in the UC and partially submerged cases, the streamwise transport is more intense compared to vertical transport of turbulence in the partially submerged cases, and vice versa in the case of UC. Also, while regions of elevated negative transport of turbulence (i.e., $-u_k$, $-v_k$) are nearly parallel to the free surface, they are inclined at an angle of 14° relative to the wake centerline in the case of UC.

4.1.5 Frequency spectra and temporal scales

In this section, the frequency spectra and temporal characteristics of the near wake are examined using velocity fluctuations extracted at the location of $\overline{u'u'}_{max}$. The time histories of u' and v' for UC, SC_{75}, and LC_{75} are shown in Figure 4.1.11(a, d, g), and those of LC_{50} and $ICLC_{50}$ in Figure 4.1.12(a, d). The fluctuating velocities for UC exhibit distinct periodicity, as expected for a circular cylinder in a uniform flow (Norberg and Sunden 1987; Dong et al. 2006; Khabbouchi et al. 2014). The frequency spectra of u' and v' in the uniform flow case (Figure 4.1.11(b)) show a distinct peak

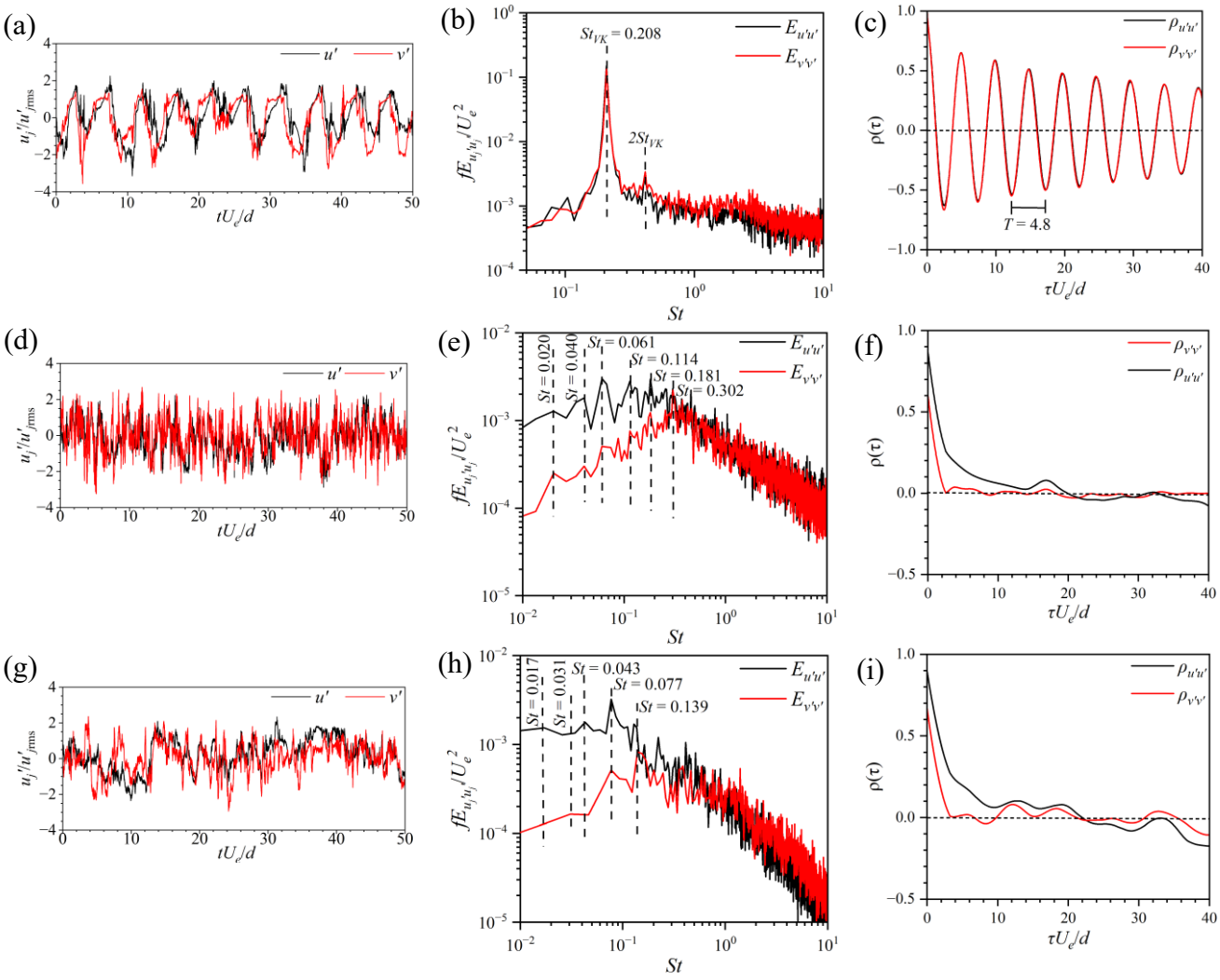

Figure 4.1.11. Time histories (left), frequency spectra (middle) and temporal autocorrelation coefficients (right) of velocity fluctuations extracted at the location of $\overline{u'u'}_{max}$ for UC (a, b, c), SC_{75} (d, e, f), and LC_{75} (g, h, i).

at a frequency that corresponds to the fundamental VK vortex shedding frequency of St_{VK} = 0.208 (Cantwell and Coles 1983; Dong et al. 2006; Khabbouchi et al. 2014). There also exists a distinct but weaker peak at the second harmonic of the VK shedding frequency ($2St_{VK}$). For the partially submerged cases, the fluctuating velocities exhibit irregular patterns, and their spectra (Figure 4.1.11(e, h) and Figure 4.1.12(b, e)) reveal peaks at multiple frequencies that are in the range of St = 0.017–0.302. This indicates that, unlike UC, the near wake regions of partially submerged

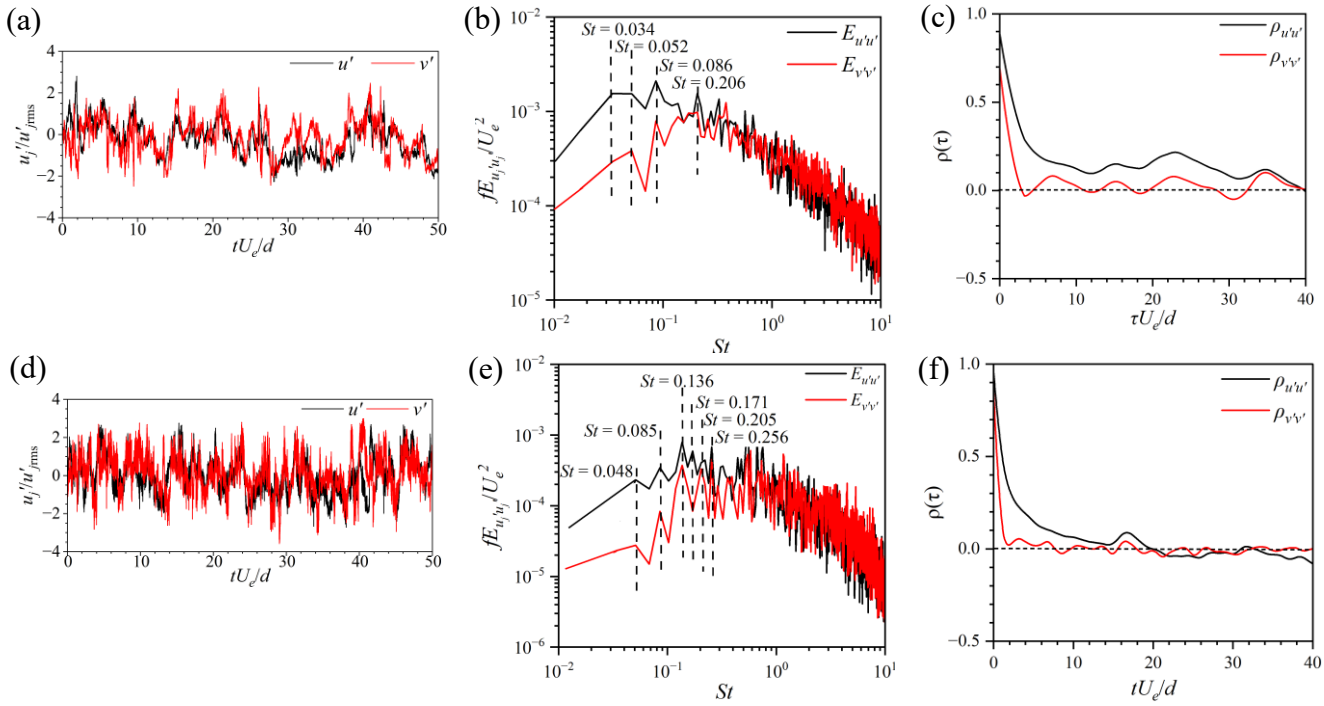

Figure 4.1.12. Time histories (left), frequency spectra (middle) and temporal autocorrelation coefficients (right) of velocity fluctuations extracted at the location of $\overline{u'u'}_{max}$ for LC_{50} (a, b, c) and $ICLC_{50}$ (d, e, f).

circular cylinders are characterized by a wide range of large-scale vortical structures, and these vortical structures are less energetic than those associated with the VK vortices, as evident in the weaker spectral peaks for the submerged cases compared to UC. The presence of multiple frequencies in the velocity spectra was also observed in He et al. (2017) for wall-mounted circular cylinders.

The temporal autocorrelation coefficient $\rho(\tau)$, which is a measure of the time over which a signal is correlated with itself, and temporal scales are also examined using the fluctuating velocities at the location of $\overline{u'u'}_{max}$. Following George (2013), $\rho(\tau)$ and temporal integral scale (T_{u_i}) are calculated as follows:

$$\rho_{u_i'u_i'}(\tau) = \frac{\overline{u_i'(t)u_i'(t+\tau)}}{\overline{u_i'u_i'}} \tag{4.8}$$

$$T_{u_i} = \int_0^{\tau^*} \rho_{u_i' u_i'}(\tau) d\tau \quad (4.9)$$

where $\tau = t' - t$ is the time difference, t and t' are the time origin and time shift, respectively, and τ^* is the value of τ at which $\rho(\tau)$ first crosses the temporal separation axis. Figure 4.1.11(c, f, i) and Figure 4.1.12(c, f) show the temporal autocorrelation coefficients of u' and v' denoted by $\rho_{u'u'}$ and $\rho_{v'v'}$, respectively. For the uniform flow case, the correlation coefficients show distinct sinusoidal patterns with a monotonic reduction in amplitude and a constant dimensionless period of T = 4.8 which coincides with the inverse of the VK shedding frequency, St = 0.208. In contrast, the correlation coefficients for the partially submerged cases show no distinct patterns nor periodicity. The correlation coefficients decay faster from the self-correlation time ($\tau = 0$) and reach zero sooner in the uniform flow case. For the partially submerged cases, the correlation coefficient based on the vertical fluctuating velocity ($\rho_{v'v'}$) decays faster in comparison to $\rho_{u'u'}$. The dimensionless temporal integral scale, based on u', is $T_u\, U_e/d$ = 0.67 for UC and ranges from 2.67 to 6.55 for the partially submerged cases. The larger temporal integral scales of the submerged cases, compared to the UC case, are consistent with characteristic low frequency motions observed in the near wake of the partially submerged circular cylinders.

4.1.6 Proper orthogonal decomposition

Proper orthogonal decomposition (POD) of the fluctuating velocity fields is performed in this section to explore the spatial and temporal dynamics of the energetic vortical structures in the wake of the cylinders. POD provides the optimal approximation of the total turbulence kinetic energy contained in a given number of modes and ranks the modes in order of decreasing energy content such that the first mode has the highest energy content (Riches et al. 2018; Khabbouchi et al. 2013; Fang and Tachie 2019b; Uruba and Procházka 2020).

The snapshot POD method proposed by Sirovich (1987) and outlined in Riches et al. (2018) and Fang and Tachie (2019b) is employed in this study. In this method, the fluctuating velocity vector field $u_i'(x,\ y,\ t)$ is decomposed into a combination of spatial eigenfunctions (or POD modes) ($\psi_i^k(x, y)$) multiplied by their respective time-dependent coefficients ($a^k(t)$) as follows:

$$u_i'(x,y,t) = \sum_{k=1}^{M} \psi_i^k(x,y)a^k(t) \tag{4.10}$$

where M is the number of POD modes. The POD analysis was performed over the flow field spanning $x/d \in$ [-0.5, 3.0] and $y/d \in$ [0.0, -1.4] for UC, and $x/d \in$ [-0.5, 5.0] and $y/d \in$ [0.0, -1.4] for the partially submerged cases, with the area identified as the cylinder masked out.

The energy captured in the first 5 POD modes are presented in Figure 4.1.13(a). For UC, the first and second POD modes contribute 23% and 21%, respectively, to the total TKE. This is consistent with previous studies that suggest the first two POD modes of a fully immersed circular cylinder have similar energy contents, reflecting the equal strength of the large-scale VK vortices shed alternately into the wake (Khabbouchi et al. 2013; Uruba and Procházka 2020). The energy contributions from modes 3 to 5 are significantly lower in comparison to the contributions from the first two modes. For the cases of the partially submerged cylinders in open water, the contribution from the first mode is significantly higher than the second mode. The energy content of the first POD mode increased by about 65% from SC_{75} to LC_{75} and 20% from LC_{75} to LC_{50}. This shows that increasing blockage ratio significantly increases the energy content of the largest vortical structures in the wake of a partially submerged cylinder compared to the effect of submergence level. In the presence of an upstream ice cover, the energy content of the first mode reduces by about 67% relative to that of the open water case (LC_{50}) and becomes comparable to that of the second mode. Nonetheless, the energy content of mode 1 in the partially submerged

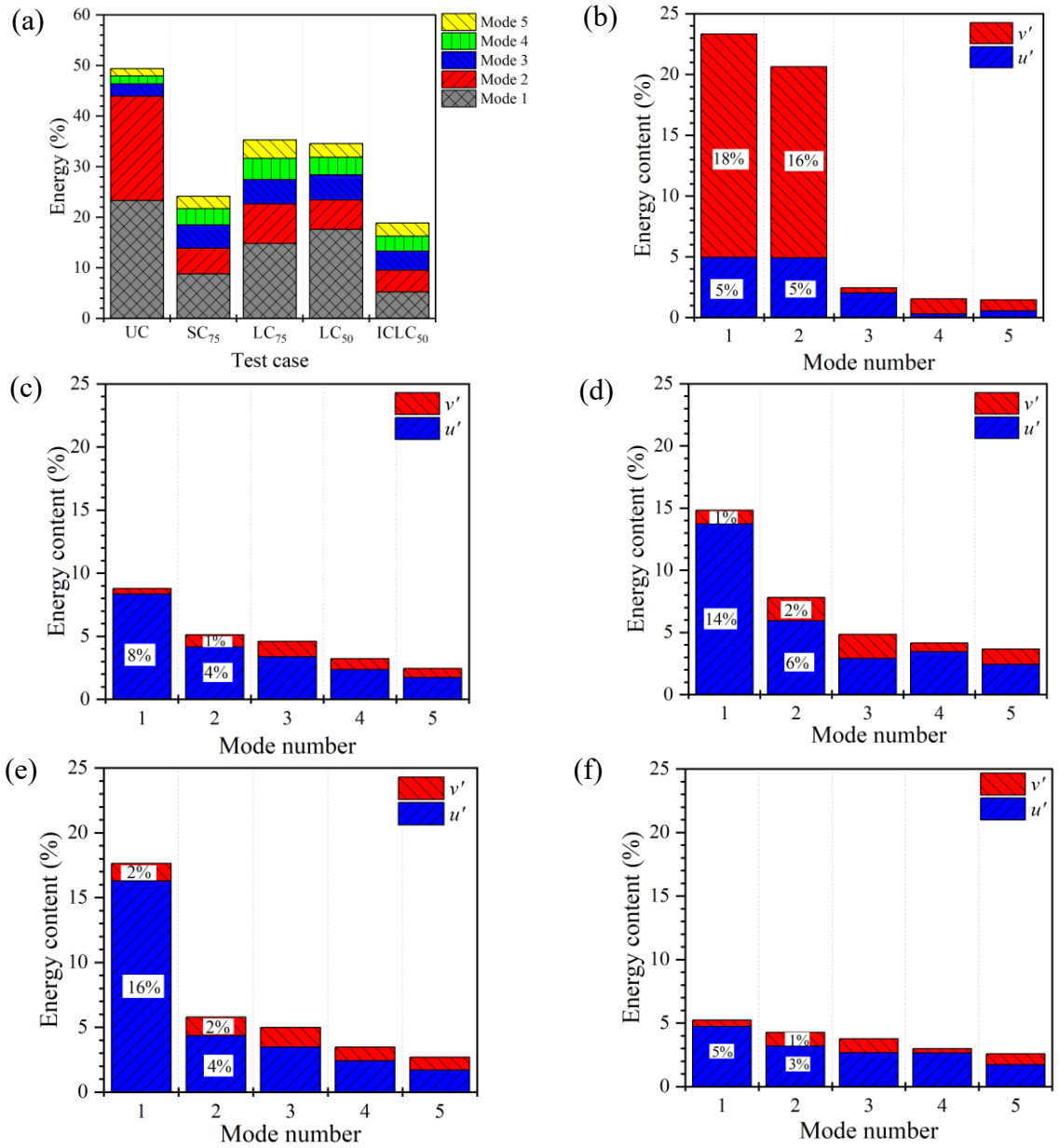

Figure 4.1.13. Energy percentages from the first five POD modes (a), and the relative contribution by the streamwise (u') and vertical (v') velocity fluctuations for UC (b), SC_{75} (c), LC_{75} (d), LC_{50} (e), and $ICLC_{50}$ (f).

cases are 22% to 74% lower compared to that of UC. However, the higher modes (modes 3 to 5) of the partially submerged cases are more energetic than their counterparts in the uniform case which may be attributed to the wide range of large-scale structures, as observed from the frequency spectra of fluctuating velocities.

The anisotropic nature of the velocity fluctuations, with $\overline{v'v'} > \overline{u'u'}$ in the uniform case and vice versa in the partially submerged cases, prompt examination of their relative contributions to the low-order modes. The relative energy contributions by u' and v' to the first five modes are shown in Figure 4.1.13(b) to (f). In the uniform flow case, besides mode 3 where the streamwise velocity fluctuations dominates, the vertical velocity fluctuations make the major contributions to the energy content of the other four modes. On the other hand, for the partially submerged cylinders, the streamwise velocity fluctuations dominate the first five modes, regardless of the upstream flow condition.

The topologies of the energetic vortical structures are examined in Figure 4.1.14 and Figure 4.1.15 using contours of the spatial modes of the vertical velocity fluctuations (ψ_v) of the first two POD modes. The contours are overlaid with fluctuating velocity vectors. The first two POD modes of UC show a train of alternating positive and negative vortical structures aligned along the wake centerline. The vortical structures are also shifted by one-quarter wavelength ($\lambda/4$) between the first two POD modes, where the wavelength (λ) is defined as the streamwise distance between peak locations of same-signed vortical structures. This behaviour is reminiscent of the alternate vortex shedding from cylinders in uniform flow (Khabbouchi et al. 2013; Riches et al. 2018; Uruba and Procházka 2020). On the other hand, the first POD modes for the partially submerged cylinders show the presence of a large vortical structure further downstream of the cylinders. Meanwhile, the second POD modes of all the partially submerged cases reveal a train of alternating positive and negative vortical structures that are aligned along the mean separating streamline. It is observed that the presence of an upstream ice cover decreases the organization and physical size of vortical structures around the partially submerged cylinder as evidenced by the relatively higher

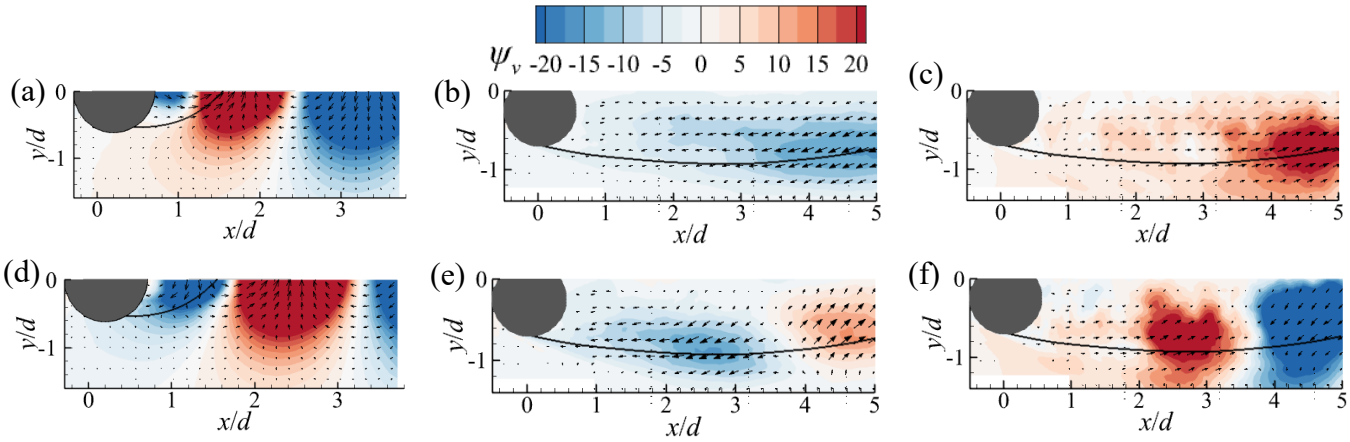

Figure 4.1.14. Contours of the first (top) and second (bottom) spatial modes of the vertical velocity fluctuations superimposed with the mean separating streamlines for UC (left), SC_{75} (middle), and LC_{75} (right).

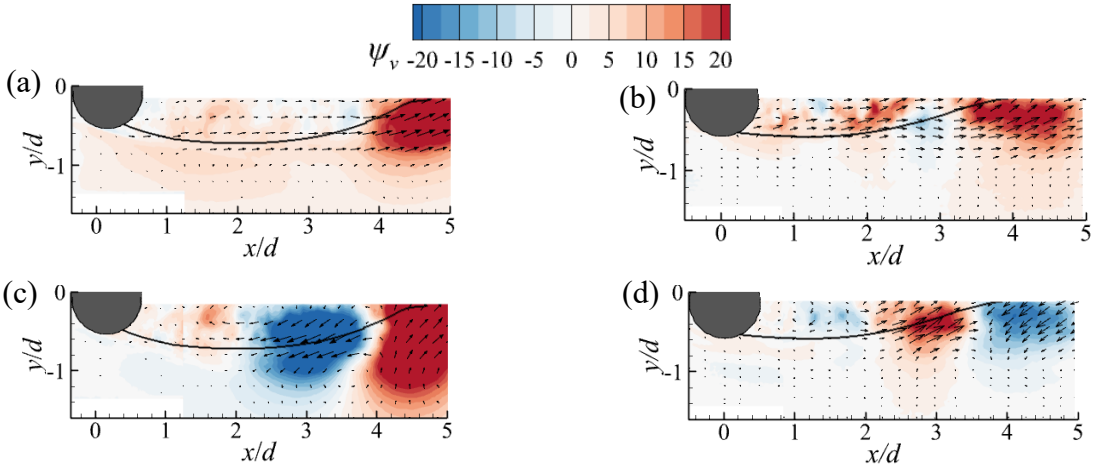

Figure 4.1.15. Contours of the first (top) and second (bottom) spatial modes of the vertical velocity fluctuations superimposed with the mean separating streamlines for LC_{50} (left), and $ICLC_{50}$ (right).

number of patches and smaller spatial extents of vortical structures in $ICLC_{50}$ compared to LC_{50}. For cylinders in uniform flow, the convective velocities of the vortical structures in the near wake region can be determined as follows (Riches et al. 2018; Kumahor and Tachie 2023b):

$$U_c/U_e = St_V \times \lambda/d \tag{4.11}$$

where St_V is the dominant Strouhal number of the wake. The half-wavelengths ($\lambda/2$) are

Table 4.1.3. Summary of half-wavelengths, St_V, and convective velocities.

Test case	$\lambda/2d$	St_V	U_c/U_e
UC	1.59	0.208	0.66
SC_{75}	2.00	0.061	0.24
LC_{75}	1.78	0.077	0.27
LC_{50}	1.61	0.086	0.28
$ICLC_{50}$	1.18	0.136	0.32

determined as the streamwise distance between peak locations of oppositely signed vortical structures, and St_V = 0.208, 0.061, 0.077, 0.086 and 0.136 for UC, SC_{75}, LC_{75}, LC_{50} and $ICLC_{50}$, respectively. Table 4.1.3 summarizes the values of the half-wavelength and convective velocity for the different test cases. The normalized convective velocity is 0.66 for UC and within 0.28 ± 0.04 for the partially submerged test cases. Lin and Hsieh (2003), who used the displacement of peak vorticity to estimate the convective velocity, reported U_c/U_e = 0.62 and 0.75 for Re = 2400 and 12 000, respectively, while Wang et al. (2020) reported U_c/U_e= 0.69 at Re = 16 000 using the centroid of vortical structures in the instantaneous vorticity distribution. These results are in good agreement with the present value for UC.

To investigate the temporal dynamics of the large-scale vortical structures, the time histories and phase portraits of the first two POD mode coefficients are presented in Figure 4.1.16. The time signals of the first two POD mode coefficients of UC display distinct sinusoidal wave patterns with no significant amplitude modulation with time, but a phase shift occurs between them. The phase portrait of these signals also exhibits a well-defined circular orbit with no significant cycle-to-cycle variation. This suggests that the first two POD modes of circular cylinders fully immersed in a uniform flow form a POD mode pair which represents the alternate VK vortex shedding

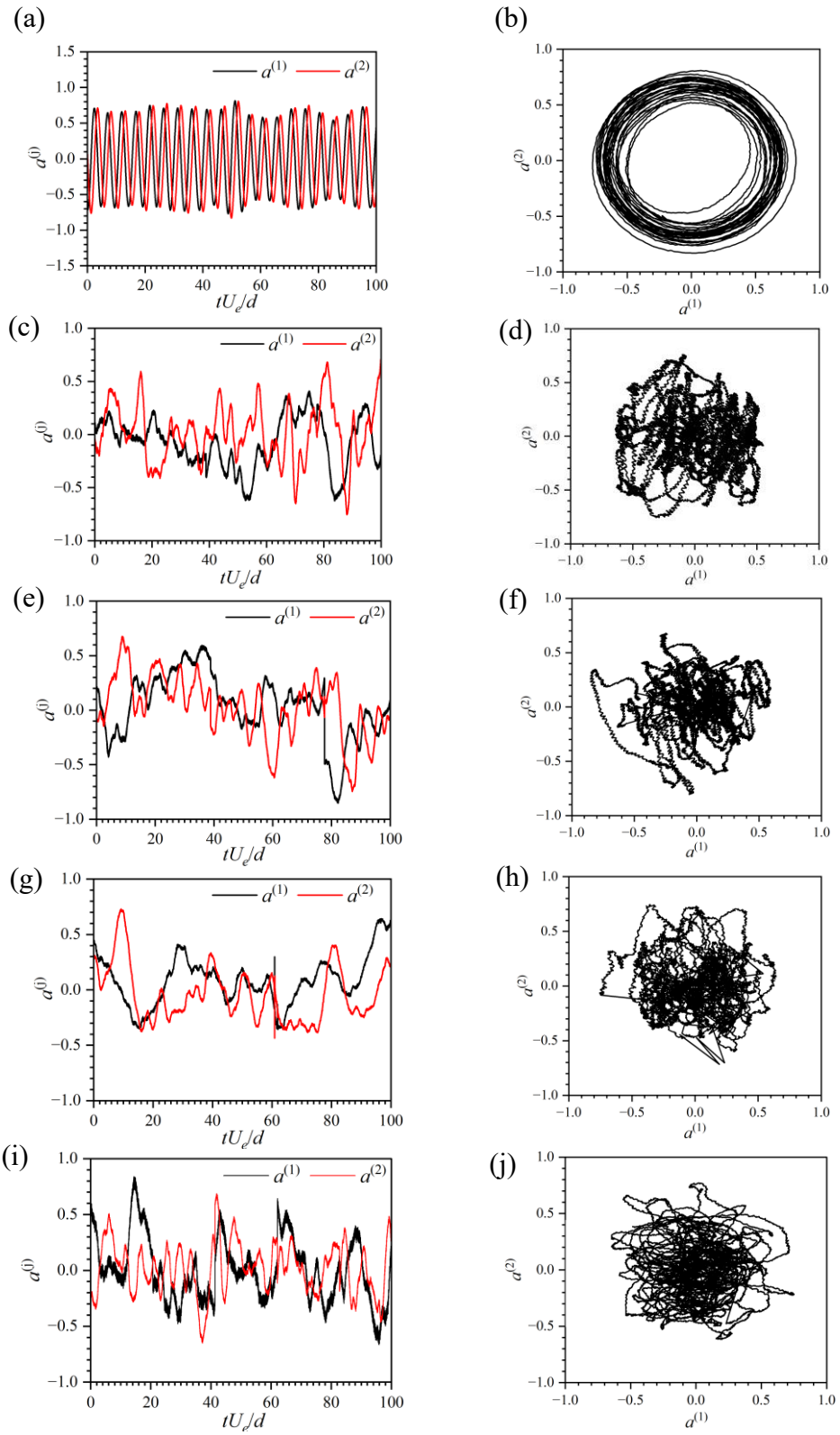

Figure 4.1.16. Time histories and phase portraits of the coefficients of the first two POD modes for UC (a, b), SC_{75} (c, d), LC_{75} (e, f), LC_{50} (g, h), and $ICLC_{50}$ (i, j).

motion (Riches et al. 2018). In contrast, the time histories of the first two POD mode coefficients of the partially submerged cases show no discernible patterns with significant amplitude modulation over time. The phase portraits of these signals also do not show the distinct circular orbit observed in UC. Indeed, no discernible correlation can be observed between the first two POD modes of these submerged cases. Khabbouchi et al. (2013) also observed lack of correlation between the first two POD modes of circular cylinders in the vicinity of a wall.

Figure 4.1.17 shows the frequency spectra of the coefficients of the first two POD modes. The frequency spectra of both mode coefficients for UC are similar and exhibit a dominant peak at St = 0.208 while those for the partially submerged cases reveal multiple low frequency peaks. For the cases of the partially submerged cylinders in open water, the dominant frequency for mode 1 is lower than the corresponding frequency for mode 2. However, for $ICLC_{50}$, the first two modes reveal a low dominant peak at St = 0.048, although the spectral density of this peak for mode 2 is lower compared to that of mode 1. The similarity in the Strouhal number obtained from the spectra of the POD mode coefficients and velocity fluctuations for UC (Figure 4.1.11(b)) is in conformity with previous studies that observed a dynamic link between the alternate vortex shedding motions and the first two POD modes in the wake of circular cylinders fully immersed in uniform flow (Perrin et al. 2007; Riches et al. 2018; Uruba and Procházka 2020). For the submerged cases, the low frequencies observed in the spectra of the first two POD mode coefficients are comparable with those from the spectra of the fluctuating velocities suggesting a connection between the first two POD modes and the low frequency motions in the wake of the partially submerged cylinders.

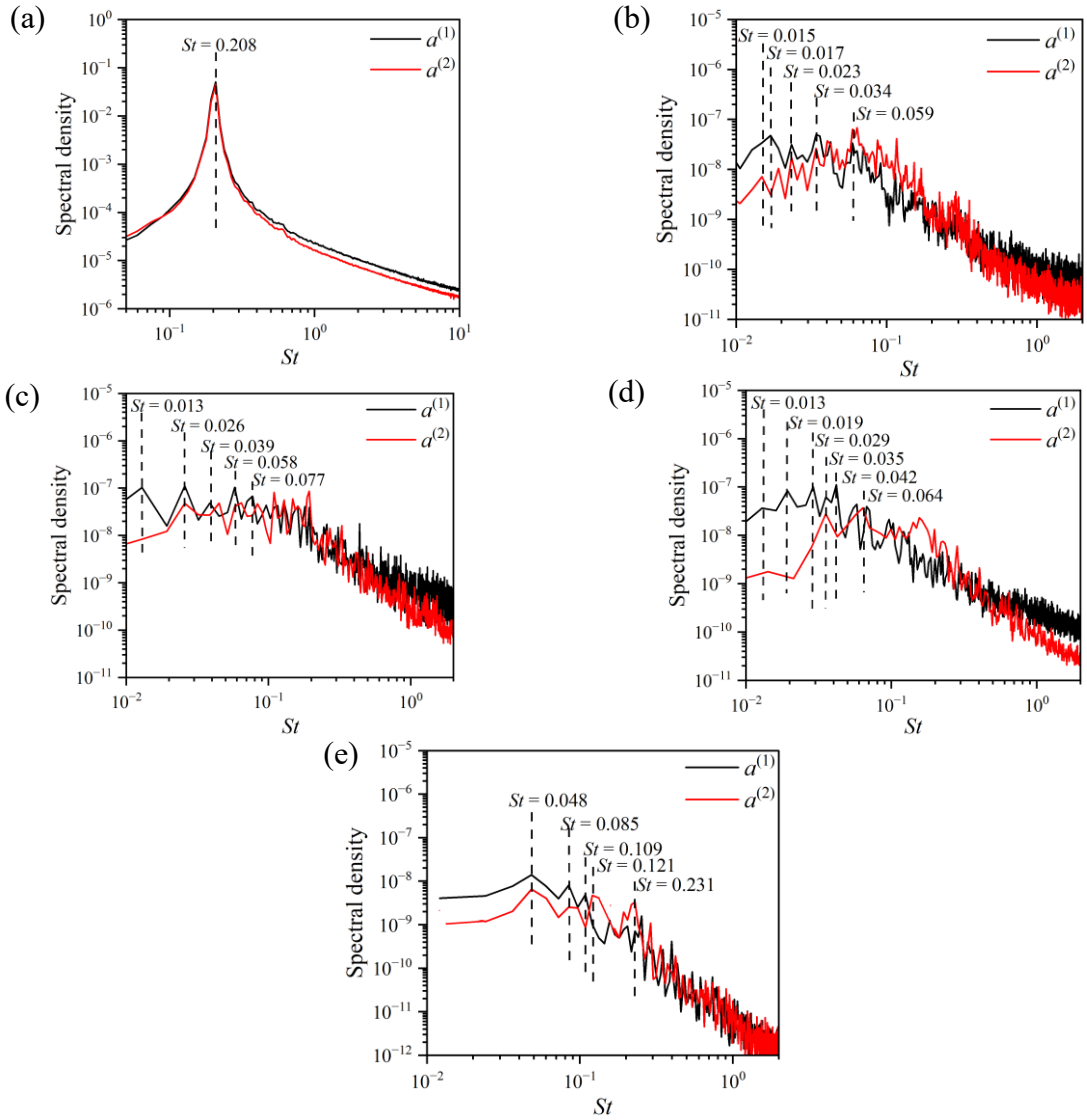

Figure 4.1.17. Frequency spectra of the coefficients of the first two POD modes for UC (a), SC_{75} (b), LC_{75} (c), LC_{50} (d), and $ICLC_{50}$ (e).

4.1.7 Unsteadiness of reverse flow area

Separated shear layers exhibit flapping motions which cause instantaneous expansion and contraction of the recirculation bubbles (Lyn and Rodi 1994; Pearson et al. 2013; Fang and Tachie 2019b; Essel et al. 2021). The flapping motions have been analyzed in the past using the temporal variation of the reverse flow area (Pearson et al. 2013; Graziani et al. 2018; Fang and Tachie 2019b; Essel et al. 2021) and the coefficients of the first POD mode (Thacker et al. 2013;

Mohammed-Taifour and Weiss 2016; Fang and Tachie 2019b). Fang and Tachie (2019b) demonstrated that both methods provide consistent results. Using the approach of Pearson et al. (2013), the flapping motions are examined through the instantaneous reverse flow area, $A_o(t)$ which is determined by summing up areas of $u < 0$ in the region of interest (E) as follows:

$$A_o(t) = \int_E \zeta\big(u(x,y,t)\big)\mathrm{dxdy}, \tag{4.12}$$

$$\zeta(p) = \begin{cases} 0, & p \geq 0 \\ 1, & p < 0 \end{cases}, \tag{4.13}$$

where dx and dy denote the vector spacings in the x and y directions, respectively, and $\zeta(p)$ is the detector function based on the event p.

The time variations and probability density functions (PDF) of the fluctuating reverse flow areas ($A' = A - \bar{A}$, where $\bar{A}$ is the time-averaged reverse flow area) normalized by the root-mean-square values, A_{rms}, are shown in Figure 4.1.18. The normalized time-averaged ($\bar{A}/d^2$) and root-mean-square (A_{rms}/d^2) values are indicated on the time history plots and the skewness values ($S_{A'}$) are indicated on the PDF plots. In each case, the time signals show a sequence of positive and negative fluctuations reminiscent of instantaneous expansion and contraction of the recirculation bubbles, respectively. In the case of UC, the time histories display quasi-periodic sinusoidal fluctuations. For the partially submerged cases, on the other hand, the time signals exhibit irregular patterns with less distinct and longer periodicity. This observation aligns with the larger temporal integral scales and lower frequencies observed in the wake of the partially submerged cylinders. The values of $\bar{A}/d^2$ and A_{rms}/d^2 for the submerged cases are an order of magnitude higher than the corresponding values for the UC case. However, the reverse flow areas of SC_{75} and LC_{75} are larger than that of LC_{50} as evidenced by the higher values of $\bar{A}/d^2$ and A_{rms}/d^2 of the former cases. The ice cover in $ICLC_{50}$ further decreases the size of the reverse flow area relative to that of LC_{50}. The

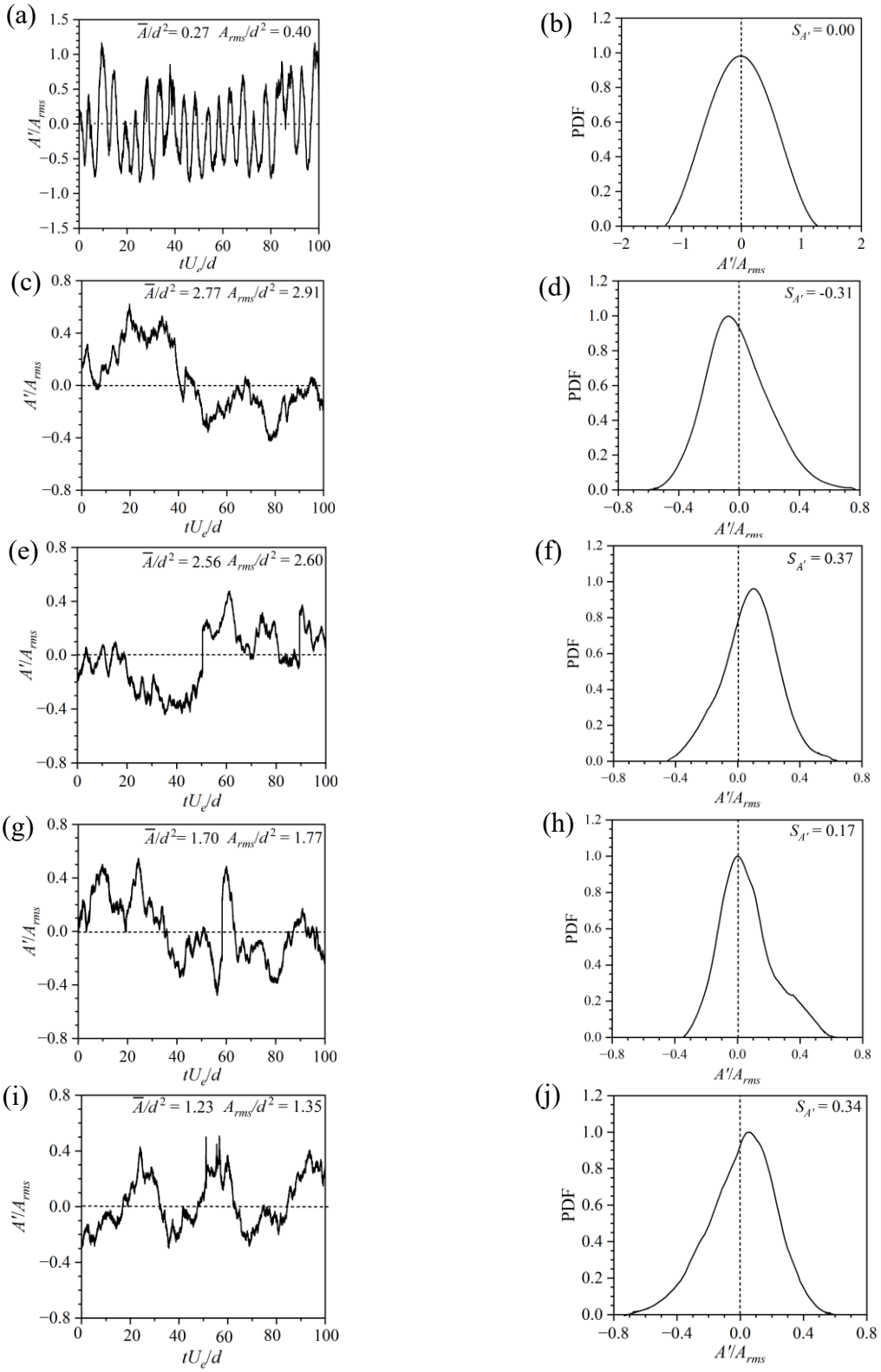

Figure 4.1.18. Time sequence of the fluctuating reverse flow area A' normalized by the root-mean-square value A_{rms} (left), and probability density functions (PDFs) of the reverse flow area A'/A_{rms} for UC (a, b), SC_{75} (c, d), LC_{75} (e, f), LC_{50} (g, h), and $ICLC_{50}$ (i, j). The PDF is normalized such that the maximum value is unity.

probability density functions (PDFs) of A'/A_{rms} exhibit unimodal distributions regardless of submergence level. The Gaussian PDF ($S_{A'} \approx 0$) of UC shows that there is an equal possibility for the occurrence of instantaneous expansions and contractions in the reverse flow area of a cylinder in the uniform flow. On the other hand, the skewed PDFs of the partially submerged cases, signify that their reverse flow areas undergo either more instantaneous expansions ($+S_{A'}$) or contractions ($-S_{A'}$), depending on the test condition. It is also observed that the flapping motions is comparatively more intense in the UC case than in the partially submerged cases, as evidenced by the extreme values of fluctuations in UC.

The frequency spectrum of the fluctuating reverse flow area for UC (Figure 4.1.19(a)) exhibits a single distinct peak at St = 0.208 which coincides with the VK vortex shedding frequency while those of the partially submerged cases (Figure 4.1.19(c, e, g, i)) reveal multiple but less distinct low frequency peaks. The dominant flapping frequencies for separated shear layers induced by adverse pressure gradient (Mohammed-Taifour and Weiss 2016), rectangular plate in uniform flow or partially submerged beneath a free surface (Kiya and Sasaki 1983; Fang et al. 2022), and forward-facing step (Largeau and Moriniere 2006), when defined in terms of the recirculation or reattachment length (i.e., $St_{L_r} = fL_r/U_e$), are within St_{L_r} = 0.08 to 0.2. In the present study, the values of St_{L_r} = 0.29, 0.20, 0.16, 0.15 and 0.10 for UC, SC_{75}, LC_{75}, LC_{50} and $ICLC_{50}$, respectively. The good agreement between the present values and those reported for separated flow induced by a wide range of geometries lend credence to the universality of St_{L_r}. Furthermore, the similarity of the frequencies captured in the spectra of the fluctuating reverse flow areas, POD modes and velocity fluctuations highlights an intimate dynamic link between the flapping motion of the separated shear layers and the vortex shedding motions.

Recently, Fang and Tachie (2019b) and Aleyasin et al. (2021) studied flows over forward-

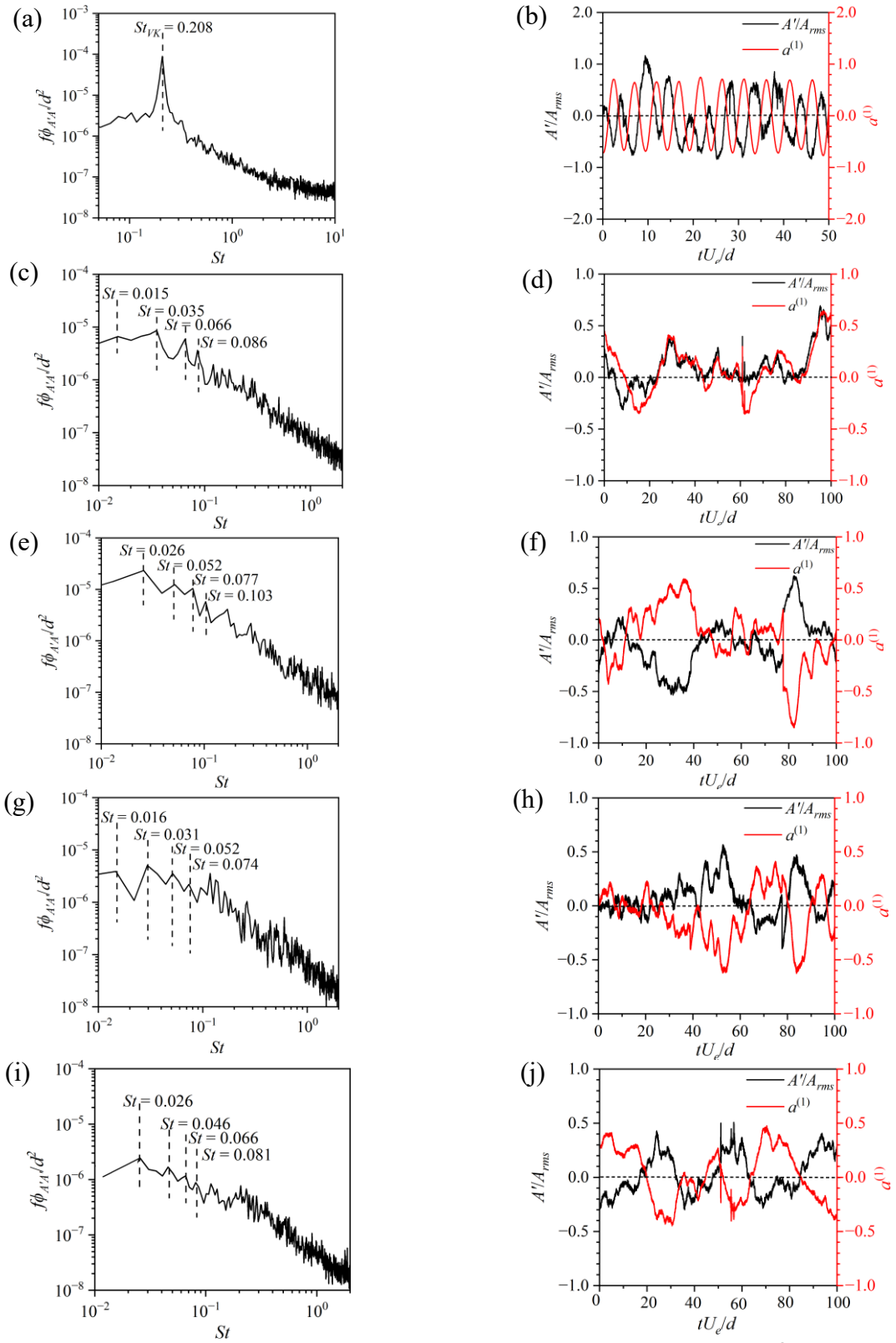

Figure 4.1.19. Frequency spectra of the fluctuating reverse flow area, $\phi_{A'A'}/d^2$ (left) and the time sequences of the first POD mode coefficient $a^{(1)}$ and A'/A_{rms} (right) for UC (a, b), SC_{75} (c, d), LC_{75} (e, f), LC_{50} (g, h), and $ICLC_{50}$ (i, j).

backward-facing steps and around three-dimensional Ahmed bodies, respectively, and showed that the time sequence of the first POD mode coefficient and the fluctuating reverse flow area synchronize well with each other. Based on their findings and the observation made in Figure 4.1.19(a, c, e, g, i), it is instructive to evaluate the correlation between the instantaneous reverse flow area and the most energetic structures. As shown in Figure 4.1.19(b, d, f, h, j), there exists a good synchronization between the time sequence of the fluctuating reverse flow areas and the first POD mode coefficient. A phase shift, however, occurs between the time sequence of the first POD mode coefficient and the fluctuating reverse flow area of UC, LC_{75}, LC_{50} and $ICLC_{50}$, but not in the case of SC_{75}. The degree of correlation between the fluctuating reverse flow areas and the first POD modes is quantified using the cross-correlation coefficient expressed as:

$$R_{A'a^{(1)}} = \frac{\overline{A' \times a^{(1)}}}{A'_{rms} \times a^{(1)}_{rms}} \tag{4.14}$$

The values of $R_{A'a^{(1)}}$ are -0.68, 0.81, -0.86, -0.91, and -0.87 for UC, SC_{75}, LC_{75}, LC_{50} and $ICLC_{50}$, respectively. It is noted that Kumahor and Tachie (2023b) reported $R_{A'a^{(1)}}$ = -0.52 for a short rectangular cylinder in uniform flow while Aleyasin et al. (2021) reported $R_{A'a^{(1)}}$ = 0.83 for wall-mounted Ahmed bodies. The higher cross-correlation coefficients observed in the partially submerged test cases highlight a stronger influence of the most energetic modes in modulating the reverse flow area in these cases, compared to the uniform flow case.

4.2 Effects of Different Upstream Ice Block Conditions

The effects of different conditions of upstream ice block on the mean flow and turbulence transport phenomena around a partially submerged circular cylinder are discussed in this section using the test cases from the second set of experiments (SIP, SIC, RIC, and TRIC). The results presented

here were submitted to the Journal of Hydraulic Research on 12th June 2024 in the paper: Israel, M. K., Dow, K., Clark, S. P., and Tachie, M. F. (2024), "PIV investigation of the effects of simulated ice blocks on the turbulent flow dynamics around a partially submerged horizontal circular cylinder".

4.2.1 Approach boundary layer

The vertical profiles of streamwise mean velocity and Reynolds stresses at a streamwise location $0.2d$ upstream of the trailing edge of the simulated ice block are used to examine the characteristics of the approach boundary layer underneath the ice block. These profiles are shown in Figure 4.2.1, and the pertinent boundary layer parameters, including the boundary layer thickness, displacement thickness (δ^*), momentum thickness (θ), shape factor ($H = \delta^*/\theta$), and the momentum thickness Reynolds number ($Re_\theta = U_e\theta/\nu$) are summarized in Table 4.2.1. The values of streamwise mean velocities ($U|_S$) and turbulence intensities ($Tu|_S$) at the submergence level of the cylinder are also included in Table 4.2.1.

For the smooth undersurface cases, the boundary layer beneath the ice cover (SIC) is more developed than beneath the ice pan (SIP) as evident in the comparatively lower values of streamwise mean velocities and higher levels of Reynolds stresses for SIC compared to SIP. At the elevation corresponding to the submergence level ($y = 0.5d$), the streamwise mean velocities are $0.94U_e$ and $0.86U_e$ for SIP and SIC, respectively, and the corresponding turbulence intensities are 3.2% and 5.8%. These results indicate that an ice boom will be exposed to an approach flow with lower momentum but higher turbulence intensity when situated downstream of an ice cover rather than an ice pan. The higher flow resistance due to the undersurface roughness reduces the mean velocities adjacent to the ice cover but significantly increases the levels of Reynolds stresses as

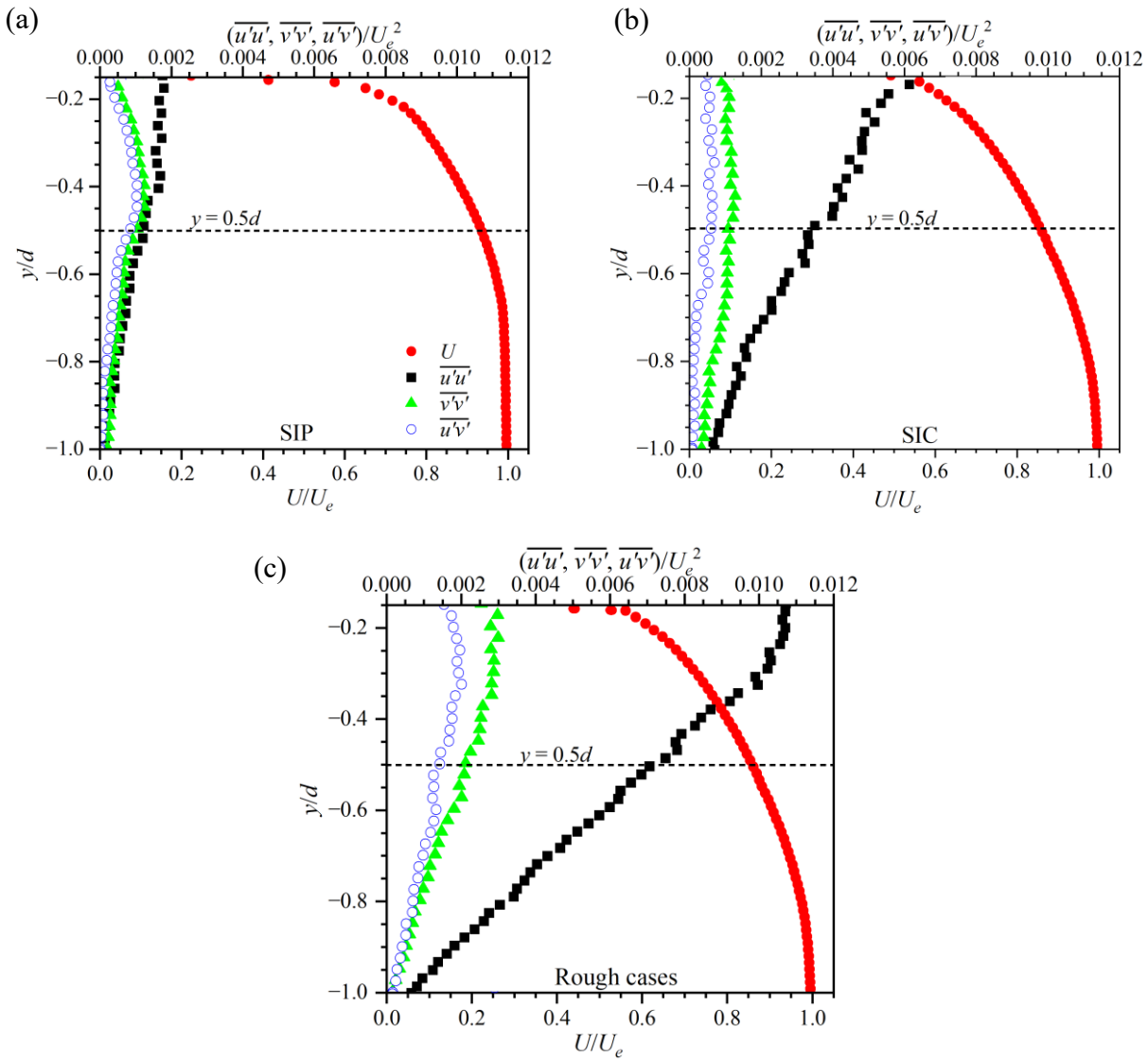

Figure 4.2.1. Vertical profiles of dimensionless streamwise mean velocity and Reynolds stresses of the approach boundary layer for (a) SIP, (b) SIC and (c) the two rough undersurface cases.

Table 4.2.1. Summary of the approach boundary layer parameters for the different test cases.

Test case	Re	δ (mm)	δ/d	$U\|_S/U_e$	$Tu\|_S$	δ^* (mm)	θ (mm)	H	Re_θ
SIP	25 500	39.4	0.51	0.94	0.032	6.2	4.6	1.35	1520
SIC	25 500	56.4	0.73	0.86	0.058	7.9	6.1	1.30	2010
RIC	25 500	59.5	0.77	0.83	0.084	11.3	7.0	1.61	2310
TRIC	25 500	59.5	0.77	0.83	0.084	11.3	7.0	1.61	2310

well as the boundary layer thickness in comparison to the smooth undersurface ice cover. It is noted that the boundary layer shape factor for the smooth and rough ice covers are comparable to $H = 1.33$ and $H = 1.58$ for smooth and rough wall turbulent boundary layers, respectively, at $Re_\theta = 2100$ (Essel et al. 2015).

4.2.2 Mean flow

Figure 4.2.2 presents contours of dimensionless streamwise and vertical mean velocities overlaid with mean streamlines to examine the effects of upstream ice block condition on the mean flow features around the cylinder. In the cases with ice block submerged thickness smaller than the submergence level of the cylinder (i.e., SIP, SIC and RIC), the mean flow deflects downwards as it approaches the cylinder, accelerates around the cylinder resulting in a region of elevated U/U_e beneath the cylinder, and subsequently recovers upwards and attaches to the free surface downstream of the cylinder. For the two smooth ice cases, the mean separation point in SIC is shifted behind and away relative to that in SIP, and the recirculation region as well as the magnitudes of U/U_e and V/U_e are substantially smaller in SIC than in SIP. With the introduction of undersurface roughness (RIC), the mean separation point shifts further behind the cylinder, and the recirculation bubble and magnitudes of mean velocities are significantly reduced in comparison to the smooth ice block cases. These observations are attributed to the differences in the characteristics of the approach flow. Specifically, the intensity and persistence of mean flow deflection, acceleration and entrainment of the external flow into the wake flow behind the cylinder decreases with decreasing approach flow momentum. When the ice block is thicker than the submerged cylinder (TRIC), the mean flow separates directly from the trailing edge of the ice block and the separated flow glides over the cylinder before attaching to the free surface. The

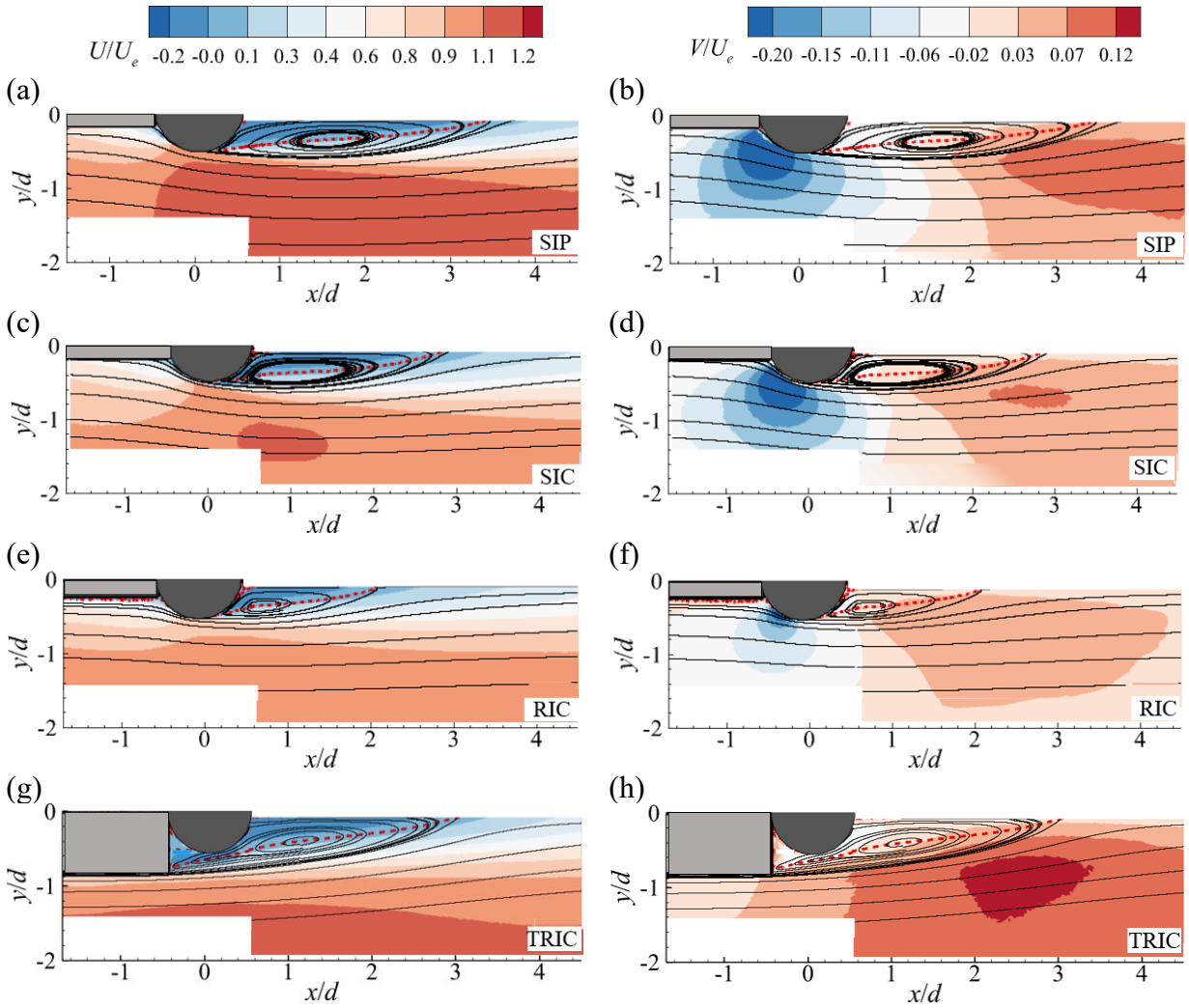

Figure 4.2.2. Contours of dimensionless streamwise (U/U_e) (a, c, e, g) and vertical (V/U_e) (b, d, f, h) mean velocities superimposed with mean streamlines. The superimposed red dashed line on the contour plots is the isopleth of $U = 0$. A white rectangle is used to mask spurious data at the air-water interface.

increased submerged thickness of the ice block in this case reduces the mean flow section beneath the ice block and cylinder which enhances the levels of U/U_e and V/U_e around the cylinder. These results align with the findings of Essel et al. (2015) and Nematollahi and Tachie (2018) who reported a more rapid mean flow acceleration over forward-facing steps with upstream smooth walls compared to those with upstream rough walls. It is worth noting that the smaller SV observed in the wake of the partially submerged cylinders in Section 4.1.2.2 are absent in the present test

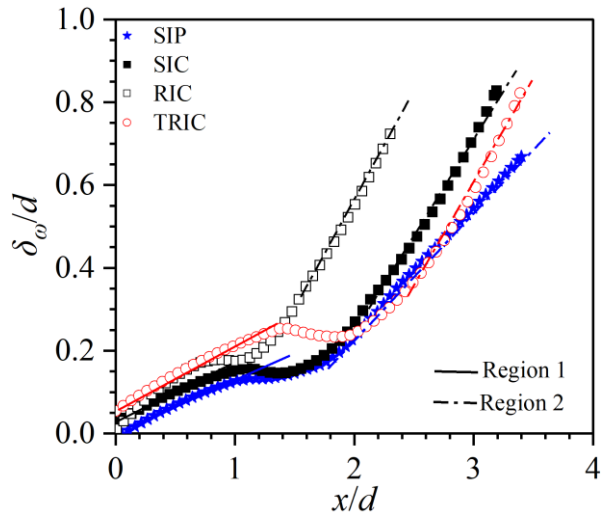

Figure 4.2.3. Streamwise variation of vorticity thickness δ_ω/d.

cases. Addai et al. (2024) who examined the effects of Reynolds number on the separated flow characteristics around partially submerged circular cylinders without upstream ice reported that the formation of the SV is inhibited at $Re > 17\,000$. Thus, the absence of the SV in the present test cases is likely due to the substantially high Re at which the present experiments were conducted.

The mean recirculation length and vorticity thickness are, respectively, used to quantify the effect of upstream ice block condition on the size of the mean recirculation bubble and the growth rate of the separated shear layer around the cylinder. Figure 4.2.3 shows the streamwise variation of vorticity thickness. The profiles in Figure 4.2.3 exhibit the two linear regions (Regions 1 and 2) with different growth rates, and the near-flattening of vorticity thickness in the mid-region of separated shear layers, observed in Figure 4.1.5(a). Table 4.2.2 presents a summary of maximum backflow velocities (U_b/U_e), mean recirculation lengths (L_r/d), and the growth rates ($\mathrm{d}\delta_\omega/\mathrm{d}x$) of the two linear regions of the separated shear layer. The maximum backflow velocity and the mean recirculation length in SIC are 12% and 17% smaller, respectively, than the corresponding values in SIP, and upstream undersurface roughness reduces U_b/U_e and L_r/d in RIC by 28% and 31%,

Table 4.2.2. Summary of critical parameters of the mean flow and shear layer growth rates.

Test case	U_b/U_e	L_r/d	$d\delta_\omega/dx$	
			Region 1	Region 2
SIP	-0.26	3.5	0.13	0.32
SIC	-0.23	2.9	0.13	0.44
RIC	-0.17	2.0	0.20	0.51
TRIC	-0.19	3.1	0.17	0.49

respectively, relative to SIC. However, U_b/U_e and L_r/d increase by 12% and 55%, respectively, in TRIC compared to RIC, when the submerged thickness of the ice block is larger than the submergence level of the cylinder. It is noted that Addai et al. (2024) reported U_b/U_e = -0.35 and L_r/d = 4.2 for a partially submerged cylinder with no upstream ice block at a similar Reynolds number as the present study. The growth rates for Region 1 of the separated shear layers are within 0.16 ± 0.04 for the present test cases, which are in good agreement with the values of 0.13 and 0.17 evaluated for the case of the cylinder fully immersed in uniform flow and the partially submerged cylinders, respectively, and the values reported by the previous studies on different bluff body geometries from Section 4.1.2.3. For Region 2, the growth rates of the shear layers in SIC, RIC and TRIC are 37%, 59% and 52% higher, respectively, than that of SIP. These observations show a strong influence of the approach boundary layer turbulence on the growth of the shear layer and the mean recirculation length around the cylinder. Specifically, higher turbulence intensities in the boundary layer underneath the ice block promotes growth of the separated shear layer and reduces the mean recirculation length. This observation is in good agreement with the results of Essel et al. (2015), who investigated the effects of upstream wall roughness on the separated flow around a forward-facing step and observed that roughness increases the momentum deficit and turbulence level in the approach boundary layer, and this

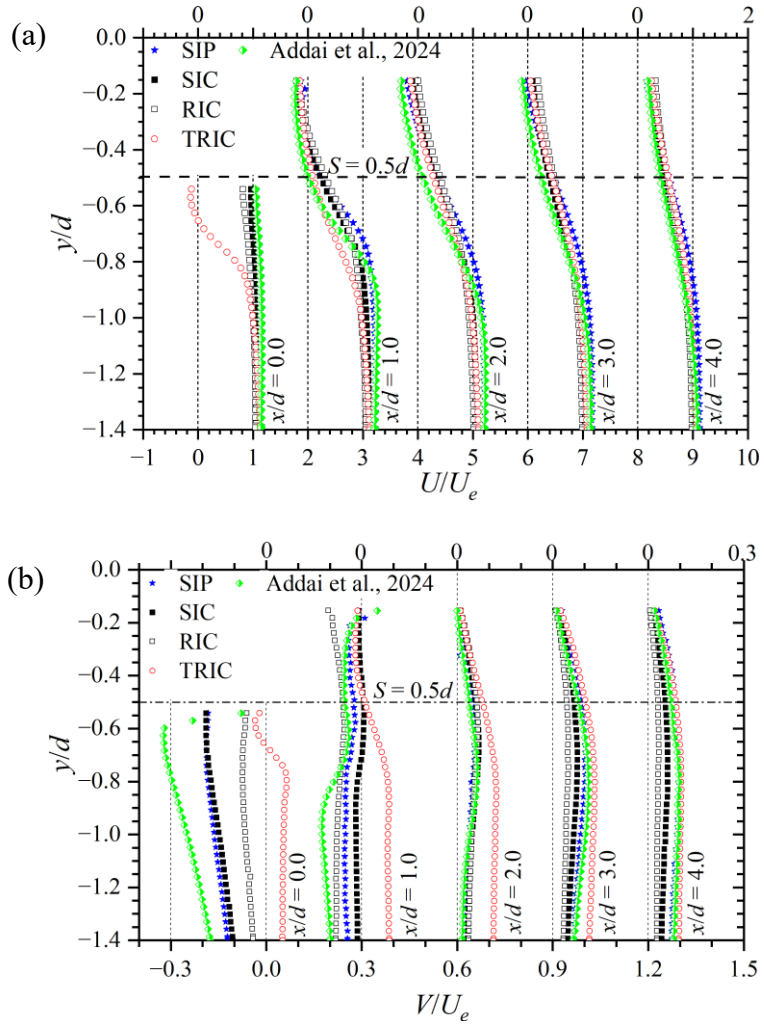

Figure 4.2.4. Vertical profiles of dimensionless (a) streamwise and (b) vertical mean velocities. The profiles at consecutive locations are shifted to the right of the preceding location for clarity. Data from Addai et al. (2024) for a partially submerged circular cylinder with no upstream ice block is included for comparison.

caused the recirculation length over the step to reduce by 44% compared to the case of the step with an upstream smooth wall.

Vertical profiles of streamwise and vertical mean velocities at five streamwise locations: $x/d = 0.0$, 1.0, 2.0, 3.0 and 4.0 are shown in Figure 4.2.4 to assess the effects of upstream ice blocks on the evolution of the mean flow around the cylinder. Data from Addai et al. (2024) for a partially submerged cylinder with no upstream ice block at a similar *Re* as the present study is included for

comparison. The mean flow is distorted near the cylinder and gradually recovers downstream of the cylinder, regardless of upstream flow condition. The mean velocities around the cylinder are lower and the mean flow recovers faster in SIC compared to the case of SIP. Upstream undersurface roughness (RIC) also reduces the mean velocities, and the mean flow recovery occurs earlier than in the smooth cases. The thickened rough undersurface ice cover in TRIC causes significant disruption to the mean flow and enhances the mean velocities around the cylinder compared to the other cases. Generally, except for TRIC, the mean velocities around the cylinder with upstream ice blocks (SIP, SIC and RIC) are lower compared to the case where there is no upstream ice block (Addai et al. 2024).

4.2.3 Reynolds stresses and turbulence kinetic energy

The effects of upstream ice block conditions on the fluctuating velocity field are examined using the Reynolds stresses and turbulence kinetic energy. Figure 4.2.5 presents the contour plots of dimensionless streamwise and vertical Reynolds normal stresses. Both the streamwise and vertical Reynolds normal stresses are concentrated along the separated shear layer but the streamwise component is significantly larger compared to the vertical component, which underscore the anisotropy of turbulence in the wake flow around the partially submerged cylinder. These observations are consistent with those of the partially submerged cylinders from Section 4.1.3, and previous studies on partially submerged circular cylinders with no upstream ice block (Ozdil and Akilli 2015; Edie et al. 2021; Addai et al. 2024), and partially buried and wall-mounted circular cylinders (Wang and Tan 2008; Akoz 2012; He et al. 2017).

The peak magnitude of the streamwise Reynolds normal stress in SIP is 0.076 but this value decreased by 11% as the length of the ice block increases (SIC) and 40% when the undersurface

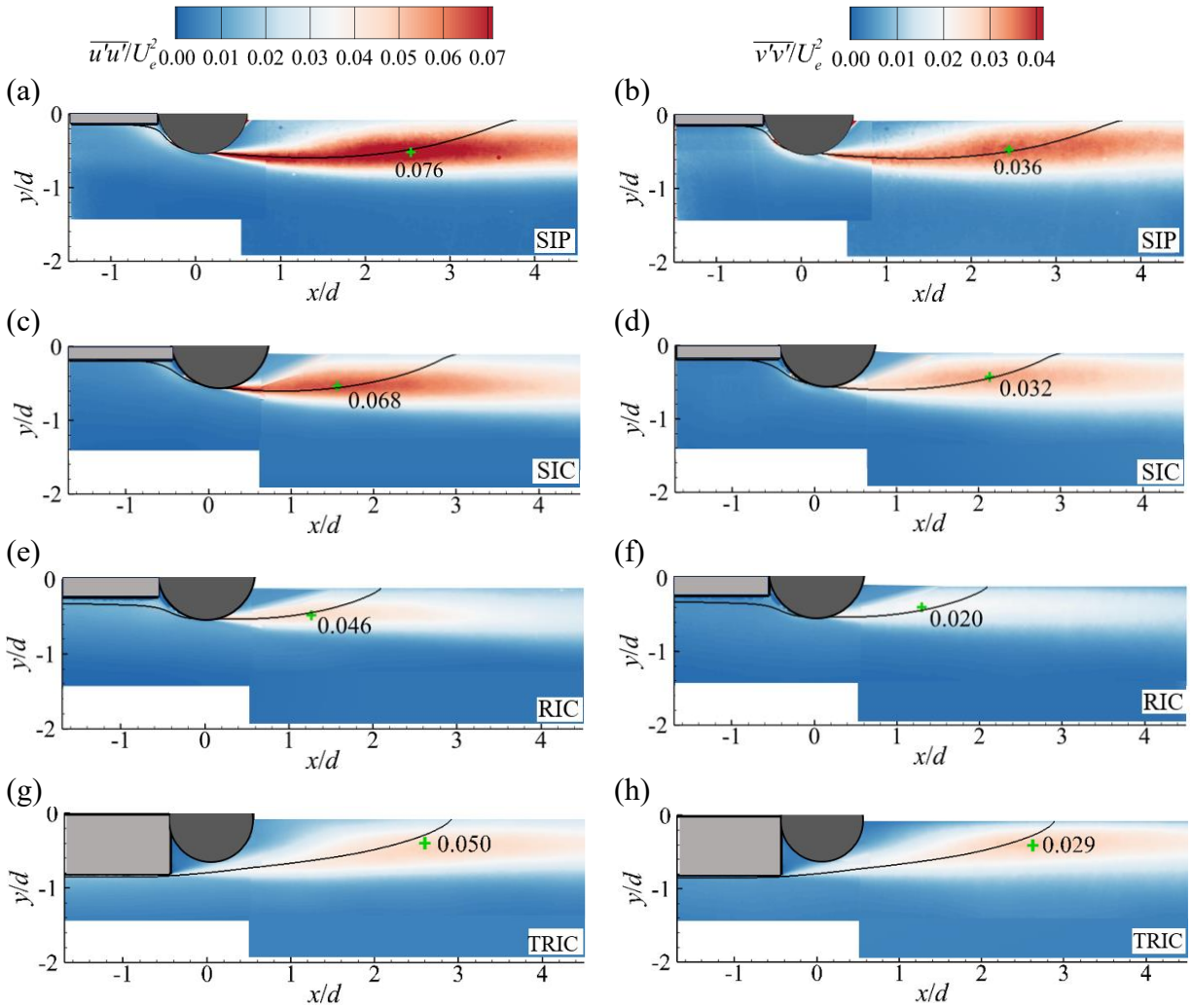

Figure 4.2.5. Contours of dimensionless streamwise (left) and vertical (right) Reynolds normal stresses. The solid black line is the mean separating streamline. The locations (green '+' symbol) and magnitudes of peak values are also indicated. A white rectangle is used to mask spurious data at the air-water interface.

becomes rough (RIC). The corresponding reduction in the peak magnitude of the vertical Reynolds normal stress in SIC and RIC are 11% and 44%, respectively, compared to SIP. The levels of Reynolds normal stresses, including their peak values, are 44% to 70% lower than the values reported by Addai et al. (2024) for a partially submerged circular cylinder with no upstream ice block. Essel et al. (2015) who investigated the effects of upstream wall roughness on the separated flow over a forward-facing step observed a similar reduction in the turbulence levels in the shear

layer in the case of an upstream rough wall relative to that in the smooth wall case. It is observed that the peaks of the Reynolds normal stresses are located nearer to the cylinder in the cases of the longer ice blocks (SIC and RIC) compared to SIP. The peak location of the Reynolds stresses is often related to transition from laminar to turbulence along the separated shear layer (Brun et al. 2008; Lander et al. 2016; Moore et al. 2019). Since the turbulence levels in the approach boundary layer over the longer smooth and rough ice blocks (SIC and RIC) are comparatively higher than in the case of SIP, it is expected that the transition process is more rapid for the longer ice blocks. The present results are also consistent with previous studies which demonstrated that higher turbulence intensity in the approach flow generally shortens the wake formation length around bluff bodies in uniform flow or mounted on a wall (Khabbouchi et al. 2014; Istvan and Yarusevych 2018). Higher turbulence in the approach flow would promote entrainment of higher momentum fluid from the external flow and lead to shortening of the recirculation region, as noted from Figure 4.2.2 and Table 4.2.2. For the two rough undercover cases, the peak values of streamwise and vertical Reynolds normal stresses are 8% and 45%, respectively, higher in the case of the thicker ice block (TRIC) than the corresponding values in RIC. These observed differences in the turbulence levels for the rough cases can be attributed to the characteristics of the separated shear layer which initiates from the cylinder in the case of RIC but from the trailing edge of the ice block for the thicker ice block. Additionally, the peaks in TRIC are located farther downstream and nearer to the free surface compared to RIC.

Figure 4.2.6 shows the contours of dimensionless Reynolds shear stress and turbulence kinetic energy. The distributions of the Reynolds shear stress and TKE around the partially submerged cylinder are qualitatively similar to those of the Reynolds normal stresses in that they are concentrated along the separated shear layer. The Reynolds shear stresses are positive with peaks

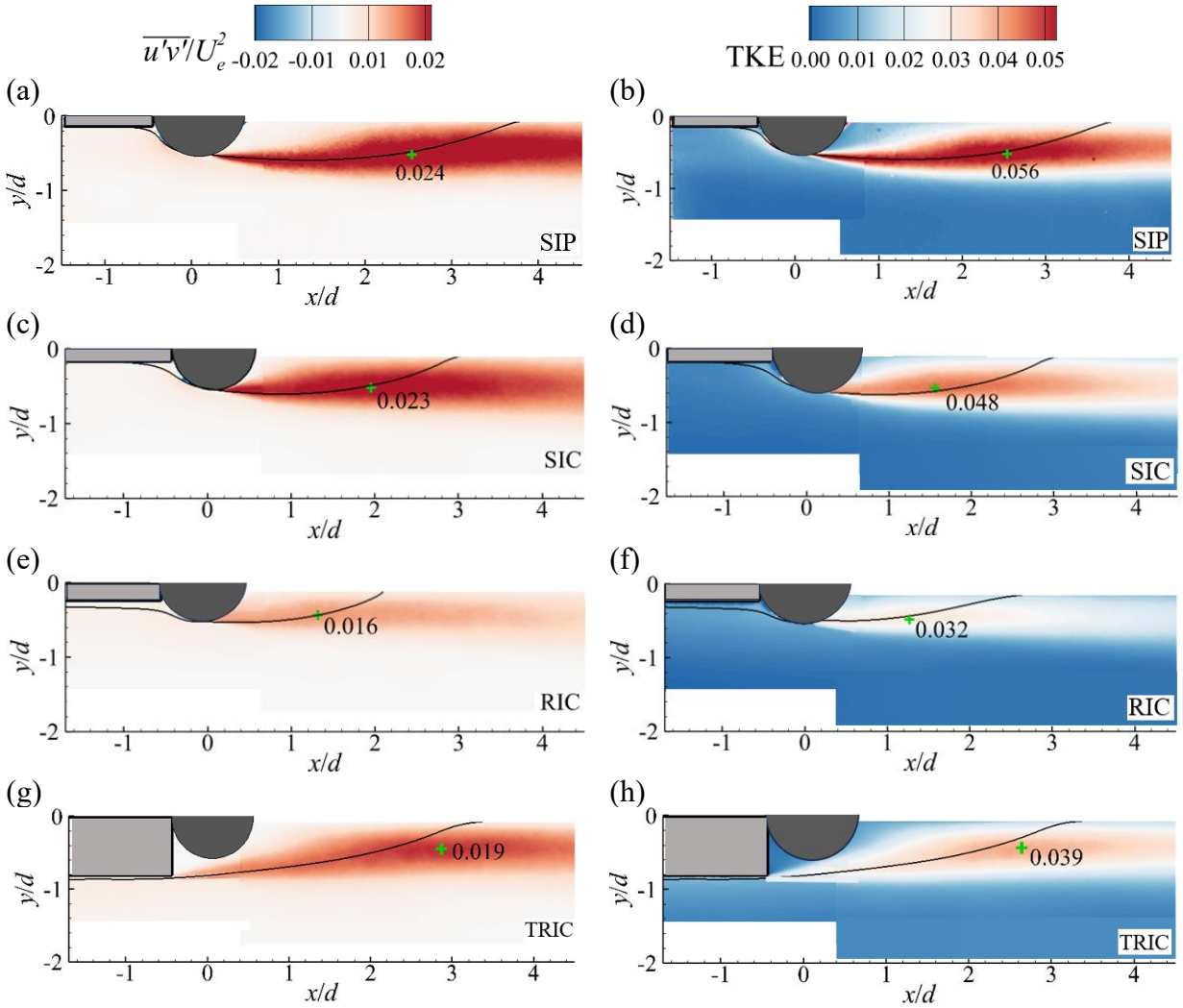

Figure 4.2.6. Contour plots of Reynolds shear stress (left) and turbulence kinetic energy (right). The solid black line is the mean separating streamline. The locations (green '+' symbol) and magnitudes of peak values are also indicated. A white rectangle is used to mask spurious data at the air-water interface.

occurring in the vicinity of the Reynolds normal stresses whiles the locations of the peaks of TKE coincide with those of the streamwise Reynolds normal stress which is the dominant contributor to TKE.

Vertical profiles of the dimensionless Reynolds stresses at five streamwise locations: x/d = 0.0, 1.0, 2.0, 3.0 and 4.0 are shown in Figure 4.2.7. Data from Addai et al. (2024) for partially submerged circular cylinders with no upstream ice block is included for comparison. For SIP, SIC

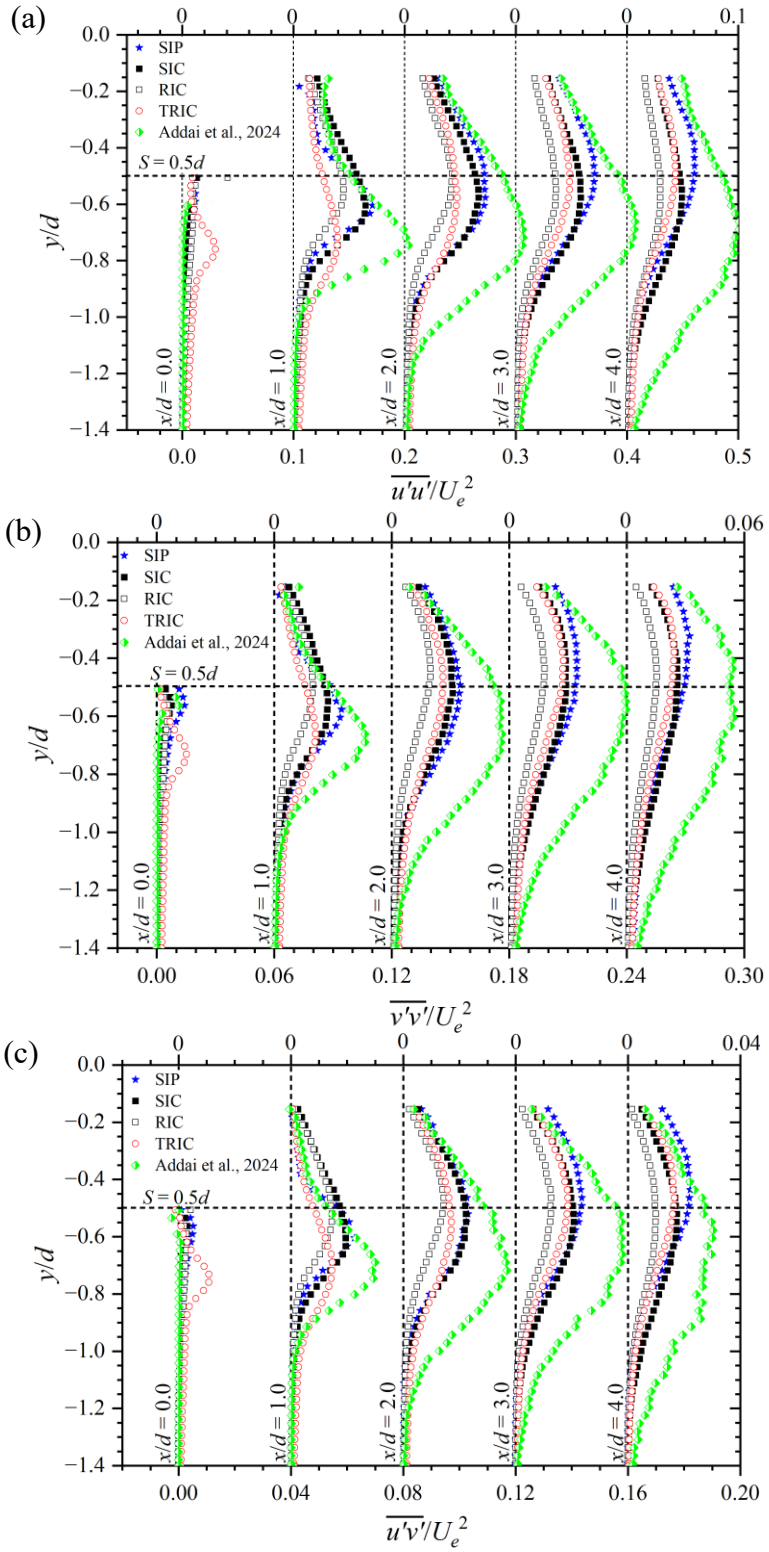

Figure 4.2.7. Vertical profiles of dimensionless streamwise Reynolds normal stress (a), vertical Reynolds normal stress (b) and Reynolds shear stress (c). The profiles at consecutive locations are shifted to the right of the preceding location for clarity. Data from Addai et al. (2024) for a partially submerged circular cylinder with no upstream ice block is included for comparison.

and RIC, the peaks in the profiles at locations near the cylinder ($x/d < 2.0$) are larger compared to those further downstream of the cylinder due to the breakdown of large-scale structures generated at separation. Similar results were reported in previous studies on wall-mounted and partially buried bluff bodies (Akoz 2012; Essel et al. 2015; Tang et al. 2018). On the other hand, the peaks in the profiles of the Reynolds stresses in TRIC increase gradually with streamwise location, and eventually, these profiles collapse and evolve in a manner like those of the other test cases. The magnitudes of the Reynolds stresses in Addai et al. (2024) are significantly higher than those of the present test cases due to the open water condition upstream of the cylinder in the former case. The peaks in Addai et al. (2024) are also located further below the free surface. This observation demonstrates that the separated shear layer, in the case of the cylinder in open water condition, descends farther into the freestream flow compared to when the cylinder is placed downstream of an ice block. As the length of the smooth undersurface ice block increases in the upstream direction (SIC), the levels of Reynolds stresses reduce compared to the case of the shorter ice block (SIP), particularly at streamwise locations beyond $x/d = 2$. This diminishing effect on the levels of Reynolds stresses in the shear layer becomes more pronounce when the undersurface of the ice block becomes rough (RIC). With the thickening of the rough ice block (TRIC), the levels of the Reynolds stresses increase compared to the case of RIC and eventually, at streamwise locations farther downstream of the cylinder, the levels of the Reynolds stresses in TRIC become comparable to the case of SIC.

4.2.4 Budget of turbulence kinetic energy and turbulence transport

The effects of the different upstream ice block conditions on the budget terms of turbulence kinetic energy around the partially submerged cylinder are examined in this section. The vertical profiles

of the individual production terms and the total production at the location of maximum turbulence kinetic energy are shown in Figure 4.2.8(a, c, e, g) to quantitatively assess their relative contributions to the total TKE production. The sign of $-\overline{u'u'}\frac{\partial U}{\partial x}$ changes from negative (i.e., energy sink) in the region adjacent to the free surface but acts as an energy source (i.e., positive) as the freestream is approached. The vertical location at which the change in sign of $-\overline{u'u'}\frac{\partial U}{\partial x}$ occurs coincides with the location of the mean separating streamline. It is noted that the sign change of $-\overline{u'u'}\frac{\partial U}{\partial x}$ is less prominent in TRIC compared to the other cases which may be a due to the different characteristic of the shear layer that initiates from the trailing edge of the ice block in TRIC. The continuity equation applied to the present incompressible flow simplifies to $\frac{\partial U}{\partial x} = -\frac{\partial V}{\partial y}$; thus, the sign and contribution from the vertical fluctuating velocities ($-\overline{v'v'}\frac{\partial V}{\partial y}$) are opposite to $-\overline{u'u'}\frac{\partial U}{\partial x}$. As such, the Reynolds normal stress terms in the production equation can be combined as $(\overline{v'v'} - \overline{u'u'})\frac{\partial U}{\partial x}$ and this acts as either an energy source or sink depending on the relative magnitudes of $\overline{u'u'}$ and $\overline{v'v'}$ and the sign of $\frac{\partial U}{\partial x}$. Since $\overline{u'u'} > \overline{v'v'}$ in all the test cases, the magnitude of $-\overline{u'u'}\frac{\partial U}{\partial x}$ is larger than that of $\overline{v'v'}\frac{\partial U}{\partial x}$, and the net contribution from the Reynolds normal stresses changes from negative to positive across the shear layers. For the shear stress terms, the contribution from $-\overline{u'v'}\frac{\partial V}{\partial x}$ is negligible whiles the contribution from $-\overline{u'v'}\frac{\partial U}{\partial y}$ is positive due to the occurrence of positive $\overline{u'v'}$ and negative $\frac{\partial U}{\partial y}$. Since the magnitude of positive $-\overline{u'v'}\frac{\partial U}{\partial y}$ is significantly higher than the contribution from $(\overline{v'v'} - \overline{u'u'})\frac{\partial U}{\partial x}$, the net TKE production is positive, and $-\overline{u'v'}\frac{\partial U}{\partial y}$ serves as the primary energy source. The peak of the total TKE production is 18%, 42% and 38% lower in SIC, RIC, and TRIC, respectively, compared to

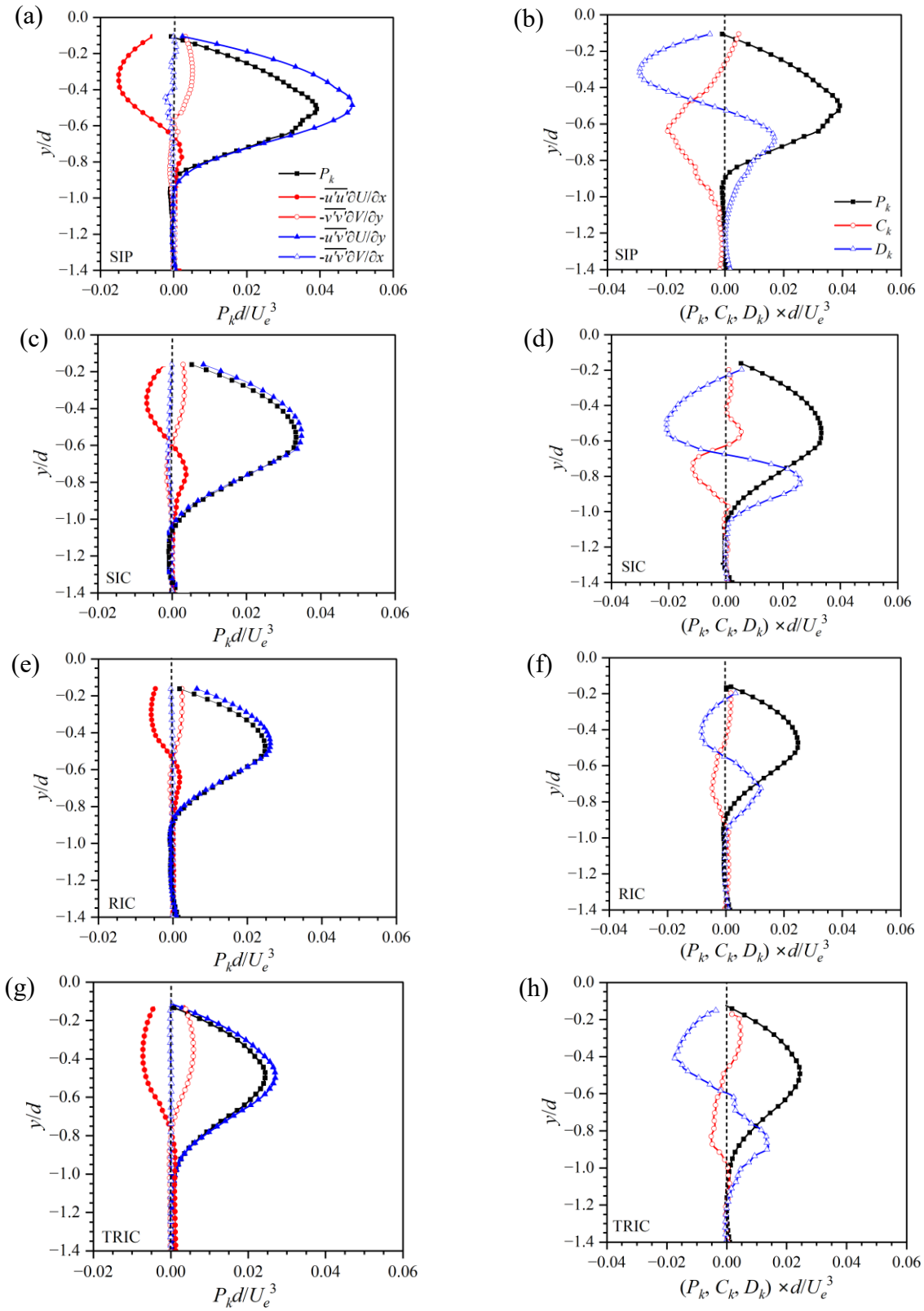

Figure 4.2.8. Vertical profiles of the individual production terms (left) and budget terms (right) of turbulence kinetic energy extracted through the location of maximum turbulence kinetic energy.

the case of SIP.

Figure 4.2.8(b, d, f, h) present vertical profiles of the production, convection and diffusion terms at the location of maximum turbulence kinetic energy. Regardless of the upstream ice block condition, the convection and diffusion terms switch signs so as to balance each other across the separated shear layer. From the free surface to the vertical location where this change in sign occurs, the diffusion term predominantly acts as an energy sink whiles the convection term acts as an energy source. Except for SIP, the vertical location where the convection and diffusion terms change signs nearly coincide with each other. However, in all cases, the diffusion term is more dominant compared to the convection term, underscoring the stronger turbulent fluxes across the separated shear layers. Similar to the turbulence production, the convection and diffusion of turbulence around the cylinder gradually become less pronounced with the upstream progression of the ice pan (SIP) to form a stable ice cover (SIC) and with the roughening of the undersurface of the ice cover (RIC). Nonetheless, the thickening of the rough ice cover (TRIC) enhances convection and diffusion of the turbulence produced around the cylinder compared to the thinner, rough undersurface case (RIC).

The third order moments of velocity fluctuations are used to examine the effects of different ice block conditions on the transport of turbulence around the cylinder. Here, the transport of turbulence kinetic energy by streamwise and vertical fluctuating velocities are represented by $(\overline{u'u'u' + v'v'u'})$ and $(\overline{u'u'v' + v'v'v'})$, respectively (Essel and Tachie 2015; Addai et al. 2024). Contour plots of $(\overline{u'u'u' + v'v'u'})$ and $(\overline{u'u'v' + v'v'v'})$ are shown in Figure 4.2.9. Regardless of the test case, the distributions of $(\overline{u'u'u' + v'v'u'})$ and $(\overline{u'u'v' + v'v'v'})$ are qualitatively similar in that they are both concentrated along the separated shear layers, and have positive and negative regions demarcated by the mean separating streamline. Since $u'u'$ and $v'v'$ are positive, the signs

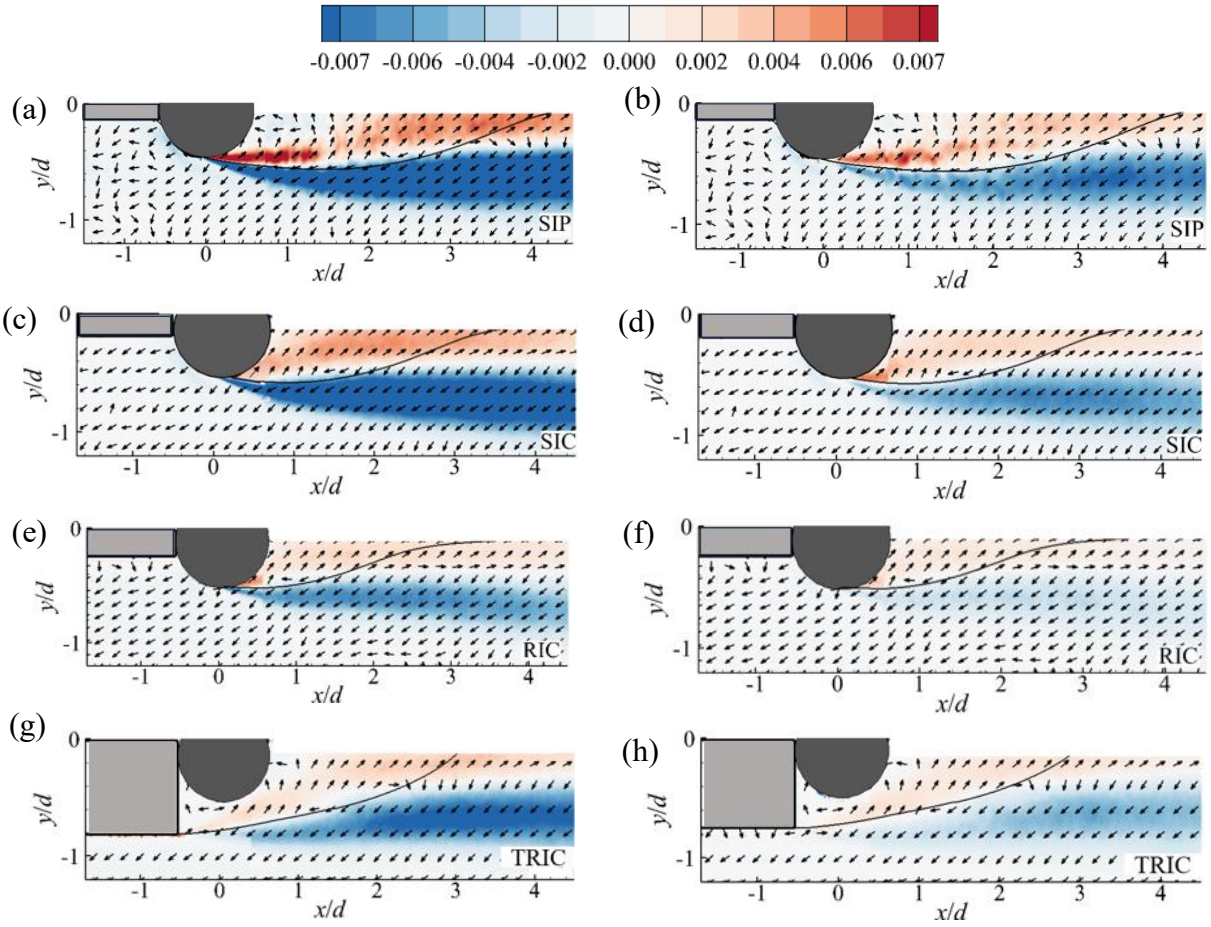

Figure 4.2.9. Contour plots and vectors of the third order moments $(\overline{u'u'u' + v'v'u'})/{U_e}^3$ (left) and $(\overline{u'u'v' + v'v'v'})/{U_e}^3$ (right). The black solid line is the mean separating streamline. The same contour levels are used for both velocity correlations to facilitate comparisons. A white rectangle is used to mask spurious data at the air-water interface.

of $(\overline{u'u'u' + v'v'u'})$ and $(\overline{u'u'v' + v'v'v'})$ originate from the velocity fluctuations. Therefore, by simultaneously analyzing the topologies of both $(\overline{u'u'u' + v'v'u'})$ and $(\overline{u'u'v' + v'v'v'})$, the dominant fluid transport events occurring along the separated shear layer can be deduced. Above the mean separating streamline, both $(\overline{u'u'u' + v'v'u'})$ and $(\overline{u'u'v' + v'v'v'})$ are positive indicating that fast entrainment events $(+u', +v')$ are prevalent in this region. However, below the mean separating streamline, $(\overline{u'u'u' + v'v'u'})$ and $(\overline{u'u'v' + v'v'v'})$ are negative and this highlights the dominance of slow ejection events $(-u', -v')$ in this region. The transport of

turbulence from the shear layer, where it is produced, into the freestream flow through slow ejection events exceeds the transport of turbulence towards the free surface by fast entrainment events as evidenced by the higher intensity of the negative regions of ($\overline{u'u'u' + v'v'u'}$) and ($\overline{u'u'v' + v'v'v'}$) compared to the positive regions. Nonetheless, turbulence transport by streamwise fluctuating velocities exceeds that by vertical fluctuating velocities as evidenced by the intense distributions of ($\overline{u'u'u' + v'v'u'}$) compared to ($\overline{u'u'v' + v'v'v'}$), and the intensity of the transport events around the cylinder varies among the test cases depending on their respective turbulence levels.

4.2.5 Two-point spatial autocorrelation

In this section, two-point spatial autocorrelations of the velocity fluctuations are used to examine the effects of upstream ice block conditions on the spatial dynamics of the coherent vortical structures. The two-point spatial autocorrelation coefficient of the velocity fluctuation u_i' is defined as follows:

$$R_{u_i u_i} = \frac{\overline{u_i'(\boldsymbol{X}_{ref}) u_i'(\boldsymbol{X}_{ref} + \Delta \boldsymbol{X})}}{{u_i'}_{rms}(\boldsymbol{X}_{ref}) {u_i'}_{rms}(\boldsymbol{X}_{ref} + \Delta \boldsymbol{X})} \tag{4.15}$$

where $\boldsymbol{X}_{ref}$ and $\Delta \boldsymbol{X}$ represent the reference position and relative displacement, respectively. Figure 4.2.10(a, c, e, g) present contours of the autocorrelation coefficients of u' (R_{uu}) at five arbitrary points along the mean separating streamline, and Figure 4.2.10(b, d, f, h) show contours of the autocorrelation coefficients of v' (R_{vv}) juxtaposed with the vector field (R_{vu}, R_{vv}) at the midpoint of the mean separating streamline. The vector field (R_{vu}, R_{vv}) has previously been interpreted as the stochastic estimation of spanwise vortical structures based on v' at a given reference point (Kevin, Monty and Hutchins 2019; Fang and Tachie 2019b).

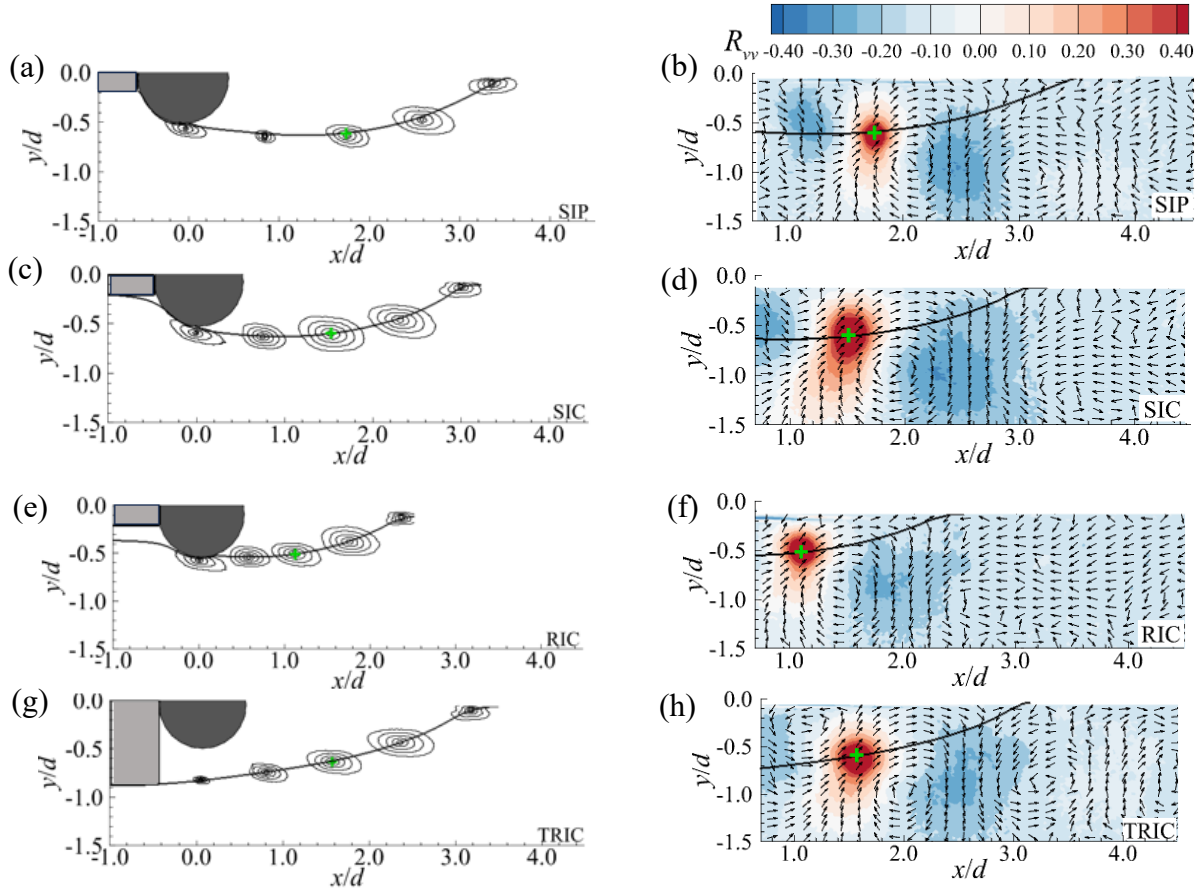

Figure 4.2.10. Contour plots of the autocorrelation coefficients of u' (R_{uu}) at five arbitrary points along the mean separating streamline (left), and v' (R_{vv}) overlaid with the vector field (R_{vu}, R_{vv}) at the midpoint of the mean separating streamline (right). The highest and lowest levels of the contour plots of R_{uu} are 0.9 and 0.5, respectively, and the contour levels are at intervals of 0.1.

The contours of R_{uu} for SIP, SIC and RIC at $x/d = 0$ and near the vertical location of mean flow separation from the cylinder surface are stretched and inclined at an angle of about -18° to the cylinder surface, as a result of the deflection of the approach flow. At each reference point, the R_{uu} contours are elliptical and stretched in the streamwise direction signifying that the vortical structures embodied in R_{uu} have higher spatial coherence in the streamwise direction than in the vertical direction. The spatial extents of the R_{uu} contours gradually increase as the shear layers evolve downstream away from the cylinder due to the pairing up of relatively smaller vortical structures to form larger structures in the shear layer. When the separated shear layer impinges on

the free surface, the large-scale coherent structures are broken down resulting in the substantial reduction in the size of R_{uu} contours at the impingement point on the free surface. The R_{vv} contours reveal alternating patterns of positive and negative values around the cylinder, regardless of the upstream ice block condition. Similar results were reported in the separated shear layers of partially submerged cylinders (Addai et al. 2024), and along the wake centerline of cylinders fully immersed in uniform flow (Le et al. 1997; Perret 2009; Tang et al. 2015). Le et al. (1997) and Tang et al. (2015) interpreted the alternating patterns of R_{vv} along the wake centerline of cylinders fully immersed in uniform flow as imprints of the alternate VK vortex shedding phenomenon. In the vicinity of the reference point of the R_{vv} contours, counterclockwise and clockwise vortical structures, respectively, form above and below the mean separating streamline. This phenomenon indicates that the coherent structures in the separated shear layers induce the fast entrainment and slow ejection events which, respectively, transport the turbulence produced in the separated shear layers towards the free surface and into the freestream flow as observed in Figure 4.2.9.

Figure 4.2.11 presents profiles of R_{uu} in the streamwise direction and R_{vv} in the vertical direction extracted through the midpoint of the mean separating streamline to assess the effects of upstream ice block conditions on the spatial extents of the coherent structures embodied in R_{uu} and R_{vv}. The profiles of both R_{uu} and R_{vv} show qualitative similarities wherein their values are unity at the reference point (i.e., the self-correlation point) and decrease towards zero with increasing distance away from the reference point. The profiles are also distinctly asymmetric about the self correlation point which is similar to the results of previous studies on partially submerged cylinders and wall-mounted bluff bodies (Essel and Tachie 2017; Addai et al. 2024). The integral length scale, determined by integrating R_{uu} and R_{vv} from the self-correlation point to the point where the values of R_{uu} and R_{vv} are zero, is often used to quantify the physical size of the structures in R_{uu} and R_{vv}

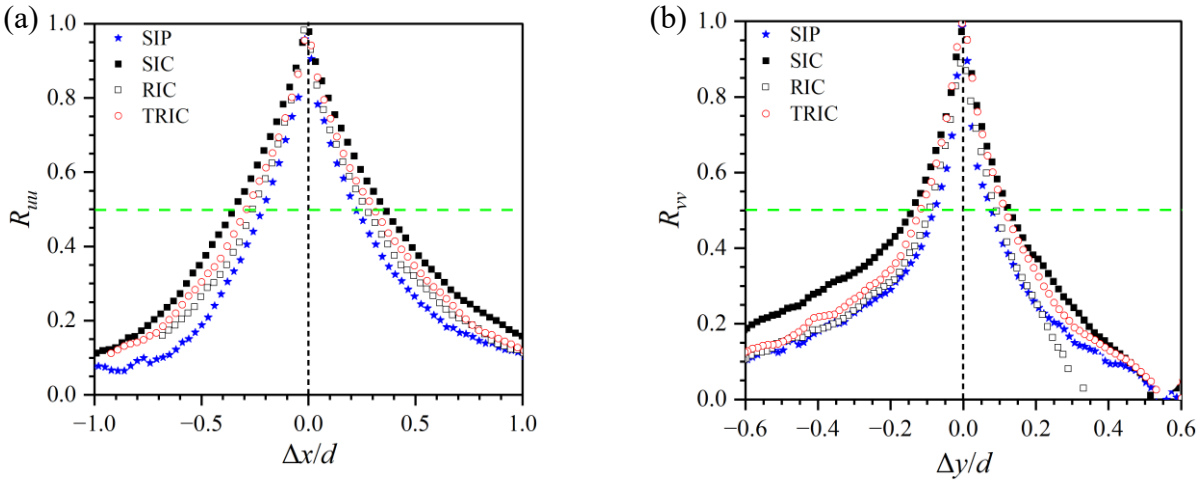

Figure 4.2.11. Profiles of (a) streamwise (R_{uu}) and (b) vertical (R_{vv}) two-point autocorrelation coefficients extracted through the midpoint of the mean separating streamline.

(Ruderich and Fernholz 1986; O'Neill et al. 2004). Since most of the profiles did not decay to zero, the streamwise length scales of the structures in R_{uu} (Lx_{uu}) and the vertical length scales of the structures in R_{vv} (Ly_{vv}) are estimated by measuring the horizontal distance between the points at either side of the self-correlation point where the values of the respective correlation coefficients are 0.5 (Volino et al. 2009). Using this method, the streamwise length scales are evaluated to be Lx_{uu} = 0.46d, 0.72d, 0.52d and 0.58d for SIP, SIC, RIC and TRIC, respectively, and the corresponding vertical length scales are Ly_{vv} = 0.16d, 0.28d, 0.18d and 0.22d. The larger length scales of SIC compared to SIP suggests that the structural integrity of coherent structures in the separated shear layer decreases with increasing upstream ice block length. The higher values of Lx_{uu} compared to Ly_{vv} also indicate that the streamwise velocity fluctuations are associated with the relatively larger scales of turbulence motions around the cylinder.

5 CONCLUSION AND RECOMMENDATION

In this chapter, summary and conclusions of this present study are provided and recommendations for future research work are made based on the findings.

5.1 Effects of Blockage Ratio, Submergence Level and Upstream Ice Cover

Time-resolved PIV was used to examine the spatial and temporal dynamics of the wake of a single, stationary partially submerged horizontal circular cylinder. The effects of blockage ratio (BR = 5% and 9%), submergence level (S/d = 0.50 and 0.75), and a simulated upstream ice cover were investigated. A reference experiment was performed on a circular cylinder fully immersed in the uniform flow for comparison. The Reynolds number, based on freestream velocity and the cylinder diameter, was maintained at 10 000. The results were analyzed using the instantaneous and mean flow, shear layer growth, Reynolds stresses and turbulence kinetic energy, energy budget, frequency spectra, proper orthogonal decomposition (POD), and reverse flow area.

Instantaneous flow analyses revealed that the wake of a partially submerged circular cylinder is exemplified by erratic pairing up and breaking down of small-scale retrograde and prograde vortical structures. Distinct recirculation bubbles form in the wake. Due to the absence of an upper separated shear layer, the mean recirculation length of a partially submerged cylinder is longer, but the turbulence levels and energy budget terms are lower compared to the case of the cylinder fully immersed in uniform flow. It was observed that an increase in blockage ratio of the partially submerged cylinder has negligible effect on the mean recirculation length but substantially increases the turbulence levels and energy budget terms. On the effects of submergence level, it was found that the mean recirculation length reduces with decreasing submergence level because of the closer proximity of the shear layer to the free surface at lower submergence levels but the

submergence level of the cylinder had negligible impact on the turbulence levels and energy budget terms. The presence of a simulated upstream ice cover shortens the mean recirculation length and decreases the turbulence levels and energy budget terms around the partially submerged cylinder due to the boundary layer which forms underneath the ice cover. However, the separated shear layer, in all cases, is demarcated by two distinct regions of linear growth: the first region encompasses the first half of the mean recirculation bubble and shows a lower growth rate compared to the second region which bounds the second half of the mean recirculation bubble. The wake flow of the cylinders is also highly anisotropic, regardless of boundary condition, with vertical fluctuating velocities being dominant over streamwise fluctuating velocities in the uniform flow case and vice versa in the partially submerged cases. In the uniform flow case, the maximum turbulence production occurs along the wake centerline with $-\overline{v'v'}\frac{\partial V}{\partial y}$ as the primary energy source, however, for the partially submerged cases, the maximum production occurs within the shear layer with $-\overline{u'v'}\frac{\partial U}{\partial y}$ as the primary energy source.

The frequency spectra of fluctuating velocities showed that, unlike the uniform flow case, the wake of a partially submerged cylinder is characterized by irregular patterns of fluctuating velocities, and multiple low frequencies, indicating the presence of a wide range of large-scale vortical structures in the wake flow. These large-scale vortical structures in the wake of the partially submerged circular cylinder are, however, less energetic compared to those associated with the case of the cylinder fully immersed in the uniform flow. In the uniform flow case, the first two POD modes make similar energy contributions mainly from vertical velocity fluctuations. However, in the cases of the partially submerged cylinders without upstream ice cover, the energy contribution from mode 1 is two to three times as large as that from mode 2. It was found that an increase in blockage ratio increases the energy contents of the largest vortical structures in the

wake flow, but the energy contents are not significantly affected by changes in submergence level. When the partially submerged is placed behind an ice cover, the energy content of the first mode reduces substantially and becomes comparable with that of the second mode. Nonetheless, regardless of the upstream flow condition, the energy contributions by the POD modes of the partially submerged cylinder are primarily from the streamwise velocity fluctuations. Additionally, in all the flow configurations, the coefficients of the first POD modes correlate with the flapping motions of the separated shear layers, but the degree of correlation is significantly higher in the partially submerged cases compared to the uniform flow case. The degree of correlation between the first POD mode and the flapping motions of the shear layer in the partially submerged cases, however, varies depending on submergence level, blockage ratio and upstream flow condition. Nonetheless, the dominant dimensionless flapping frequencies (based on recirculation length) for the fully immersed and partially submerged cylinders are in good agreement with those reported for separated flows induced by a wide range of bluff body geometries and adverse pressure gradient.

5.2 Effects of Different Upstream Ice Block Conditions

These experiments were designed to investigate the effects of the different stages of evolution of upstream ice on the mean flow and turbulence transport phenomena around an ice boom pontoon. The ice boom pontoon was modelled using a partially submerged circular cylinder, and a double-frame PIV technique was used for the velocity measurements. Four conditions of upstream ice were considered: (1) a short ice pan with smooth undersurface, (2) a long ice cover with smooth undersurface, (3) a long ice cover with rough undersurface, and (4) a long, thickened ice cover with rough undersurface, using simulated ice blocks. The cylinder was held stationary at a

submergence level of S/d = 0.50, and the Reynolds number was maintained at 25 500. The results were discussed in terms of the mean velocity and recirculation length, shear layer growth, Reynolds stresses, energy budget of turbulence kinetic energy and turbulence transport. The distinct features and evolution of coherent vortical structures around the cylinder were also examined using the two-point spatial autocorrelation coefficient.

The results show that, the boundary layers underneath the ice covers are more developed than that underneath the ice pan. Thus, an ice boom downstream of an ice cover is subject to an approach flow with lower momentum but higher turbulence intensity than when it initially retains an ice pan. Rough undersurface of the ice cover causes larger momentum deficits and enhances the turbulence level in the boundary layer relative to that of the smooth ice cover. It was observed that the size of the mean recirculation bubble as well as the intensity and persistence of the mean flow deflection, acceleration, and entrainment of external flow into the wake flow behind the cylinder reduces as the ice pan elongates to form an ice cover and with the subsequent roughening of the ice cover undersurface. However, when the submerged thickness of the rough ice cover becomes larger than the submergence level of the cylinder, a larger recirculation bubble forms from the trailing edge of the ice cover, and the mean flow accelerates rapidly, entraining ambient flow into the wake more aggressively than in the relatively thinner, rough ice cover case.

The higher turbulence intensities in the approach boundary layer underneath the ice covers promotes the growth of the separated shear layers and causes the separated shear layers to transition rapidly from laminar to turbulent compared to the case of the ice pan. Regardless of upstream ice block condition, the streamwise Reynolds normal stresses are dominant compared to the vertical Reynolds normal stresses, but the production and levels of turbulence as well as the convection and diffusion of turbulence around the cylinder decreases as the turbulence intensity in

the approach boundary layer increases. Two-point spatial autocorrelation of velocity fluctuations along the separated shear layer, in all the cases, revealed that the streamwise velocity fluctuations are associated with the relatively larger scales of turbulence motion around the cylinder, and the vortical structures associated with the streamwise fluctuating velocities have higher coherence in the streamwise direction than in the vertical direction. It was also found that the vortical structures in the separated shear layer induce fast entrainment and slow ejection events above and below the mean separating streamline, respectively, through which the turbulence produced in the separated shear is transported towards the free surface and into the freestream. Nonetheless, the structural integrity of the coherent vortical structures in the separated shear layer decreases as the ice pan elongates in the upstream direction to form an ice cover.

5.3 Recommendations for Future Work

The present study has provided qualitative and quantitative insights into various aspects of the turbulent flow dynamics around a single stationary partially submerged circular cylinder. Based on the results from this study, the following recommendations are made for future research.

1. Since a planar PIV technique was used in the present experiments, only two velocity components were available, and the turbulence kinetic energy was estimated based on the two components of velocity fluctuations. In the future, a stereoscopic PIV technique should be employed to obtain all three velocity components for accurate estimation of turbulence kinetic energy.
2. The present experiments were focused on the canonical case of a single, stationary partially submerged circular cylinder. However, in most practical applications, the floating pontoons are usually flexible and free to oscillate at the open water surface. To model these real-life

scenarios, it is recommended that future experimental studies investigate the spatiotemporal characteristics of the wake flow around an oscillating partially submerged circular cylinder. Follow-up studies can then be conducted to examine the effects of different upstream conditions on the separated flow dynamics around the oscillating cylinder.

REFERENCES

Abdelnour, R., Nicholson, C., and Gong, Y. (1999). The design, fabrication and deployment of an ice boom to protect two hydroelectric power plant water intakes from ice blockages during winter. *Ice in Surface Waters*, *2*, 669–677.

Addai, S., Tachie, M.F., Dow, K., Clark, S.P., and Israel, M.K. (2024). Separated flow around half-submerged horizontal circular cylinders at different Reynolds numbers. *Experiment in Fluids*, *65*(1), 10.

Agyei-Agyemang, K.H., Essel, E.E., and Tachie, M.F. (2023). Effects of aspect ratio on flow characteristics on free surface-mounted rectangular cylinders. In *The 10th International Symposium on Turbulence, Heat and Mass Transfer*, Rome, Italy.

Akon, A.F., and Kopp, G.A. (2018). Turbulence structure and similarity in the separated flow above a low building in the atmospheric boundary layer. *Journal of Wind Engineering and Industrial Aerodynamics*, *182*, 87–100.

Akoz, M. (2012). Investigation of vortical flow characteristics around a partially buried circular cylinder. *Ocean Engineering*, *52*, 35–51.

Aleyasin, S.S., Tachie, M.F., and Balachandar, R. (2021). Characteristics of flow past elongated bluff bodies with underbody gaps due to varying inflow turbulence. *Physics of Fluids*, *33*, 125106.

Angrilli, F., Bergamaschi, S., and Cossalter, V. (1982). Investigation of wall induced modifications to vortex shedding from a circular cylinder. *ASME Journal of Fluids Engineering*, 104, 518–522.

Arie, M., Kiya, M., Suzuki, Y., Hagino, M., and Takahashi, K. (1981). Characteristics of circular cylinders in turbulent flows. *Bulletin of JSME*, *24*, 640–647.

Bai, H., and Alam, M.M. (2018). Dependence of square cylinder wake on Reynolds number. *Physics of Fluids*, *30*(1), 015102.

Beltaos, S. (1983). River ice jams: theory, case studies, and applications. *Journal of Hydraulic Engineering*, *109*(10), 1338–1359.

Boucher, E. (2017). River ice and ice jams. *International Encyclopedia of Geography*, John Wiley & Sons, Ltd, 1–8.

Bouscasse, B., Colagrossi, A., Marrone, S., and Souto-Iglesias, A. (2017). SPH modelling of viscous flow past a circular cylinder interacting with a free surface." *Computers and Fluids*, *146*, 190–212.

Brown, G. L., and Roshko, A. (1974). On density effects and large structure in turbulent mixing layers. *Journal of Fluid Mechanics*, *64*(4), 775–816.

Brun, C., Aubrun, S., Goossens, T., and Ravier, Ph. (2008). Coherent structures and their frequency signature in the separated shear layer on the sides of a square cylinder. *Flow, Turbulence and Combustion*, *81*(1-2), 97-114.

Buresti, G., and Lanciotti, A. (1979). Vortex shedding from smooth and roughened cylinders in crossflow near a plane surface. *Aeronautical Quarterly*, *30*, 305–321.

Cantwell, B., and Coles, D. (1983). An experimental study of entrainment and transport in the turbulent near wake of a circular cylinder. *Journal of Fluid Mechanics*, *136*, 321–374.

Capone, A., Klein, C., Di Felice, F., and Miozzi, M. (2016). Phenomenology of a flow around a circular cylinder at sub-critical and critical Reynolds numbers. *Physics of Fluids*, *28*, 074101.

Castro, I.P., and Haque, A. (1987). The structure of a turbulent shear layer bounding a separation region. *Journal of Fluid Mechanics*, *179*, 439–468.

Chalmers, H., Fang, X., and Tachie, M.F. (2023). Gap ratio effects on the coherent structures surrounding a near-wall square cylinder, *International Journal of Heat and Fluid Flow*, *100*, 109114.

Chen, W. L., Li, H., and Hu, H. (2014). An experimental study on the unsteady vortices and turbulent flow structures around twin-box-girder bridge deck models with different gap ratios. *Journal of Wind Engineering and Industrial Aerodynamics*, *132*, 27–36.

Cherry, N.J., Hillier, R., and Latour, M.E. M.P. (1984). Unsteady measurements in a separated and reattaching flow. *Journal of Fluid Mechanics*, *144*, 13–46.

Cimarelli, A., Leonforte, A., De Angelis, E., Crivellini, A., and Angeli, D. (2019). On negative turbulence production phenomena in the shear layer of separating and reattaching flows, *Physics Letters A*., 383, 1019–1026.

Doligalski, T. L., Smith, C.R., and Walker, J.D.A. (1994). Vortex interactions with walls. *Annual Review of Fluid Mechanics*, *26*, 573–616.

Dong, S., Karniadakis, G.E., Ekmekci, A., and Rockwell, D. (2006). A combined direct numerical simulation-particle image velocimetry study of the turbulent near wake. *Journal of Fluid Mechanics*, *569*, 185–207.

Edie, E., Clark, S., and Dow, K. (2021). Hydraulic effects of an ice boom in ice-free conditions. In *CGU HS Committee River Ice Processes Environment*, Saskatoon, Saskatchewan, Canada.

Edie, E.D. (2022). Investigation of the hydraulic effects of ice booms. *M.Sc. Thesis*, University of Manitoba, Canada.

Essel, E.E., Nematollahi, A., and Tachie, M.F. (2015). *Effects of upstream roughness and Reynolds number on separated and reattached turbulent flow*. *Journal of Turbulence*, 16(9), 872–899.

Essel, E.E., and Tachie, M.F. (2017). Upstream roughness and Reynolds number effects on turbulent flow structure over forward-facing step. *International Journal of Heat Fluid Flow*, *66*, 226–242.

Essel, E.E., Tachie, M.F., and Balachandar, R. (2021). Time-resolved wake dynamics of finite wall-mounted circular cylinders submerged in a turbulent boundary layer. *Journal of Fluid Mechanics*, *917*, 1–40.

Fang, X., and Tachie, M.F. (2019a). On the unsteady characteristics of turbulent separations over a forward-backward-facing step. *Journal of Fluid Mechanics*, *863*, 994–1030.

Fang, X., and Tachie, M.F. (2019b). Flow over surface-mounted bluff bodies with different spanwise widths submerged in a deep turbulent boundary layer. *Journal of Fluid Mechanics*, *877*, 717–758.

Fang, X., and Tachie, M.F. (2020). Spatio-temporal dynamics of flow separation induced by a forward-facing step submerged in a thick, turbulent boundary layer. *Journal of Fluid Mechanics*, *892*, A40.

Fang, X., Tachie, M.F., and Dow, K. (2022). Turbulent separations beneath semi-submerged bluff bodies with smooth and rough undersurfaces. *Journal of Fluid Mechanics*, *974*, A19.

Fang, X., Dow, K., Tachie, M.F., Jarrod, M., and Wang, S. (2023). Flow characteristics beneath ice blocks with smooth and rough undersurfaces. *Journal of Hydraulic Engineering*, *149*(4), 04023005.

Foltyn, E.P. and Tuthill, A.M. (1996). Design of ice booms. *USACE CRREL Cold Regions Technical Digest*, *96*.

Gebre, S., Alfredsen, K., Lia, L., Stickler, M., and Tesaker, E. (2013). Review of ice effects on hydropower systems. *Journal of Cold Regions Engineering*, *27*(4), 196–222.

George, W.K. (2013). *Lectures in Turbulence for the 21st Century*. Chalmers University of Technology, Gothenburg, Sweden

Gerrard, J.H. (1967). A disturbance-sensitive Reynolds number range of the flow past a circular cylinder. *Journal of Fluid Mechanics*, *22*, 187–196.

Graziani, A., Kerhervé, F., Martinuzzi, R.J., and Keirsbulck, L. (2018). Dynamics of the recirculating areas of a forward-facing step. *Experiments in Fluids*, *59*, 1–18.

Griffin, O.M. (1995). A note on bluff body vortex formation. *Journal of Fluid Mechanics*, *284*, 217–224.

Hancock, P.E., and Bradshaw, P. (1987). The structure of a turbulent boundary layer beneath a turbulent freestream. *Journal of Fluid Mechanics*, *205*, 45–76.

He, G.-S., Wang, J.-J., Pan, C., Feng, L.-H., Gao, Q., and Rinoshika, A. (2017). Vortex dynamics for flow over a circular cylinder in proximity to a wall. *Journal of Fluid Mechanics*, *812*, 698–720.

Hicks, F. (2009). An overview of river ice problems: CRIPE07 guest editorial. *Cold Regions Science and Technology*, *55*(2), 175–185.

Hopkins, M., and Tuthill, A. (2002). Ice boom simulations and experiments. *Journal of Cold Regions Engineering*, *16*(3), 138–155.

Istvan, M.S., and Yarusevych, S. (2018). Effects of freestream turbulence intensity on transition in laminar separation bubble formed over an airfoil. *Experiments in Fluids*, *59*(3), 1–21.

Kevin, Monty, J., and Hutchins, N. (2019). Turbulent structures in a statistically three-dimensional boundary layer. *Journal of Fluid Mechanics*, *859*, 543–565.

Khabbouchi, I., Guellouz, M. S., and Ben Nasrallah, S. (2013). A study of the effect of the jet-like flow on the near-wake behind a circular cylinder close to a plane wall. *Experimental Thermal Fluid Science*, *44*, 285–300.

Khabbouchi, I., Fellouah, H., Ferchichi, M., and Guellouz, M.S. (2014). Effects of freestream turbulence and Reynolds number on the separated shear layer from a circular cylinder. *Journal of Wind Engineering and Industrial Aerodynamics*, *135*, 46–56.

Kiya, M., Sasaki, K., and Erie, M. (1982). Discrete vortex simulation of a turbulent separation bubble. *Journal of Fluid Mechanics*, *120*, 219–244.

Kiya, M., and Sasaki, K. (1983). Structure of a turbulent separation bubble. *Journal of Fluid Mechanics*, *137*, 83–113.

Kumahor, S., and Tachie, M.F. (2023b). Turbulent flow around a short rectangular cylinder in uniform flow at moderate Reynolds numbers. *Experimental Thermal Fluid Science*, *147*, 110960.

Lander, D.C., Letchford, C. W., Amitay, M., and Kopp, G.A. (2016). Influence of the bluff body shear layers on the wake of a square prism in a turbulent flow. *Physical Review Fluids*, *1*(4), 044406.

Largeau, J.F., and Moriniere, V. (2006). Wall pressure fluctuations and topology in separated flows over a forward-facing step. *Experiment in Fluids*, *42*, 21–40.

Le, H., Moin, P., and Kim, J. (1997). Direct numerical simulation of turbulent flow over a backward-facing step. *Journal of Fluid Mechanics*, *330*, 349–374.

Liddiard, A., Abdelnour, R., Tremblay, R., Quach, T., and Morse, B. (2002). Design and monitoring of a prototype ice boom for use in an area of high current velocity. In *Proceedings of the 16th International Association for Hydro-Environment Engineering and Research International Symposium on Ice*, Dunedin, New Zealand.

Lin, C., and Hsieh, S.-C. (2003). Convection velocity of vortex structures in the near wake of a circular cylinder." *Journal of Engineering Mechanics*, *129*, 1108–1118.

Løset, S. (1994b). Discrete element modelling of a broken ice field - Part II: Simulation of ice loads on a boom. *Cold Regions Science and Technology*, *22*(4), 349–360.

Lui, M., Kumahor, S., and Tachie, M.F. (2024). Reynolds number effects on turbulent wakes generated by rectangular cylinders with streamwise aspect ratios between 1 and 4. *Journal of Fluids Engineering*, *146*, 1–21.

Lyn, D.A., and Rodi, W. (1994). The flapping shear layer formed by flow separation from the forward corner of a square cylinder. *Journal of Fluid Mechanics*, *267*, 353–376.

Mohammed-Taifour, A., and Weiss, J. (2016). Unsteadiness in a large turbulent separation bubble. *Journal of Fluid Mechanics*, *799*, 383–412.

Moore, D.M., Letchford, C.W, and Amitay, M. (2019). Energetic scales in a bluff body shear layer. *Journal of Fluid Mechanics*, *875*, 543–575.

Morse, B., Francoeur, J., Delcourt, H., and Leclerc, M. (2006). Ice control structures using piers, booms and nets. *Cold Regions Science and Technology*, *45*(2), 59–75.

Nematollahi, A., and Tachie, M.F. (2018). Time-resolved PIV measurement of influence of upstream roughness on separated and reattached turbulent flows over a forward-facing step. *AIP Advances*, *8*(10), 105110-105110–36.

Nguyen, Q.D., and Lei, C. (2023). A PIV study of blockage ratio effects on flow over a confined circular cylinder at low Reynolds numbers. *Experiments in Fluids*, *64*, 1–17.

Nishino, T. (2007). Dynamics and stability of flow past a circular cylinder in ground effect. *Ph.D. Thesis*, University of Southampton, United Kingdom.

Nishino, T., and Roberts, G.T. (2008). Absolute and convective instabilities of two-dimensional bluff body wakes in ground effect. *European Journal of Mechanics B/Fluids*, *27*, 539–551.

Norberg, C., and Sunden, B. (1987). Turbulence and Reynolds number effects on the flow and fluid forces on a single cylinder in cross flow. *Journal of Fluids and Structures*, *1*, pp. 337–357.

Nyantekyi-Kwakye, B., Essel, E.E., Dow, K., Clark, S.P., and Tachie, M.F. (2019). Hydraulic and turbulent flow characteristics beneath a simulated partial ice-cover. *Journal of Hydraulic Research*, *59*(3), 392–403.

Ozdil, N.F.T., and Akilli, N. (2015). Investigation of flow structure around a horizontal cylinder at different elevations in shallow water. *Ocean Engineering*, *96*, 56–67.

O'Neill, P. L., Nicolaides, D., Honnery, D., and Soria, J. (2004). Autocorrelation functions and the determination of integral length with reference to experimental and numerical data. In *15th Australasian Fluid Mechanics Conference*, Sydney, Australia.

Pariset, E., and Hauser, R. (1961). Formation and evolution of ice covers on rivers. *Transactions*, *Engineering Institute of Canada*, *5*.

Pearson, D.S., Goulart, P.J., and Ganapathisubramani, B. (2013). Turbulent separation upstream of a forward-facing step. *Journal of Fluid Mechanics*, *724*, 284–304.

Perret, L. (2009). PIV investigation of the shear layer vortices in the near wake of a circular cylinder. *Experiment in Fluids*, *47*(4-5), 789–800.

Perrin, R., Braza, M., Cid, E., Cazin, S., Barthet, A., Sevrain, A., Mockett, C., and Thiele, F. (2007). Obtaining phase averaged turbulence properties in the near wake of a circular cylinder at high Reynolds number using POD. *Experiments in Fluids*, *43*, 341–355.

Poole, D.C. (1994). Investigation of floating boom structures. *M.Sc. Thesis*, University of Manitoba, Canada.

Price, S.J., Sumner, D., Smith, J.G.B., Leong, K.F., and Païdoussis, M.P. (2002). Flow visualization around a circular cylinder near to a plane wall. *Journal of fluids and Structures, 16*, 175–191.

Rahman, M.S., and Tachie, M.F. (2019). Reynolds number effect on flow characteristics of surface single and twin jets. *Journal of Hydraulic Research*, *57*(6), 808–821.

Rajagopalan, S., and Antonia, R.A. (2005). Flow around a circular cylinder-structure of the near wake shear layer. *Experiments in Fluids*, *38*, 393–402.

Riches, G., Martinuzzi, R., and Morton, C. (2018). Proper orthogonal decomposition analysis of a circular cylinder undergoing vortex-induced vibrations. *Physics of Fluids*, *30*, 105103.

Ruderich, R., and Fernholz, H. H., (1986). An experimental investigation of a turbulent shear flow with separation, reverse flow and reattachment. Journal of Fluid Mechanics, 163, 283–322.

Samimy, M., and Lele, S.K. (1991). Motion of particles with inertia in a compressible free shear layer. *Physics of Fluids*, *3*(8), 1915–1923.

Sciacchitano, A., and Wieneke, B. (2016). PIV uncertainty propagation. *Measurements in Science and Technology*, *27*(8), 84006.

Senarathbandara, R., Clark, S.P., and Dow, K. (2023). Experimental analysis on hanging dam formation and evolution. *Water* (*Basel*), *15*(24), 4242.

Shabaka, I., Mehta, R., and Bradshaw, P. (1985). Longitudinal vortices imbedded in turbulent boundary layers. Part 1. Single vortex. *Journal of Fluid Mechanics*, *155*, 37–57.

Sirovich, L. (1987). Turbulence and the dynamics of coherent structures. iii. dynamics and scaling. *Quarterly Applied Mathematics*, *45*, 583–590.

Tang, S.L., Djenidi, L., Antonia, R.A., and Zhou, Y. (2015). Comparison between velocity-and vorticity-based POD methods in a turbulent wake. *Experiment in Fluids*, *56*(8).

Thacker, A., Aubrun, S., Leroy, A., and Devinant, P. (2013). Experimental characterization of flow unsteadiness in the centerline plane of an Ahmed body rear slant. *Experiments in Fluids*, *54*, 1479.

Timco, G., and Cornett, A. (1996). Laboratory tests of ice interaction with steel booms. *Canadian Journal of Civil Engineering*, *23*(2), 560–566.

Triantafyllou, G., and Dimas, A.A. (1989). Interaction of two-dimensional separated flows with a free surface at low Froude numbers. *Physics of Fluids*, *1*, 1813–1821.

Uruba, V., and Procházka, P. (2020). POD spectrum of the wake behind a circular cylinder. *MATEC Web Conferences*, *328*, 5006.

Volino, R.J., Schultz, M.P., and Flack, K.A. (2009). Turbulence structure in a boundary layer with two-dimensional roughness. *Journal of Fluid Mechanics*, *635*, 75–101.

Wang, X.K., and Tan, S.K. (2008). Near wake flow characteristics of a circular cylinder close to a wall. Journal of Fluids and Structures, *24*(5), 605–627.

Wang, Q., Gan, L., Xu, S., and Zhou, Y. (2020). Vortex evolution in the near wake behind polygonal cylinders. *Experimental Thermal Fluid Science*, *110*, 109940.

Wu, Y., and Christensen, K.T. (2006). Population trends of spanwise vortices in wall turbulence. *Journal of Fluid Mechanics*, *568*, 55–76.

Yagmur, S., Dogan, S., Aksoy, M.H., Canli, E., and Ozgoren, M. (2015). Experimental and numerical investigation of flow structures around cylindrical bluff bodies. *EFM14 - Experimental Fluid Mechanics 2014*, *92*, 02113.

Zhou, J., Adrian, R.J., Balachandar, S., and Kendall, T.M. (1999). Mechanisms for generating coherent packets of hairpin vortices in channel flow. *Journal of Fluid Mechanics*, *387*, 353–396.

APPENDIX

A.1 Convergence Analysis of TR-PIV Measurements

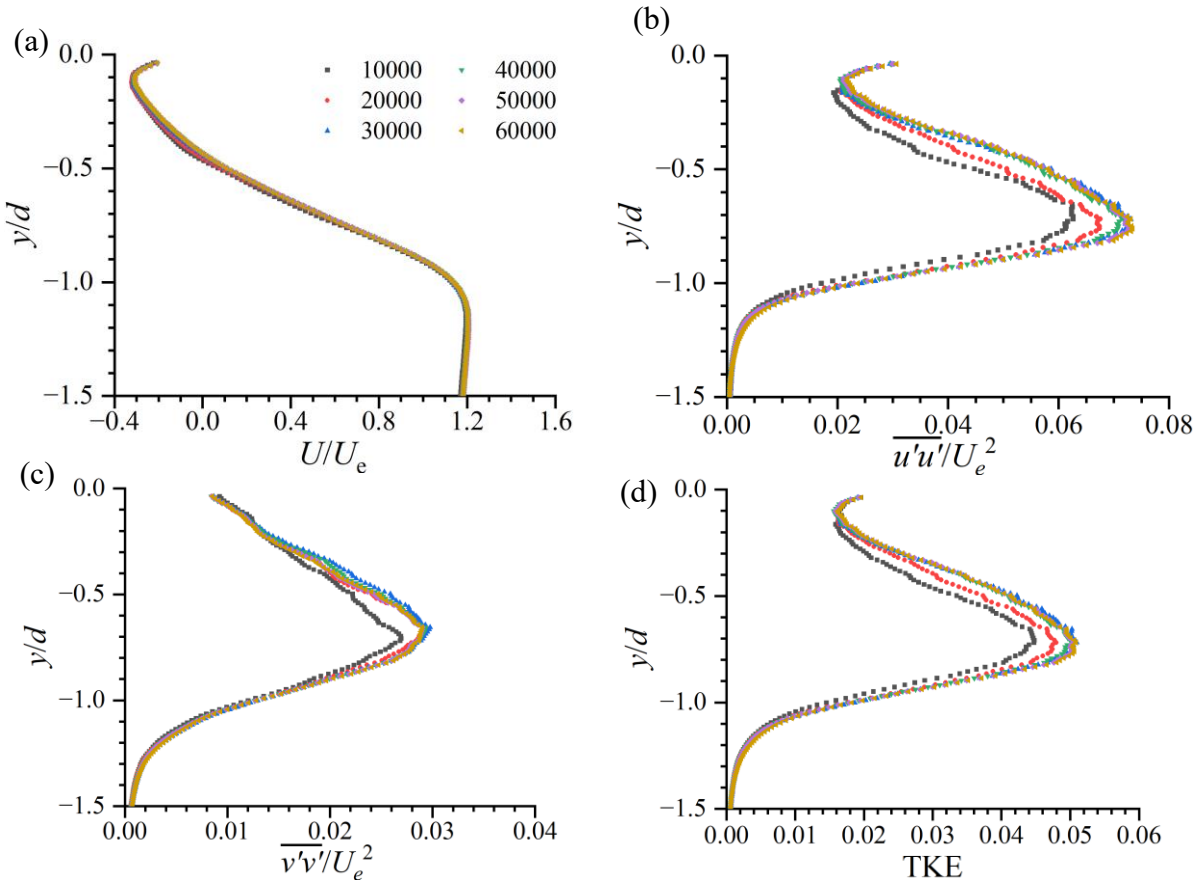

Figure A1. Vertical profiles of streamwise mean velocity (a), streamwise Reynolds normal stress (b), vertical Reynolds normal stress (c) and turbulence kinetic energy (d) extracted through the midpoint of the recirculation bubble for SC_{75} using different sample sizes.

Table A1. Mean and root-mean-square values of fluctuating reverse flow area for SC_{75} using different sample sizes.

Sample size	$\bar{A}/d^2$	A_{rms}/d^2
10 000	2.98	3.12
20 000	2.89	3.05
30 000	2.84	2.97
40 000	2.78	2.92
50 000	2.78	2.92
60 000	2.77	2.91

A.2 Copyright Details

This is a License Agreement between Mark Kofi Israel ("User") and Copyright Clearance Center, Inc. ("CCC") on behalf of the Rightsholder identified in the order details below. The license consists of the order details, the Marketplace Permissions General Terms and Conditions below, and any Rightsholder Terms and Conditions which are included below.

All payments must be made in full to CCC in accordance with the Marketplace Permissions General Terms and Conditions below.

Order Date	01-Aug-2024	Type of Use	Republish in a thesis/dissertation
Order License ID	1511716-1		
ISSN	0142-727X	Publisher	ELSEVIER INC.
		Portion	Chapter/article

LICENSED CONTENT

Publication Title	The International journal of heat and fluid flow	Country	United States of America
		Rightsholder	Elsevier Science & Technology Journals
Article Title	Experimental investigation of the turbulent wake of partially submerged horizontal circular cylinders	Publication Type	Journal
		Start Page	109509
		Volume	109
Author / Editor	INSTITUTION OF MECHANICAL ENGINEERS (GREAT BRITAIN		
Date	01/01/1979		
Language	English		

REQUEST DETAILS

Portion Type	Chapter/article	Rights Requested	Main product
Page Range(s)	1-17	Distribution	Worldwide
Total Number of Pages	17	Translation	Original language of publication
Format (select all that apply)	Print, Electronic	Copies for the Disabled?	No
Who Will Republish the Content?	Academic institution	Minor Editing Privileges?	Yes
		Incidental Promotional Use?	No
Duration of Use	Life of current edition		
Lifetime Unit Quantity	Up to 499	Currency	CAD

NEW WORK DETAILS

Title	Experimental investigation of the turbulent wake of partially submerged horizontal circular cylinders	Institution Name	University of Manitoba
		Expected Presentation Date	2024-08-09
Instructor Name	Mark Kofi Israel		

ADDITIONAL DETAILS

Order Reference Number	N/A	**The Requesting Person / Organization to Appear on the License**	Mark Kofi Israel

REQUESTED CONTENT DETAILS

Title, Description or Numeric Reference of the Portion(s)	10.1016	**Title of the Article / Chapter the Portion Is From**	Experimental investigation of the turbulent wake of partially submerged horizontal circular cylinders
Editor of Portion(s)	Israel, Mark K.; Dow, Karen; Clark, Shawn P.; Tachie, Mark F.	**Author of Portion(s)**	Israel, Mark K.; Dow, Karen; Clark, Shawn P.; Tachie, Mark F.
Volume / Edition	109		
Page or Page Range of Portion	109509	**Issue, if Republishing an Article From a Serial**	N/A
		Publication Date of Portion	2024-09-30

RIGHTSHOLDER TERMS AND CONDITIONS

Elsevier publishes Open Access articles in both its Open Access journals and via its Open Access articles option in subscription journals, for which an author selects a user license permitting certain types of reuse without permission. Before proceeding please check if the article is Open Access on http://www.sciencedirect.com and refer to the user license for the individual article. Any reuse not included in the user license terms will require permission. You must always fully and appropriately credit the author and source. If any part of the material to be used (for example, figures) has appeared in the Elsevier publication for which you are seeking permission, with credit or acknowledgement to another source it is the responsibility of the user to ensure their reuse complies with the terms and conditions determined by the rights holder. Please contact permissions@elsevier.com with any queries.

Marketplace Permissions General Terms and Conditions

The following terms and conditions ("General Terms"), together with any applicable Publisher Terms and Conditions, govern User's use of Works pursuant to the Licenses granted by Copyright Clearance Center, Inc. ("CCC") on behalf of the applicable Rightsholders of such Works through CCC's applicable Marketplace transactional licensing services (each, a "Service").

1) **Definitions.** For purposes of these General Terms, the following definitions apply:

"License" is the licensed use the User obtains via the Marketplace platform in a particular licensing transaction, as set forth in the Order Confirmation.

"Order Confirmation" is the confirmation CCC provides to the User at the conclusion of each Marketplace transaction. "Order Confirmation Terms" are additional terms set forth on specific Order Confirmations not set forth in the General Terms that can include terms applicable to a particular CCC transactional licensing service and/or any Rightsholder-specific terms.

"Rightsholder(s)" are the holders of copyright rights in the Works for which a User obtains licenses via the Marketplace platform, which are displayed on specific Order Confirmations.

"Terms" means the terms and conditions set forth in these General Terms and any additional Order Confirmation Terms collectively.

"User" or "you" is the person or entity making the use granted under the relevant License. Where the person accepting the Terms on behalf of a User is a freelancer or other third party who the User authorized to accept the General Terms on the User's behalf, such person shall be deemed jointly a User for purposes of such Terms.